



universität
wien

DISSERTATION

Titel der Dissertation

Production and detection of neutral molecular beams:
From single amino acids to biomolecular complexes

angestrebter akademischer Grad

Doktor der Naturwissenschaften (Dr. rer.nat.)

Verfasser:	Mag. Markus Marksteiner
Matrikel-Nummer:	0002118
Dissertationsgebiet (lt. Studienblatt):	Physik
Betreuer:	Univ.-Prof. Dr. Markus Arndt

Wien, am 28. Juni 2010

Contents

Abstract	6
Zusammenfassung	8
I Introduction	10
Matter waves	12
Matter wave interference	13
A new source for biomolecules	16
A new detector for molecules	17
II Laser desorption and post-ionization of molecules	20
1 Introduction to laser desorption and post-ionization	22
1.1 Supersonic gas jets	22
1.2 Laser desorption of molecules	28
1.3 Photo-ionization of molecules	30
1.3.1 Single-photon ionization	32
1.3.2 Multi-photon ionization	32
1.3.3 Mass limit for post-ionization of organic molecules	33
2 Experimental realization of the desorption and post-ionization setup	36
2.1 Setup	36
2.1.1 Detection of the molecules	36
2.1.2 Source	39
2.1.3 Sample molecules	40
2.1.4 Free desorption versus mixing channel	42

2.1.5	Control and alignment of the setup	46
2.2	Results of the laser desorption source	49
2.2.1	Free desorption	49
2.2.2	Straight mixing channel	50
2.2.3	Closed mixing channel	54
2.3	Further improvements of the laser desorption source	56
2.3.1	Velocity measurements	57
2.3.2	Signal stabilization	59
2.4	Comparison of 157 nm versus 266 nm ionization	61
III	Applications of the laser desorption source	66
3	Towards biomolecule interferometry	68
3.1	Laser desorption as a source for biomolecule interference . . .	68
3.1.1	Outlook and application for interferometry	74
4	Gas-phase formation of large organic clusters and organo-metallic complexes	76
4.1	Formation of amino acid clusters	78
4.1.1	Alkaline earth metal inclusion into tryptophan clusters	78
4.1.2	Formation of sodium and copper tryptophan clusters .	84
4.1.3	Formation of phenylalanine calcium clusters	85
4.2	Pure clusters of biomolecules	86
5	A superconducting detector for neutral molecules	92
5.1	Introduction to superconducting detectors	92
5.2	Experimental setup	93
5.3	First detection of neutral biomolecules with a superconducting single photon detector	97
5.4	Outlook and future SSPD experiments	102
6	Summary	104
	Appendix	108
A)	TOF settings	108
B)	Valve Characterization	108
C)	Signal stabilization	109

List of publications	112
Bibliography	113
Acknowledgments	127
Curriculum vitae	129

Abstract

This thesis presents a laser desorption source for neutral organic molecules and clusters as well as the first exploration of a superconducting single photon detector for the detection of massive neutral particles. Whereas the source can produce beams of biomolecules for various gas-phase applications, the detector can be used to overcome the current post-ionization detection mass limit of neutral molecules. The aim of our work is to produce and detect neutral molecular gas-phase beams, ranging from small amino acids over large polypeptides to massive complexes. The purpose of creating these beams is to use them for quantum optics experiments, like near field matter wave interference and its applications in metrology.

Standard effusive sources usually lack the ability to cool the evaporated organic molecules fast enough to prevent fragmentation. In contrast to that, the presented laser desorption source cools the initially evaporated molecules by embedding them into a supersonic seed gas beam. The mixing of the seed gas and the desorbed molecules is implemented both in free expansion as well as inside a closed mixing channel.

The desorbed neutral molecules are detected by photo-ionization using UV (266 nm) and VUV (157 nm) light followed by time-of-flight mass spectrometry. For the amino acid tryptophan (204 amu) and for the antibiotic polypeptide gramicidin (1884 amu) the ion yields for both photo-ionization wavelengths are examined and the ionization cross sections for the UV wavelength are measured. In case of tryptophan the ionization yield is comparable for both wavelengths, whereas gramicidin is detected fifteen times more efficiently under VUV ionization than for UV ionization at equal intensity. Desorption of heavier molecules than gramicidin never resulted in a detectable ion yield, which confirms the known inefficiency for the post-ionization of isolated large organic molecules [1–3].

The desorption source is also used for the formation of large neutral bio-

molecular complexes. The largest observed complex is a gramicidin tetramer with a mass of 7,536 amu. Furthermore, desorption of tryptophan together with alkaline earth salts, such as calcium-carbonate results in the formation of two different kinds of massive tryptophan clusters: Tryptophan clusters containing a single calcium atom with a mass of up to 6,800 amu and also pure clusters with a mass of up to 7,100 amu are observed. The inclusion of a metal atom into tryptophan clusters is observed also for strontium, barium, sodium and copper. The cluster formation is studied additionally for other amino acids such as phenylalanine, the tripeptide tyrosine-tryptophan-glycine and the nucleotide guanine. The cluster formation between two different molecular species was observed after the simultaneous desorption of gramicidin and tryptophan and resulted in the attachment of tryptophan molecules to a single gramicidin.

An alternative detection method to photo-ionization is examined by testing a *superconducting single photon detector* (SSPD) for its ability to detect individual neutral molecules. The sensitivity of the nanostructured SSPD seems not to be limited to small molecules. The superconducting detector is able to record velocity distributions of neutral insulin ($\approx 5,700$ amu), myoglobin (≈ 17 kDa) and hemoglobin (≈ 66 kDa) beams. A check if the intact molecules leave the source is missing due to the lack of alternative detection methods for these molecules. The working principle of the SSPD relies on the fact, that an impinging particle leads to a breakdown of superconductivity. Further developments of the SSPD appear possible and promising in order to increase the mass range of detected neutral organic molecules, which cannot be detected in photo-ionization.

The source is developed in order to fulfill the criteria needed for a combination with a Talbot-Lau interferometer. Interference of biomolecules is, beside the prove of the wave-particle duality, interesting for the examination of their properties like polarizabilities, dipole moments or absorption and collisional cross sections. This work describes the resources for that goal by providing a source for biomolecular beams ready for near future interference experiments and a novel detection method. The source and detector are therefore expected to become important corner stones for future quantum optics experiments.

Zusammenfassung

Die vorliegende Arbeit beschreibt eine Laserdesorptionsquelle für organische Moleküle und Cluster, sowie einen supraleitenden Detektor, der erstmals zur Detektion von neutralen Teilchen eingesetzt wurde. Während die Quelle Strahlen von Biomolekülen für Anwendungen in der Gasphase erzeugt, kann der Detektor das Massenlimit für die Nachionisation von neutralen Biomolekülen signifikant erweitern. Die Motivation für diese Arbeit war die Erzeugung und Detektion von neutralen Strahlen im Massenbereich von kleinen Aminosäuren über Polypeptiden zu großen organischen Komplexen für die zukünftige Verwendung in quantenoptischen Experimenten, wie beispielsweise einem Nahfeld Materiewelleninterferometer und die interferometrische Molekülmetrologie.

Thermische Quellen führen oft für große organische Verbindungen zur Fragmentation der verdampften Moleküle. Dies wird im Falle der Laserdesorptionsquelle durch die Einlagerung der Moleküle in einen überschallgeköhlten Gasstrahl verhindert. Die Implantation der laserverdampften Moleküle in den Gasstrahl wurde im freien Flug, sowie in einem geschlossenem Mischvolumen getestet.

Die Detektion der desorbierten Teilchen wurde mittels UV (266 nm) und VUV (157 nm) Photoionisation und anschließender Flugzeit-Massenspektroskopie durchgeführt. Die Ionisationsraten beider Wellenlängen wurden für die beiden Moleküle Tryptophan und Gramicidin verglichen und die Ionisationswirkungsquerschnitte im UV bestimmt. Während Tryptophan keinen signifikanten Unterschied zeigt, ist im Falle von Gramicidin die Ein-Photonen-Ionisation mit VUV Licht fünfzehn mal effizienter als die Zwei-Photonen-Ionisation im UV bei gleicher Laserintensität. Die Desorption von größeren Molekülen als Gramicidin führte zu keinem nachweislichen Ionisationssignal und bestätigte damit die in der Literatur bekannte ineffiziente Nachionisation von großen organischen Teilchen [1–3].

Die vorgestellte Desorptionsquelle erlaubte auch die Erzeugung von großen Biomolekül-Komplexen. Der massivste nachgewiesene neutrale Komplex war ein Gramicidin-Tetramer mit einer Masse von 7,536 amu. Die gleichzeitige Desorption von Tryptophan und Kalzium-Carbonat führte zur Bildung von zwei unterschiedlichen Arten von Tryptophan-Clustern. Eine Sorte hatten jeweils ein einzelnes Kalzium Atom eingelagert und erreichte eine Masse von 6,800 amu, während auch reine Tryptophancluster mit einer maximalen Masse von 7,100 amu gebildet wurden. Die Einlagerung eines Metalatoms in den Tryptophancluster konnte auch für die Metalle Strontium, Barium, Natrium und Kupfer demonstriert werden. Neben Tryptophan wurden auch noch andere Moleküle wie etwa Phenylalanin, das Tripeptid Tyr-Trp-Gly und das Nukleotid Guanin auf ihre Clusterverhalten untersucht. Im Falle von Gramicidin und Tryptophan konnte auch die Clusterbildung zwischen zwei verschiedenen Molekülen gezeigt werden, wobei sich mehrere Tryptophan Moleküle an ein einzelnes Gramicidin anlagerten.

Neben der Photoionisation wurde mit einem supraleitenden Einzelphotonen Detektor (SSPD) eine andere alternative Detektionsmöglichkeit für neutrale isolierte Moleküle getestet. Der Detektionsnachweis des SSPD scheint nicht nur auf kleine Moleküle beschränkt zu sein. Der supraleitende Detektor konnte für die neutralen Moleküle Insulin ($\approx 5,700$ amu), Myoglobin (≈ 17 kDa) und Hämoglobin (≈ 66 kDa) Geschwindigkeitsverteilungen aufnehmen. Ob diese Moleküle die Laserdesorptionsquelle völlig intakt verlassen, kann allerdings auf Grund fehlender alternativer Detektionsmöglichkeiten nicht überprüft werden. Das Funktionsprinzip des SSPD beruht auf der Zerstörung der Supraleitung in einem Nanodraht durch ein auftreffendes Teilchen. Die Weiterentwicklung des SSPD ist möglicherweise ein wichtiger Schlüssel für die Detektion von schweren neutralen Molekülen.

Die Desorptionsquelle wurde optimiert um eine Kombination mit der Talbot-Lau Interferometrie zu ermöglichen. Interferenz von Biomolekülen eröffnet neben der Überprüfung des Welle-Teilchen Dualismus auch eine interessante Methode um molekulare Eigenschaften wie Polarisierbarkeiten, Dipolmomente oder Absorptions- und Stoßquerschnitte zu messen. Sowohl die Quelle als auch der Detektor sind somit wichtige Bausteine für zukünftige Experimente im Bereich der molekularen Quantenoptik.

Part I

Introduction

Matter waves

In *classical* physics matter is described as consisting of particles, whereas electromagnetic radiation is identified as waves. The revision of this view came with the birth of quantum physics, where the separated treatment of waves and particles is no longer valid. At the turn of the 19th century Max Planck succeeded in explaining the spectral distribution of the black body radiation based on the assumption of particle-like behavior [4]. Planck assumed that the energy E for a certain frequency ω is only given in *quantized* amounts:

$$E = \hbar\omega \tag{1}$$

with the reduced Planck constant¹ $\hbar = 1.055^{-34}$ Js.

In 1905 Albert Einstein described the photoelectric effect [5], which was experimentally examined by Heinrich Hertz, Wilhem Hallwachs and Philipp Lenard, by introducing photons as particles of the electromagnetic radiation. This discovery led to what has become known as the term *particle-wave duality* and was also extended to matter. In 1923 Louis de Broglie proposed that also matter should exhibit wave-like properties [6]. This could immediately explain the electron orbits in the atomic model as proposed by Bohr. De Broglie's waves were experimentally proven in 1927 by Davisson and Germer [7] and independently by Thomson [8] for electrons. Three years later the same phenomenon was demonstrated for H_2 and He [9] and in the mid 30s also for neutrons [10]. For his analysis de Broglie used only Planck's discovery (eq. 1) as well as $E = mc^2$ and the Lorentz transformation from Einstein's theory of special relativity. A particle with the mass m and velocity v has according to de Broglie a wavelength λ of:

$$\lambda = \frac{h}{mv} = \frac{h}{p} \tag{2}$$

With the development of nuclear reactors, intense beams of neutrons could be produced, leading to many neutron interference experiments both in the field of the foundations of quantum physics [11] and as to routine applications in condensed matter physics [12]. After the first atom diffraction experiments in the 1930s it took until the 1980s, before new nanotechnologies and the implementation of the laser provided new experimental techniques. This led to the interference of sodium at standing light waves [13, 14], as

¹The Planck constant h has the value $h = 6.625^{-34}$ Js and \hbar is defined as: $\hbar = \frac{h}{2\pi}$

well as at material gratings [15, 16]. In the 1990s matter wave interference was further extended to diatomic molecules and led to diffraction of I_2 [17], Na_2 [18] and K_2 [19]. Also the discovery of the helium dimer succeeded via diffraction at nanofabricated gratings [20] and was later extended to $^4He_{44}$ clusters [21]. For the molecule D_2 the quantum behavior has also recently been proved by detecting the Poisson spot in the geometrical shadow of an obstacle [22].

Matter wave interference of molecules

By the end of the last century de Broglie's hypothesis had already been tested for electrons, neutrons, atoms and small molecules, leaving no doubt about the existence of the particle-wave duality. From a standard quantum mechanical point of view the duality should not only apply to the smallest building blocks of our universe, but to every object in nature. No principle mass limit exists and every massive object can be assigned a wavelength corresponding to eq. 2. The wavelength gets smaller with increasing mass, such that for example a person with a mass of 75 kg and a speed of 1 m/s has a wavelength of $\lambda \approx 10^{-35}$ m, which is impossible to resolve with current technology. Anyhow, it is a matter of fact, that everyday objects usually do not show any hint of a 'quantum' behavior - an observation, which raises the question why this is the case. The agreement of our every-day macroscopic world with classical physics has led to theoretical proposals, where the combination of quantum physics with the properties of space time results in a spontaneous reduction/collapse of the wave function beyond a certain delocalization time and above a certain mass of the quantum object [23–26]. Such theories may be tested in future interference experiments, if the complexity or mass of the interfering objects reaches the various proposed limits. Although quantum physics is the most exact theory ever invented by mankind, interference of complex particles is therefore expected to be able to contribute new insights into the foundations of physics.

In the late 1990s matter wave interference was started at the University of Vienna with the goal of showing the wave nature of complex molecules. In 1999 the fullerene C_{60} (720 amu) was diffracted at a 100 nm nanofabricated grating [27]. The far-field diffraction at a material grating was extended to the heavier C_{70} (840 amu) [28], before diffraction at a standing light wave was also demonstrated [28, 29]. Exploiting Talbot-Lau effect led to the inter-

ference of fullerenes [30] and perfluorinated fullerenes $C_{60}F_{48}$ (1632 amu) [31] at material gratings as well as to diffraction at a standing light wave for functionalized azobenzenes (1030 amu) [32], to name a few successfully interfered molecules. Talbot-Lau interferometry was also used for lithography by the deposition of the nanostructured periodic interference pattern of C_{60} on a Si surface in ultra-high vacuum [33].

It is still interesting to extend quantum experiments and in particular matter wave interference to more and more complex objects, as it allows, for example, the study of decoherence effects due to the coupling to external degrees of freedoms. But also the reverse is true: Not only can complex particles be used to proof fundamental physics, but the ‘quantum’ effects can also be exploited in combination with metrology to study various properties of the interfering objects. Interference experiments were used to measure atomic polarizabilities [34, 35], the recoil during absorption of even a single photon [36] and the index of refraction for atoms passing through a gas [37]. Also, the molecule interference experiments performed in Vienna have already been used for metrology, i.e. to measure for example the polarizabilities of molecules as demonstrated for fullerenes [38–40]. Quantum interference was also used to study the fragmentation processes in thermally labile molecules [41], the thermally activated conformational dynamics of perfluoroalkyl-functionalized azobenzenes [42] as well as the identification of two isomers [43]. Also the measurement of the absolute photon absorption cross sections in combination with interferometric methods was proposed [44].

Talbot-Lau interferometry

The Talbot-Lau effect is an optical near field effect, which allows the imaging of a periodic structure without the help of any lenses. The Talbot as well as the Lau effect are not only limited to the use of light [45–47], but could also be applied to matter wave interferometry of electrons [48], atoms [18, 49–52] and large molecules [30, 32].

In the nineteenth century William Henry Fox Talbot discovered the reproduction of a periodic structure after illumination with a plane wave [53]. The revival of a periodic grating with grating constant d , as shown in figure 1a, happens at multiples of the so called *Talbot length* L_T :

$$L_T = \frac{d^2}{\lambda} \quad (3)$$

where λ is the wavelength of the particles. In fact the reproduction of the grating at L_T is shifted by $\lambda/2$ and revivals of the grating also appear at distances $L = \frac{n}{m} \frac{d^2}{\lambda}$ with the natural numbers $m > 0$ and $n \geq 0$. The images observed at $m > 1$ are called fractional Talbot effect, whereas the number n stands for the n -th order Talbot effect.

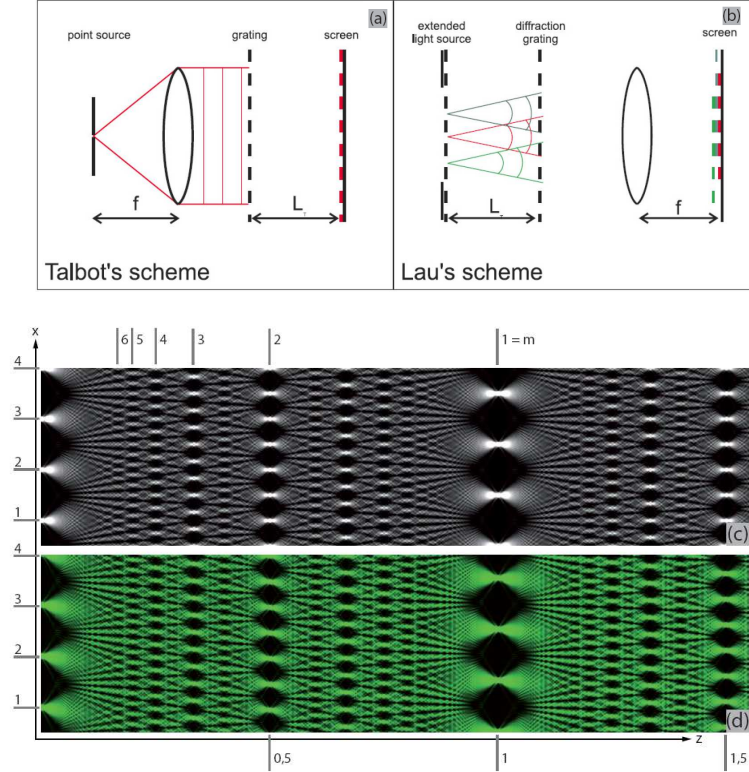


Figure 1: a) Talbot effect: After coherent illumination of a grating it is reproduced in a distance L_T . b) Lau effect: An additional grating at the source allows starting with an incoherent source. Images a) and b) are taken from [54]. c) Theoretical expectation of the Talbot effect. d) Experimental Talbot carpet recorded with light at 532 nm. The z -axis denotes the distance from the grating in multiples of L_T , the x -axis counts the grating periods and m gives the order of the Talbot effect. Pictures c) and d) are taken from [47].

Ernst Lau used the Talbot effect for his studies and observed that using a periodic grating as a source right after a completely incoherent light source resulted again in a reproduction of an illuminated second grating [55]. Lau looked at the image on a screen at infinity in the focal plane of a lens as depicted in figure 1b. Exploiting the Lau effect results in interference even

for an incoherent source. Each slit of the first grating acts as an individual point source, emitting a spherical wave. After the second grating each wave reproduces the grating at L_T due to the Talbot effect. If the two gratings match in periodicity the reproduced image will be the same for all beam paths, so that each path adds to the whole grating image. Therefore the full source aperture can be used without any collimation, which leads to an enormous signal gain for diluted molecular beams.

A theoretical and experimental examination of the Talbot effect with light is shown in figure 1 c and figure 1 d, respectively. In the Talbot length at $m=1$ the first grating is reproduced, but also in front and behind of the Talbot length other orders of the Talbot effect appear. A theoretical description of the Talbot and Lau effect and its combination can be found for example in [56–58].

A new source for biomolecules

The limiting factors in molecular quantum optics are mostly given by the available sources and detectors for neutral large molecules. Although interference of small charged species at high energies could be successfully demonstrated [7, 59, 60], we focus on *neutral* molecules. These have the advantage, that they are less susceptible to decoherence and dephasing effects which would be introduced by stray fields or the interactions of the ions with the gratings.

Our present work was started due to the need for new sources and also new detection methods for matter wave interference. Interesting candidates for future molecular interference applications in metrology are the *biomolecules*. Biomolecules are usually defined as organic molecules, which are found in living organisms. They are available in a mass range starting from small nucleotides and amino acids with less than one hundred atomic mass units² over polypeptides with a few thousand mass units to huge viruses with more than a million mass units. This makes them interesting candidates for a stepwise increase of complexity of interfering particles. Quantum metrology measurements will give insight into their internal structure, which could be used to test state-of-the-art quantum molecular simulations.

²One atomic mass unit (amu) is defined as one twelfth of the mass of a carbon-12 atom. 1 amu = 1.66×10^{-27} kg.

The main requirement for this thesis was to produce an intense beam of neutral complex molecules with moderate fragmentation. In the past an oven heated the molecules until they evaporated. This worked very well for the fullerenes and some organic molecules, like tetraphenylporphyrin (615 amu) or azobenzene (1030 amu). The major limitation of this method is that the more complex molecules tend to fragment at elevated temperatures. For many biomolecules the required evaporation temperature already exceeds the fragmentation energy, leading to the destruction of the molecule during heating.

In this work we consider a new source based on laser desorption followed by supersonic cooling. Laser desorption can bring high mass molecules into the gas-phase and, combined with supersonic cooling, fragmentation can be kept low. It has been demonstrated that molecular temperatures around a few Kelvin can be reached for jet-cooling of laser desorbed molecules [61]. Also the number of possible conformers as well as the vibrational and rotational excitations are reduced in a cold molecular beam, which is favorable for interferometric metrology. The detection of the neutral molecules is performed via single and two-photon ionization with the help of short-pulse lasers.

Chapter 1 gives an overview of supersonic beams, laser desorption and photo-ionization. The design and development of the source is described in chapter 2 and initial tests to combine the source with an interferometer are reported in chapter 3. The production of large neutral organic clusters and complexes with up to 7,000 amu is reported in chapter 4.

A new superconducting detector for molecules

In general the photo-ionization of organic molecules starts to fail above a mass of about 2000 amu [1–3]. This is problematic whenever organic molecules exceeding that mass need to be ionized for further analysis or for detection. In chapter 5 a new type of detector is presented which allows the circumvention of the post-ionization problem. A *superconducting single photon detector* (SSPD), developed for photon detection, was tested in the framework of this thesis for the first time to detect single neutral molecules. The first promising tests with the superconducting detector indicate its sensitivity to neutral single molecules. It was used to record velocity distributions for various neutral molecules. All molecules that could be cross checked by established

detection schemes such as photo-ionization time-of-flight methods, resulted in the same distributions as the ones recorded by the SSPD. The experiments with the SSPD showed a fast time resolution in the order of ten nanoseconds for a single molecule detection event. Where the photo-ionization method fails and others, like fluorescence, are inadequate, the SSPD may become an important method to detect molecules in the range of a few thousand atomic mass units.

Part II

Laser desorption and post-ionization of molecules

Chapter 1

Introduction to laser desorption and post-ionization

1.1 Supersonic gas jets

Supersonic jets are commonly used to produce a low temperature, environment that travels with a certain velocity v . The first pioneering works using supersonic beams were already performed in the 1950s [62, 63] and quickly became standard applications in physic and chemistry. When gas expands from a high pressure reservoir P_0 through a small opening of diameter D into high vacuum with pressure P_b , the gas atoms undergo a large number of collisions during their expansion through the opening. During this expansion the enthalpy of the atoms is converted into kinetic energy, which not only accelerates the atoms but also reduces their temperature. The description of the properties of supersonic beams can be found in more detail in references [64–66].

The name *supersonic* provides already some hint about the velocity class of the beam. It is faster than the speed of sound c , which is the local propagation speed within a gas at temperature T :

$$c = \sqrt{\frac{\gamma R T}{M}} \quad (1.1)$$

where R is the universal gas constant, M the mass of the gas atoms [kg/mol] and $\gamma = c_p/c_v$ the ratio of the heat capacity at constant pressure and constant volume. An important number when discussing supersonic expansion is the

Mach number M_a , which is defined as the ratio of the beam velocity v and the local speed of sound c in that environment.

For simplicity the description of the supersonic expansion is treated for the case of an ideal gas, where friction, heat transfer and external forces are negligible. The gas is first pushed by the pressure difference $P_b - P_0$ towards the orifice of the reservoir, where it expands into vacuum (see figure 1.1). The flow will become supersonic ($M_a=1$), if the pressure ratio P_0/P_b reaches a certain critical value.

Conservation of energy states that the enthalpy³ per unit mass, h_0 , of the gas in the reservoir has to be conserved and can only be split between the increased kinetic energy and the enthalpy h (per unit mass) of the accelerated gas:

$$h_0 = h + \frac{v^2}{2} \quad (1.2)$$

This law can be rewritten in the form

$$\frac{v^2}{2} = h_0 - h = \int_T^{T_0} c_p dT. \quad (1.3)$$

The integration results in

$$\frac{v^2}{2} = c_p(T_0 - T). \quad (1.4)$$

Inserting the specific heat at constant pressure, $c_p = \frac{\gamma}{\gamma-1} \frac{R}{M}$, in eq. (1.4) results in

$$v = \sqrt{2 \frac{\gamma}{\gamma-1} \frac{RT_0}{M} \left(1 - \frac{T}{T_0}\right)}. \quad (1.5)$$

The adiabatic index γ is given by the number of internal degrees of freedom f

$$\gamma = \frac{f+2}{f} \quad (1.6)$$

and amounts to $\gamma=5/3$ for monoatomic gases.

If the gas is cooled during the expansion to $T \ll T_0$ the terminal velocity v_{term} of the gas follows from eq. 1.5:

$$v_{term} = \sqrt{2 \frac{\gamma}{\gamma-1} \frac{RT_0}{M}} = v_{mp} \sqrt{\frac{\gamma}{\gamma-1}}, \quad (1.7)$$

³The enthalpy h is defined as: $h = u + pV$ with u the internal energy, p the pressure and V the volume.

with v_{mp} the most probable speed of an ideal gas at temperature T . Thus the terminal velocity of the expanding gas beam is about 60% faster than the thermal velocity of the gas. Using the definition for the Mach number M_a , eq. (1.1) and eq. (1.5), together with the thermodynamic relation $\frac{P_2}{P_1} = \left(\frac{T_2}{T_1}\right)^{\frac{\gamma}{\gamma-1}}$ gives:

$$M_a = \frac{v}{c} = \sqrt{\frac{2}{\gamma-1} \left(\frac{T_0}{T} - 1\right)} = \sqrt{\frac{2}{\gamma-1} \left[\left(\frac{P_0}{P}\right)^{\frac{\gamma-1}{\gamma}} - 1\right]} \quad (1.8)$$

For $M_a \geq 1$ it follows from eq. (1.8) the relation

$$P_0/P \geq \left(\frac{\gamma+1}{2}\right)^{\gamma/(\gamma-1)}. \quad (1.9)$$

For monoatomic gases with $\gamma=5/3$ this results in the critical value of $\frac{P_0}{P} \geq 2.1$, which has to be reached in order to achieve supersonic velocities.

Given the Mach number M_a all thermodynamic properties of the system can be calculated:

$$\frac{T}{T_0} = \left(1 + \frac{\gamma-1}{2} M_a^2\right)^{-1} \quad (1.10)$$

$$\frac{P}{P_0} = \left(1 + \frac{\gamma-1}{2} M_a^2\right)^{\frac{\gamma}{1-\gamma}} \quad (1.11)$$

$$v = M_a \sqrt{\gamma \frac{RT_0}{M} / \left(1 + \frac{\gamma-1}{2} M_a^2\right)} \quad (1.12)$$

If the propagation of a disturbance is smaller than the speed of sound, $v < c$, the disturbance travels with $v + c$ downstream and with $v - c$ upstream. For $v > c$ no information about obstacles in the beam line can travel upstream, i.e. back towards the nozzle exit. This means that a supersonic beam cannot 'feel' downstream boundary conditions at least within a certain area, which is called the *zone of silence*. Since the beam finally has to adapt to some boundary conditions, such as the walls of the vacuum chamber, the zone of silence is confined by shock waves - areas of high density, velocity, temperature and pressure gradients. The shock wave in front of the source exit is called the *Mach disk*. Figure 1.1 shows a drawing of a supersonic expansion with its different regions. The distance x_M of the Mach disk from the source exit is found experimentally and is given in the literature [64, 65] as multiples of the orifice diameter D :

$$\frac{x_M}{D} \approx 0.67 \left(\frac{P_0}{P_b}\right)^{1/2} \quad (1.13)$$

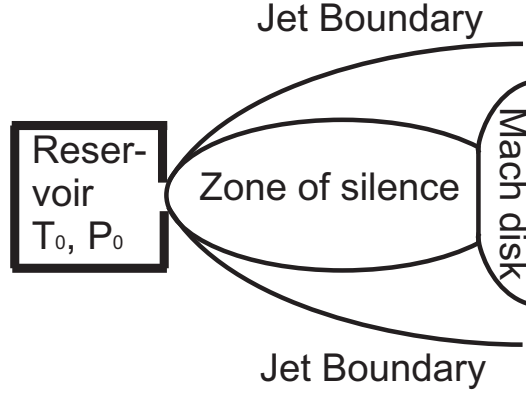


Figure 1.1: Schematic drawing of a supersonic expansion. Depicted are the zone of silence, which is enclosed by the shock waves and the Mach disk perpendicular to the beam direction.

If $M_a \geq 1$ is reached at the source exit and the supersonic beam does not 'feel' any downstream boundary conditions, the velocity of the beam and its Mach number will further increase, whereas the pressure can even reach values below P_b within the zone of silence. The beam is only recompressed by the shock waves, i.e. the barrel shock on the side and the Mach disk in front. Therefore the molecular beam has to be coupled into high vacuum region before it reaches the Mach disk to prevent it from being destroyed by the shock wave. For this reason a skimmer is placed inside the zone of silence to extract the central beam into the subsequent high vacuum region.

As already mentioned, the beam undergoes dramatic changes in density, temperature, pressure, velocity and number of collisions during its expansion. The biggest change of these properties occurs after a distance of a few orifice diameters behind the exit. Due to the high collision frequency a relaxation of internal degrees of freedom also takes place. Further expansion decreases the temperature as well as the collision frequency, leading to slower relaxation processes and in the end to a termination of all collisions. The beam *freezes* out, which means that the mean free path of the molecules gets so large that further collisions can be neglected during the typical time scale of the experiment.

The final velocity distribution of the beam is normally taken as a Maxwell-Boltzmann distribution, which is superimposed on the the mean velocity

v_0 [65]:

$$f(v) \propto \left(\frac{M}{2RT}\right)^{3/2} v^2 \exp\left[-\frac{M}{2RT}(v - v_0)^2\right] \quad (1.14)$$

In order to get a better understanding of the properties of supersonic beams a few quantitative values shall be given in the following. The threshold for the supersonic expansion (eq. (1.9)) was fulfilled easily since the backing pressure in our experiments was typically 2 bar and P_b in the source chamber was below $5 \cdot 10^{-3}$ mbar even with the valve operating at 20 Hz. The distance of the Mach disk can then be calculated using eq. (1.13), which results in $x_M = 134 \cdot D$ or $x_d = 6.7$ cm for a 0.5 mm orifice. To extract the beam within the zone of silence, the skimmer was placed at a distance of about 2 cm behind the source exit. The final velocity of the beam can be calculated using eq. (1.12) if the Mach number is known. In [64] numerical calculations were done, which resulted in two formulas for calculating M_a for an axisymmetric expansion of gases depending on their value of γ . Using the abbreviation $\xi = x_d/D$ the Mach number can be calculated for gases with $\gamma = 5/3$:

$$M_a = \xi^{5/3} [3.232 - 0.7563 \xi^{-1} + 0.3937 \xi^{-2} - 0.0729 \xi^{-3}] \quad \text{for } \xi > 1 \quad (1.15)$$

$$M_a = 1 + 3.337 \xi^2 - 1.541 \xi^3 \quad \text{for } 0 < \xi < 1 \quad (1.16)$$

In figure 1.2 the velocities of helium, argon, krypton and xenon starting at room temperature are plotted using eq. (1.15), eq. (1.16) and eq. (1.12) as a function of multiples of the orifice diameter x_d/D . The terminal velocity v_{term} was calculated with eq. (1.7). Both the Mach number M_a and the velocity increase extremely fast within the first few nozzle diameters and converge slowly towards the terminal velocity of the individual gas. For helium at room temperature the terminal velocity is 1766 m/s, whereas velocities of 558 m/s, 385 m/s and 309 m/s are reached for argon, krypton and xenon, respectively. Starting with a cold gas reduces the velocity of the beam as shown in figure 1.2 for helium and xenon at 100 K.

For monoatomic gases (except for helium) the terminal Mach number M_a^{term} starting from a room temperature reservoir, can be calculated using the formula [67, 68]:

$$M_a^{term} = 133(P_0 D)^{0.4} \quad (1.17)$$

where the nozzle diameter D is given in cm and P_0 in bar. At $P_0 = 2$ bar we find a terminal Mach number of $M_a^{term} = 53$ for a 0.5 mm nozzle. In the case of helium, quantum effects have to be taken into account. This leads to

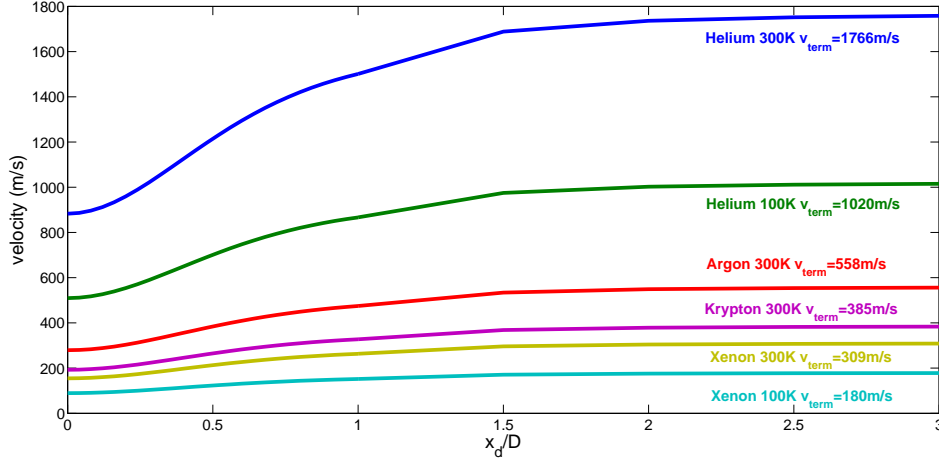


Figure 1.2: Plot of the velocity as a function of x_d/D for helium, argon, krypton and xenon at $T_0=300\text{ K}$ as well as $T_0=100\text{ K}$ for helium and xenon using eq. (1.15), eq. (1.16) and eq. (1.12). The terminal velocity was calculated from eq. (1.7). Already within the first nozzle diameters the final velocity is reached for the various gases.

higher Mach numbers due to increased collisional cross sections and longer interaction times in an expanding helium beam [69].

In our work the supersonic beams are produced with different noble gases ($\gamma=5/3$). The gas jet is used for accelerating and cooling other molecules via collisions. The molecules are embedded into the supersonic gas beam by laser desorption. The carrier gas beam could only be detected by electron impact ionization, but not via photo-ionization, since the ionization energy of the noble gas used cannot be reached by the laser light. This has the advantage that the gas beam does not spoil the molecular mass spectra obtained by photo-ionization.

The supersonic carrier gas does not only accelerate the embedded molecules, but also results in a cooling effect. In principle the cooling of all three degrees of freedom - translational, rotational and vibrational - have to be treated separately. Generally cooling of the rotational degrees of freedom is more effective than the cooling of vibrational modes. This was for example shown for the diatomic iodine I_2 , where the cooling resulted in a rotational temperature, which was fifty times lower than the vibrational temperature [70,71]. The translational temperature was shown to be equal with the rotational temperature. In general lower internal temperatures were achieved by increasing

the mass of the monoatomic seed gas.

Due to the already mentioned quantum effects in helium it is a very special seed gas under certain conditions. Helium can be used with extremely high backing pressure, which results in very low temperatures of the expanding beam. If a high pressure helium reservoir is cooled to about 5 K prior to the expansion, the gas starts to form clusters, helium nanodroplets, which have a temperature as low as 400 mK [72] and can grow to typical cluster sizes of 10^4 – 10^8 helium atoms.

Studies of several nozzle designs are performed in [73], resulting in a translational temperature of 53 mK for a helium beam. The embedment of aniline (93 amu) in a cold helium beam cooled the molecule to a rotational temperature of 400 mK [74], which is comparable to the conditions in a helium nanodroplet. Supersonic helium beams reached a translational temperature of 0.3 mK [75] by using a high backing-pressure and a valve orifice of only 125 μ m. These beams were then later used to proof the existence of the helium dimer [76].

The cooling efficiency is given by the gas properties as well as by other experimental conditions, like for example the nozzle design. Examples for efficient cooling of laser desorbed biomolecules embedded into supersonic beams are given in [61], where rotational temperatures around 5 K for anthracene (178 amu) and vibrational temperatures of about 15 K for diphenylamine (170 amu) are reported for argon as seed gas. But with increasing mass of the embedded molecules the cooling efficiency drops down. Using argon as seed gas the molecule β -carotene (536 amu) was cooled to a translational temperature of 20 K, a rotational temperature of 50–80 K and a vibrational temperature of 100–150 K [77].

1.2 Laser desorption of molecules

The main goal of our source is to produce a beam of neutral gas-phase molecules suitable for future quantum optics experiments. Neutral molecules are favorable, since interferometry with charged particles needs to take into account electromagnetic stray fields in the chamber, ion-grating interactions or ion-ion interactions leading to decoherence and dephasing effects. The description of the laser desorption will therefore be focused on sources which produce neutral molecules. For completeness we add, however, also a short discussion of one of the most widespread laser desorption technique,

which rather produces ions, i.e. Matrix Assisted Laser Desorption Ionization (MALDI) [78–81]. In MALDI analyte molecules are embedded in special matrices, which absorb most of the laser energy. This results in a desorption of the matrix, which is accompanied by an ionization and ejection of the embedded molecules into the gas-phase. For the development of MALDI Koichi Tanaka was awarded with the Nobel Prize in Chemistry in the year 2002 [78] and it soon became a standard tool for the gas-phase studies of large molecules.

The cooling effect of the matrix can, however, be also replaced by any other cold gaseous environment, such as for instance an adiabatically expanding noble gas. The key feature of pulsed laser desorption is that molecules can be softly brought into gas-phase on the nanosecond time scale. This opens the way for experiments with a huge family of thermally labile molecules as for example many biomolecules (for a review see [82]). This is relevant not only in physics and chemistry, but also in medicine and pharmacology. Especially for thermally labile biomolecules, where extended heating leads to fragmentation and denaturation, the fast heating rates of pulsed lasers with up to 10^{13} K/s [82] can be used. The advantage of this fast heating is that the molecules are desorbed, i.e. leave the substrate/sample before they can decompose.

Soon after the invention of the laser, the first laser desorption of salts was shown [83, 84]. The mass of the desorbed species constantly increased and reached the 1,000 amu limit by the end of the 1970’s [85]. In MALDI the ion masses could be constantly increased [78, 80, 81, 86, 87] and reached masses even beyond 5 MDa [88]. But also laser desorption of neutral particles shifted into the focus of research [89–92].

The term laser desorption is not clearly defined. The expressions *laser desorption*, *laser ablation*, *laser ejection* or *laser vaporization* can be found in the literature. Depending on the community, different mechanism refer to the different expressions. Sometimes a distinction is drawn between the term *laser desorption* and the other synonyms by limiting laser desorption to thermal processes where only a few monolayers of material are involved [82]. In this work the term *laser desorption* will be used for the effect of releasing molecules into the gas-phase by heating with a pulsed laser. This will be applied for the desorption of both thin sample surfaces and bulk material.

Some of the first molecule desorption experiments were performed with IR wavelengths. Karas and Hillenkamp [79] showed that a desorption wave-

length in the UV (355 nm and 266 nm) has a strong influence on the ion yield of dipeptides and amino acids. They observed an enhanced total ion yield for desorption wavelengths, which are resonant with the matrix, but where the analyte molecules show no resonance. The dependence of the desorption wavelength for the produced neutral organic molecules was examined for the four wavelengths of a YAG laser (1064 nm, 532 nm, 355 nm and 266 nm) [92]. In the case of the UV wavelengths all tested molecules could be desorbed, whereas for the longer wavelengths only those molecules showed signal, which also show absorption at these wavelengths. The smallest desorption wavelength found in the literature was vacuum ultra-violet at 193 nm [93,94].

Different observations are reported if the desorption pulse width is changed from nanoseconds to pico- or femtoseconds. In [95,96] no relevant change in the mass spectra was observed when the laser shot is reduced to the shorter pulse lengths. Thus it was concluded that the total amount of energy pumped into the sample is the relevant parameter, whereas the time scale has a minor influence [96]. In contrast to that, a lower energy threshold and different mass spectra are reported for 300 fs pulses compared to 15 ns laser pulses [97].

The relevant parameter for a successful desorption is the irradiation threshold. But unfortunately this threshold is not only dependent on the laser wavelength and desorption time. Many other different experimental parameters influence the irradiation threshold like the chemical composition of the sample and the thickness of the sample. And additionally the irradiation threshold also depends on the analyte species. Systematic studies dealing with these parameters are given in [82,98].

1.3 Photo-ionization of molecules

Ionization is not only important for the detection of molecules, but it makes further analysis like mass filter/discrimination very easy. The most prominent ionization mechanisms for molecules in the gas-phase are electron impact ionization (EI) and photo-ionization (PI).

In EI electrons of high kinetic energy, typically between 40 and 70 eV, collide with the molecules. Electron impact ionization has the drawback that fragile molecules tend to fragment instead of emitting an electron and EI has therefore only a limited range of applications for large biomolecules. In contrast to that, photo-ionization may be a soft ionization method for fragile

molecules with only low fragmentation. In PI the ionization energy can be provided by different processes. The most important ones are single-photon ionization, two- or multi-photon ionization, resonant enhanced multi photon ionization and thermionic emission as depicted in figure 1.3. Thermionic

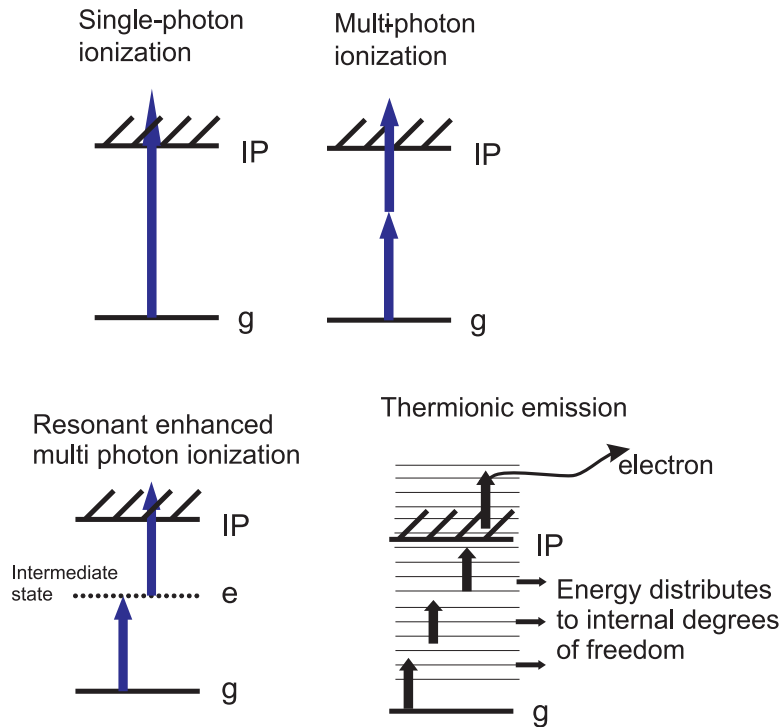


Figure 1.3: Sketch of single photon, multi photon and resonant enhanced multi photon ionization, where photons excite the electronic subsystem until the ionization threshold is reached. In the case of thermionic emission the molecule is excited internally to high vibrational states, which results in the emission of an electron.

ionization was observed for example for fullerenes [99] passing a cw argon laser and used in Vienna as a detection scheme for several interference experiments [27, 30]. The ionization energy of C_{60} is 7.6 eV [100], which would require the absorption of four photons at 532 nm. If the photon density is too low to provide the simultaneous absorption of four photons, the absorbed energy redistributes into internal degrees of freedoms. But if about five to ten times more energy than the ionization potential is pumped into the fullerene it ionizes, since the ionization energy is taken from the stored internal energy [101, 102]. The fullerene survives this enormous heating due to its C-

C bonds, which withstand the high amount of internal energy. Thermionic emission is however not feasible for thermally unstable molecules.

1.3.1 Single-photon ionization

Single-photon ionization (SPI) relies on the fact that the ionization energy has to be provided by a single photon. Since most ionization potentials of biomolecules exceed 7 eV, e. g. tryptophan has 7.3 eV [103], this requires a laser wavelength of less than 177 nm, which is already in the vacuum ultra-violet (VUV) region. Beside VUV lasers at 157 nm as used in our work, VUV light can also be generated at a wavelength of 118 nm (10.5 eV) by sending the third harmonic of a Nd:YAG laser (355 nm) through a gas cell containing a xenon-argon mixture [104–107]. To obtain wavelength tunable VUV light synchrotron radiation has to be used. By varying the photon energy of a synchrotron VUV beam the ionization energies for amino acids and other biomolecules were measured [103, 108].

The ion yield Y in single-photon ionization is given by [109]:

$$Y = \sigma_{pi} \frac{I}{h\nu} \tau N_{Mol} \quad (1.18)$$

where σ_{pi} is the photon-ionization cross section, I the laser intensity, ν the laser frequency, τ the laser duration and N_{Mol} the number of molecules in the laser beam area. A modern review of single-photon ionization can be found in [110].

In our work a F₂ excimer laser with a wavelength of 157 nm resulting in a photon energy of 7.9 eV was used, which allowed single-photon ionization of a variety of molecules. But even for molecules with an ionization energy exceeding 7.9 eV post-ionization with 157 nm light was successfully demonstrated by binding special tags to the molecules and thereby lowering their ionization energy below 7.9 eV [111, 112].

1.3.2 Multi-photon ionization

An alternative to the single-photon ionization is multi-photon ionization (MUPI), where the ionization energy is provided by the absorption of more than one photon. A special case of multi-photon ionization is called *resonance enhanced multi-photon ionization* (REMPI). In the case of REMPI the molecule is first excited to a real internal state, before the next photon

releases the electron into the continuum. Thereby an increased lifetime of an intermediate state increases also the ionization probability.

Neglecting processes like non-radiative decays from intermediate electronic states the ion yield Y for a two-photon process is proportional to the squared laser intensity I^2 [109]:

$$Y = \sigma_1 \sigma_2 \left(\frac{I}{h\nu} \right)^2 \tau^2 N_{Mol} \quad (1.19)$$

where σ_1 and σ_2 are the absorption cross sections for the first and second photon. The first photon excites the molecule into the electronically intermediate state and the second photon transfers the electron into the continuum [113]. If the ionization yield saturates with increasing laser intensity the cross sections σ_1 and σ_2 can be calculated as shown in section 2.4 for tryptophan and gramicidin.

As in the case of the desorption pulses the influence of the laser pulse width was studied also for MUPI [114–119]. Shortening the ionization pulse at a wavelength of 260 nm from 5 ns to 500 fs does not increase the ion yields in the case of benzene and tryptophan [114]. Only for larger biomolecules, as for example β -carotene or gramicidin D, the femtosecond pulse ionizes more efficiently than the nanosecond pulse. This is explained in [114] by assuming that for the larger molecules fast processes in the nanosecond regime at the intermediate state or at the ionization threshold compete with photon excitation or ionization. Therefore the shorter and faster pulse can overcome these relaxation processes. Studies on dipeptides showed, that shortening the pulse width from 5 ns to 250 fs at 266 nm results in reduced fragmentation [119]. For tryptophan reduced fragmentation is reported when using 35 ps instead of 5 ns pulses at 266 nm [116].

From the literature we conclude that SPI is a general ionization method, whereas MUPI may enhance the ion yield and reduce fragmentation, which is the case especially for aromatic amino acids [116]. In our work we explore SPI at 157 nm as well as MUPI at 266 nm for the post-ionization of laser desorbed molecules. A comparison of these two wavelengths for tryptophan and gramicidin is given in section 2.4.

1.3.3 Mass limit for post-ionization of organic molecules

Whereas MALDI has been successfully applied to produce ions of molecules in the MDa regime, the post-ionization of large neutral organic molecules has

not yet advanced into these mass classes. The mass limit for post-ionized molecules seems to be around 2,000 amu [1–3]. Different interpretations have been given to explain the decreasing ion yield with increasing mass. A mechanism was proposed, which is described as *a large molecule acting as its own solvent*, where photo-ionization is described similar to a photo-induced charge separation in solution [1, 2]. The model concludes that in the case of a large organic molecule the electron tends to recombine again with the molecular ion instead of escaping from it. In contrast to this interpretation of the charge-pair recombination the reduced ion yield for large molecules was also explained by an increased fragmentation rate of massive species [3].

Transcending 2,000 amu for post-ionization of organic molecules was only successful for large molecular clusters and complexes exceeding that mass [120–123]. Post-ionization of gramicidin_n clusters up to an octomer (n=8) with a mass of 15,040 amu was shown in [120]. We also performed experiments, where high mass clusters up to about 7,500 amu could be photo-ionized (see section 4.1). Other examples of high mass post-ionization are the successful ionization of perfluorinated polyethers with masses up to 7,000 amu [121, 124, 125] and photo-ionization of fullerene clusters [3].

Different mechanisms of post-ionization have been tried, for example *Hyperthermal Surface Ionization* (HSI) where the molecules undergo a charge transfer with a specially prepared surface [126, 127]. The successful detection of laser desorbed insulin ($\approx 5,700$ amu) was shown by using a hot rhenium-oxide surface [128]. However, hyperthermal surface ionization has not yet been developed into a standard technique for the post-ionization of large organic molecules. In spite of all its deficiencies and open questions, photo-ionization still remains an important technique for all applications that operate with neutral particles but have to detect them in the end.

Chapter 2

Experimental realization of the desorption and post-ionization setup

2.1 Setup

This chapter describes the development of our laser desorption source in combination with photo-ionization and time-of-flight mass spectrometry. The design of the source was optimized on the production of a dense beam of *neutral* molecules as required for quantum interference experiments. Figure 2.1 shows a schematic drawing of the setup. After the desorbed molecules leave the source they pass through a 1 mm diameter skimmer about 1-2 cm downstream before they enter the time-of-flight mass spectrometer (TOF-MS). The total distance from the source to the TOF is about 0.5 m. The pressure in the spectrometer chamber is kept at least in the 10^{-6} mbar regime, whereas the pressure in the source chamber depends on the valve settings and ranges from 10^{-5} to 10^{-3} mbar while the desorption is running.

2.1.1 Detection of the molecules

The detection of neutral particles is done via photo-ionization at 157 nm (VUV) or 266 nm (UV) to allow the analysis of the beam in a time-of-flight mass spectrometer.

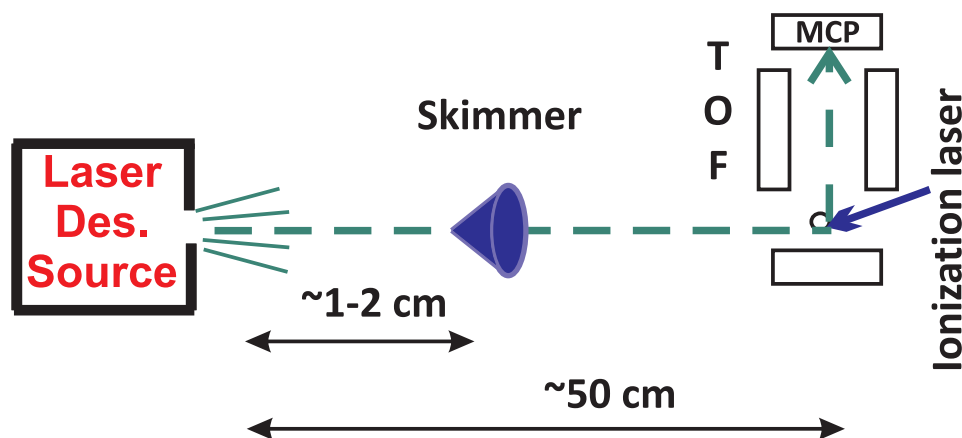


Figure 2.1: Schematic drawing of the setup. The molecules leave the laser desorption source and travel about 0.5 m downstream to the TOF-MS, passing a skimmer in between. Inside the TOF repeller zone an ionization laser crosses the molecular beam perpendicularly. The produced ions are then accelerated by electric fields and are detected at the MCP.

Time-of-flight mass spectrometer

A time-of-flight mass spectrometer (TOF-MS) allows the assignment of masses to the flight times of ionized particles. The ions are pushed by a pulsed electric field (repeller) into a field free drift region. Since all ions obtain the same energy in the electric field, they are accelerated differently depending on their mass. The acceleration results in an earlier arrival of the lighter ions at the multi-channel plate (MCP) detector (Burle Industries Inc.), while heavier ions are retarded.

A multi-channel plate consists of an array of microchannels. When an ion hits the MCP an electron is ejected and the charge pulse gets amplified in an avalanche effect by releasing other electrons, resulting in a measurable voltage peak after many cascades. The voltage peaks for molecular ions hitting the MCP have an amplitude of about 10 mV and a width about ten nanoseconds. The TOF-MS has, besides the repeller and MCP voltage, a liner I, liner II, a lens and a deflection element voltage to be set. The lens and the deflection element are used to focus the ion beam onto the MCP, whereas the two liners are placed inside the drift region. The two drift stages are field free but lie on different potentials, which results in a short acceleration of the ions during the transit from one stage to the other. Our TOF-MS fulfills the

Wiley-McLaren condition [129] to compensate for different starting position of the ions, which would otherwise lead to a broadening of the detected mass peak. Therefore ions of the same mass starting from different positions are accelerated in such a way that all of them arrive at the same moment at the MCP.

Our TOF-MS (Kaesdorf, Munich) has a mass resolution of: $\Delta m/m = 1/500$. Toluol (92 amu), tryptophan (204 amu) and the tryptophan fragment (130 amu) were used for calibration of the low mass range, while gramicidin A (1884 amu) was used instead of the tryptophan fragment for the high mass range calibration. A typical example of a calibration curve is shown in appendix A.

Photo-ionization

Photo-ionization of molecules relies on the fact that the absorption of energy larger than the ionization threshold of the molecule results in an emission of an electron. In contrast to atoms large molecules usually have a rather a dense spectrum of transition lines. This is the reason why absorption in the wavelength range between 260-280 nm is high for molecules with an aromatic group, such as tryptophan [130, 131].

We use a Nd:YAG laser (Spectron) to generate UV light at 266 nm (fourth harmonic) with a pulse duration of 6-9 ns. The laser is focused with a 200 mm lens to a sub millimeter spot in the center of the MS-TOF repeller. The absorption of two photons delivers 9.2 eV, which exceeds the ionization thresholds for most molecules.

For VUV single-photon ionization we used two different excimer lasers emitting at a wavelength of 157 nm (7.9 eV) with 5 ns long pulses. One laser (Coherent Inc., Excistar) emits up to 3 mJ pulses with a maximum repetition rate of 500 Hz, whereas the second laser (Gam Laser Inc., EX5) reaches 1 mJ with a maximal repetition rate of 200 Hz. The VUV beam is focused with a 200 mm lens into the repeller as in the case of the 266 nm laser. At the VUV wavelength the absorption length in air is of the order of nanometers due to the absorption of the radiation by oxygen and water. To prevent intensity losses the beam-path is always purged with dry nitrogen.

2.1.2 Source

Different source designs were tested all of which had their own advantages and drawbacks depending on the desired application. In short, the source consists of the following components:

- A desorption laser to evaporate the molecules on the nanosecond time scale.
- A valve to release a short pulse of a noble gas, which undergoes a supersonic expansion and acts as a cooling seed gas for the desorbed molecules.

Desorption laser

During our work a Nd:YAG (Quantel, Brilliant) laser with a pulse width of 4 ns was used for the desorption process. Our experiments were performed with the tripled output at 355 nm, where successful laser desorption was demonstrated [86, 92, 132]. The energy of the laser can be changed by a rotatable attenuation plate in the beamline, which deflect parts of the beam depending on the angle of incident. This external energy adjustment has the advantage, that the crystals of the laser can be aligned to maximal output, keeping the shot to shot fluctuations minimal. To increase the desorption intensity, the laser beam is focused onto the sample with a lens of typically 200-300 mm focal length .

Valve

The valve (Parker General valve 99; sketched in figure 2.2) is made of a spring which presses a teflon cone (*poppit*) against the orifice. An electromagnet pulls the spring back to open the valve. Different orifices can be screwed onto the valve. If not otherwise mentioned the orifice open diameter in our work was 500 μm . The opening time of the valve can be chosen on the power supply of the valve, but the real opening time depends on the force that presses the poppit against the orifice. The poppit spring is set by screwing the orifice onto the valve housing. In appendix B a comparison of the set opening time and the actual FWHM of the released helium gas pulse is measured with a Fast Ion Gauge (Jordan Co.). We used typically an opening time of the valve between 500 and 700 μs .

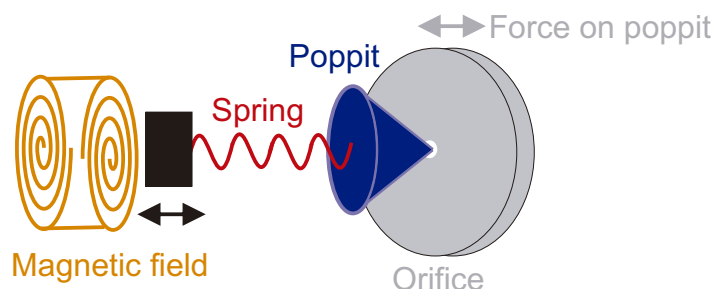


Figure 2.2: Schematic drawing of the valve mechanism. The poppit presses against the orifice of the valve and is opened when a magnetic field pulls back the attached spring.

In order to cool the valve, it is mounted inside a copper block, which is surrounded by a copper tube. By pumping liquid nitrogen through the tube the valve is cooled down, which results in slower seed gas beams. We did not cool the valve below 170 K, since at that temperature the opening mechanism of the valve started to fail. This temperature is still above the condensation temperatures of the used noble gases, which lies for xenon at 161 K and even lower for the lighter gases.

2.1.3 Sample molecules

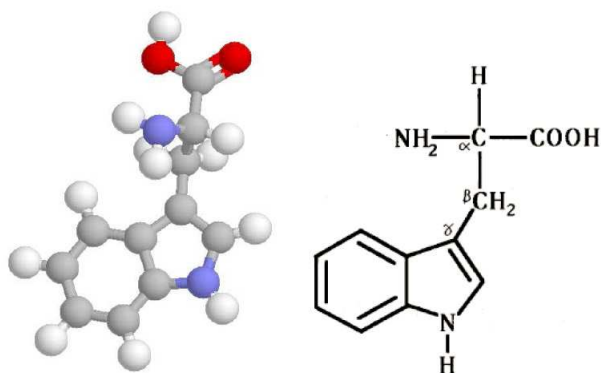


Figure 2.3: 3D plot and structure of the amino acid tryptophan.

Most of the results presented here have been obtained with the amino acid tryptophan and the polypeptide gramicidin. Figure 2.3 shows a 3D picture as well as the structure of tryptophan. The ionization energy of tryptophan was

determined to be 7.3 eV [103,133]. Different gas-phase conformers of tryptophan were identified by spectroscopy [130,134,135]. Ab initio calculations of the tryptophan conformers are presented in [136]. The transition from the ground state to the first excited state in tryptophan has been measured to lie at 286 nm [137]. Since tryptophan has a high density of vibrational states excitation also occurs at the smaller wavelength of 266 nm [114,117].

In order to explore laser desorption with a more complex organic molecule we used gramicidin (see figure 2.4). Gramicidin is an antibiotic polypeptide containing fifteen amino acids. It was purchased as gramicidin D, which contains actually a mixture of the four polypeptides gramicidin A, B, C, and D (see table 2.1 for the abundance and the differences of the four compounds). Their amino acid sequence is HCO-**X**-Gly-L-Ala-D-Leu-L-Ala-D-Val-L-Val-D-Val-L-Trp-D-Leu-L-**Y**-D-Leu-L-Trp-D-Leu-L-Trp-NHCH₂CH₂OH. Gramicidin A-C differs only by a single amino acid at residue 11 (Y), which can be either tryptophan (A), phenylalanine (B), or tyrosine (C). Gramicidin D is derived from gramicidin A by substituting alanine in place of glycine as the first residue (X).

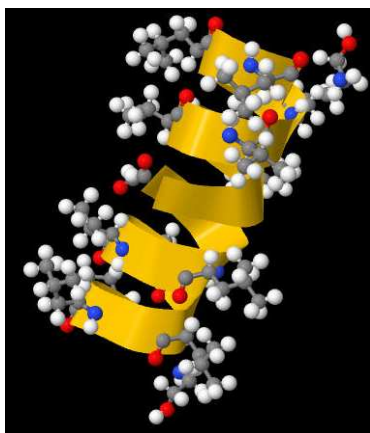


Figure 2.4: *Picture of the polypeptide gramicidin [from the RCSB Protein Data Bank].*

Besides tryptophan and gramicidin several other biomolecules were also used during this thesis. For the desorption experiments presented in section 4.1 a tripeptide containing the amino acids tyrosine, tryptophan and glycine with a mass of 425 amu was used as well as the nucleotide guanine (151 amu) and the amino acid phenylalanine (165 amu).

Gramicidin	X	Y	Weight [amu]	Abundance
A	Gly	Trp	1884	80-85%
B	Gly	Phe	1845	6-7%
C	Gly	Tyr	1861	5-14%
D	Ala	Trp	1898	< 1%

Table 2.1: Abundance of the four polypeptides, which are present in a commercial sample of Gramicidin D [from SigmaAldrich].

We also performed laser desorption of insulin ($\sim 5,700$ amu), myoglobin ($\sim 16,000$ amu) and hemoglobin ($\sim 66,000$ amu). Photo-ionization of these molecules never showed any ion yield and we confirm that the photo-ionization with VUV and UV light of these large biomolecules is difficult to achieve [1–3]. A new type of superconducting detector for neutral molecules as presented in chapter 5 could record velocity distributions for desorbed insulin, myoglobin, and hemoglobin. Due to lack of alternative detectors for these molecules a check if the neutral molecules survives the desorption is still missing.

2.1.4 Free desorption versus mixing channel

The first laser desorption experiments were performed directly in front of the valve as shown in figure 2.5⁴. For this experiment a molecular solution was sprayed onto a 10 cm long aluminum bar with a 2 mm broad edge on top. The bar is mounted in front of the orifice so that the desorbed molecules can be entrained by the expanding seed gas beam. The sample bar can be shifted in every direction to maximize the resulting signal. The molecules sit on the top edge of the bar, which is undercut by 45° to minimize turbulences in the expanding seed gas beam. The bar is moved back and forth by a stepper motor to expose a new sample spot to the desorption laser shining from the top.

For the preparation of the sample the molecules were dissolved in ethanol and sprayed onto the metal bar with an airbrush. After the ethanol evaporated a thin layer of molecules formed. As soon as the valve releases a gas pulse the desorption laser is fired on the sample and desorbs the whole layer of molecules within the reach of its beam waist into the supersonically ex-

⁴This source setup is similar to the one used in [61].

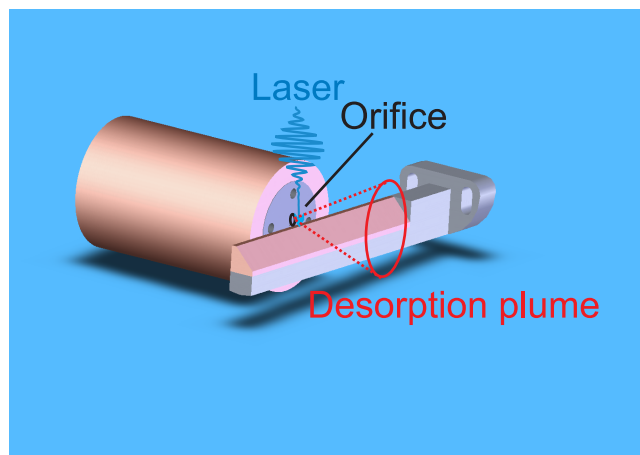


Figure 2.5: Drawing of the free expansion laser desorption setup. The laser evaporates the molecules next to the orifice of the valve. The desorbed molecules leave the source with the seed gas in the forward direction. The valve is mounted inside a copper cylinder used for cooling of the valve.

panding gas beam. This method keeps shot to shot fluctuation due to sample inhomogeneities at a low level, but each spot on the sample can only be used once. The molecules are 'kicked' by the carrier gas atoms into the forward direction of the gas beam and they are cooled by collisions with the carrier gas atoms.

The desorption into the freely expanding gas jet succeeded in generating a translationally cold tryptophan beam as presented in section 2.2. But the experiments with the ten times heavier gramicidin A (1881 amu) gave no detectable signal. This led us to modify the desorption setup, since an explanation for the missing gramicidin signal may be that the interaction i.e. the number of collisions with the seed gas is too low to accelerate them into the forward direction.

In order to increase the number of collisions the source design was changed such that the desorption process is performed in a closed volume (*mixing channel*) screwed directly onto the valve. Slightly different designs of the mixing channel than presented here can be found for example in [138, 139]. Two different designs of the straight mixing channel shown in figure 2.6 were tried. The first channel had 4 mm in diameter, a length of 300 mm ending in a conical exit and a 2 mm diameter opening for the desorption laser. The second model had a small 2 mm diameter channel, while the other dimension

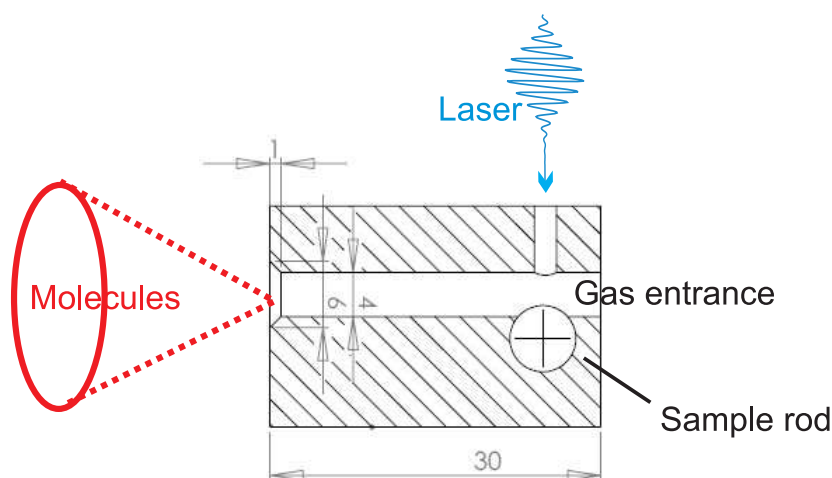


Figure 2.6: Drawing of the straight mixing channel. The sample is pressed onto a rod, which is threaded from the top into the channel (scales are in millimeters). A second version of the mixing channel had a reduced channel with only 2 mm in diameter.

were not changed.

The analyte molecules were pressed onto a threaded rod which could be screwed from the top into the mixing channel. A motor on top of the rod slowly rotated the sample, thereby screwing it in and out to expose new sample molecules to the desorption laser. Desorbed molecules were leaking out at two sides of the mixing channel. One opening was at its bottom part, since the thread in the mixing channel for the sample rod was a clearance hole. The second opening was the entrance for the laser. To close the laser entrance a glass plate was glued onto the entrance hole. In principle the desorption still worked, but the window melted/cracked rather quickly due to the laser light going through. The reason for this fast damage was that desorbed molecules stuck on the inner surface of the window, increasing the absorption and heating of the window dramatically.

For pressing the molecules onto the rod a mechanical press is used [140]. To provide better stabilization against crumbling of the pressed samples, cellulose, an organic compound of unspecified chain length, is mixed 1:1 with the analyte molecules. Without the use of cellulose the pressed samples are soft and the molecules tend to fall off rather easily. Typically about 1 g of powder is needed for pressing a sample rod. Figure 2.7 shows pictures of the rod with molecules pressed on it before and after laser desorption. Clearly

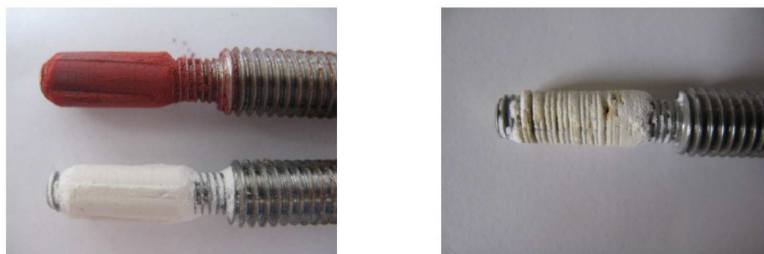


Figure 2.7: Pictures of the sample rod with pressed molecules. Left: Tryptophan and β -carotene samples. Right: Tryptophan after laser desorption. The grooves left by the laser desorption process are clearly visible.

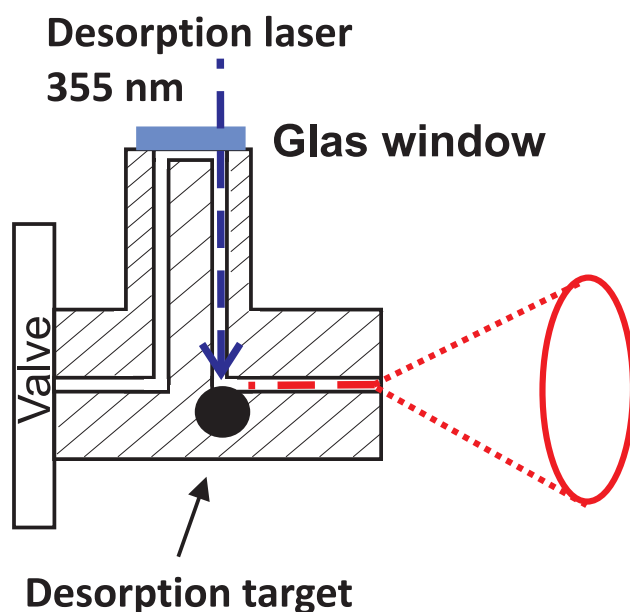


Figure 2.8: Drawing of the closed mixing channel. The seed gas is directed around three corners, which allows to prevent sticking of desorbed molecules to the window. The tube piping the gas from the entrance to the part with the glass plate has 3 mm in diameter. The channel leading from the glass plate to the exit is 6 mm in diameter and ends in a removable 1 mm diameter orifice [122, 123].

visible are the grooves the desorption laser is shooting into the sample surface leading to an inhomogeneous sample surface with the time.

In order to avoid a loss of seed gas during the desorption process through the mixing channel's openings, it was redesigned in such a way that the exit orifice was the only opening into the vacuum (see figure 2.8), i.e. we obtained a 'closed mixing channel'. Therefore the threaded hole for the sample rod was changed from a clearance hole to a blind one. The entrance for the desorption laser was covered by a glass plate, but it had to be protected from desorbed molecules covering it from the inside. This could be achieved by piping the seed gas three times around a 90° corner such that the gas flows in the same direction as the laser light is shining on the sample. The desorbed molecules would have to pass upstream against the flow of the seed gas beam to reach the glass window. Each gas pulse released by the valve additionally cleans the window from inside while passing it. In this way the window is protected from molecules and the overheating and melting of the glass window could be eliminated completely. The exit of the mixing channel has a removable cap with a 1 mm diameter exit orifice, where the gas molecule mixture can undergo a supersonic expansion into the vacuum.

2.1.5 Control and alignment of the setup

Timing

Since the valve, the lasers and the TOF-MS only work in a pulsed mode, the triggers for all devices have to be synchronized. As a master trigger a TTL pulses with 20 Hz is generated by a National Instruments card and fed into a pulse generator (Berkeley Nucleonics Corporation, 575-8C), which generates individual trigger pulses for each device. The limiting factor for the repetition rate are the flashlamp-pumped lasers, which can not be operated above 20 Hz repetition rate. In figure 2.9 the timing sequence of the valve, desorption laser, ionization laser and repeller is shown for a flight distance of 0.5 m. For the valve and the repeller the trigger width also defines their opening time, whereas the laser triggers define only the starting moment of the light pulse. As shown in figure 2.9 the repeller is delayed by a few microseconds with respect to the ionization laser. This has the advantage that the jitter of the ionization laser in the range of a few microsecond does not result in a broadening of the peaks in the mass spectra due to different starting moments of the ions. Since the ions are produced before the repeller

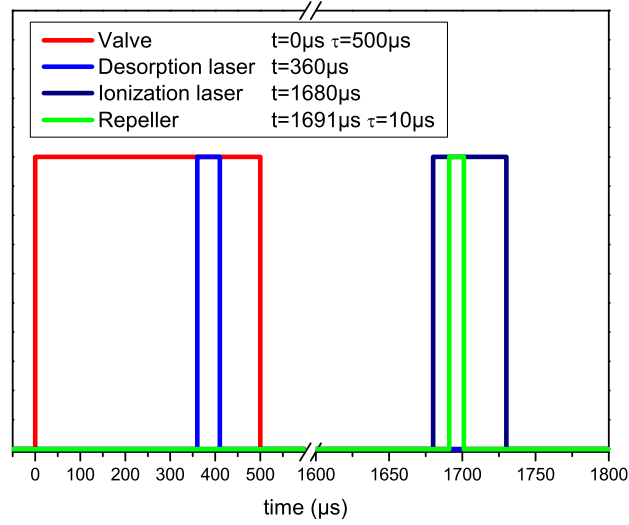


Figure 2.9: Typical timing of the four devices valve, desorption laser, ionization laser and repeller for a molecular flight distance of 0.5 m. The shown pulses are already corrected for internal delays of the devices. The trigger widths of the valve and the repeller define also their opening time.

is opened, all of them start simultaneously when it opens.

To scan the velocity distribution the time between the desorption laser and the ionization laser has to be varied by keeping the time interval of the valve-desorption laser and ionization laser-repeller fixed. This can be done by hand directly at the pulse generator, but during the course of the experiment it was automatized by a self written Labview program, which controlled the pulse generator and the data acquisition. The velocity of the molecules is calculated by dividing the flight distance by the flight time. The flight time is given -if not mentioned otherwise- by the time difference between the desorption and the ionization time. For the closed mixing channel we found that the ejection of the molecules is actually delayed with respect to the desorption, which results in an underestimation of the velocities, as will be discussed in section 2.3.1. The velocity distributions presented in our work are a selection of recorded data, which show variations of about 20% for the velocities and up to about 50% for the widths, although the experimental parameters are chosen to be identical. This is due to the fact that some of the experimental parameters of the source are rather critical. The most important ones among them are the alignment of the source and the focus of the desorption spot after the sample rod has been changed.

The thickness of each pressed sample varies slightly and replacing the rod requires a new alignment of the mixing channel, which both leads to a change of the desorption focus and consequently to a change of the deposited energy. All presented data on the variation of one of the desorption parameters e.g. different seed gases are recorded by changing only the mentioned parameter and keeping the rest as fixed as possible. Therefore a relative trend in one or the other direction can be concluded by probing a single parameter, although the absolute values between the different sets of measurements may still vary.

Signal readout

The output of the multi channel plate is amplified by a factor of 50 to 100 before the mass spectra is displayed on an oscilloscope (500MHz) with the repeller pulse as trigger. Additionally the signal of a single mass peak can also be recorded by a boxcar integrator (Stanford Research Company). A boxcar integrator integrates an electronic input signal within defined timing limits (box) and converts the corresponding area into an output signal. Two separated boxcar integrators were used, which allowed the simultaneous recording of two separated mass peaks within one mass spectrum or the recording of the same mass peak at two different velocities. With a Labview program the digitized signals from the oscilloscope and the boxcar integrators could be read into a computer for further analysis. The presented mass spectra and velocity distributions were averaged over 30 desorption shots (if not mentioned otherwise).

Alignment of the setup

In order to align the source with respect to the repeller's entrance opening, an optical alignment procedure was used. A laser diode entering from the back of the vacuum chamber was aligned such that it passed the middle of the repeller and the skimmer and shone on the opening of the mixing channel thereby defining the molecular flight path. The source was moved to a position so that the laser beam hit a mirror next to the source's orifice and it was tilted until the reflected beam overlapped with the incident laser beam. After that the source could be moved without changing the tilt angle by a xy-stage to a position, where the laser beam hits the orifice. This procedure ensured that the signal could be found easily and only slightly further real-time alignment was needed.

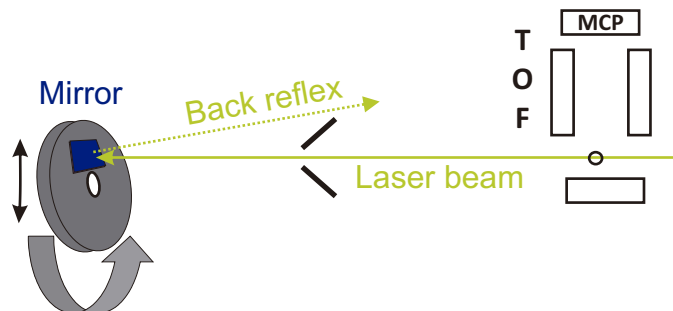


Figure 2.10: For alignment of the source a laser beam shines parallel to the molecular beam line. A mirror on the source is used for backreflection of the laser beam. The source is tilted until the laser is reflected back into the incident beam. Afterwards the source is moved in the xy -plane until the laser hits the orifice.

2.2 Results of the laser desorption source

2.2.1 Free desorption

The first desorption experiments were performed by the desorption of tryptophan next to the orifice of the freely expanding seed gas beam [141]. Figure 2.11 shows a mass spectrum of tryptophan entrained into an argon seed gas beam. Tryptophan at the mass of 204 amu is clearly the largest signal for a desorption energy of 3.3 mJ at 355 nm and an ionization energy of 2.6 mJ at 266 nm. The peak at 130 amu is a fragment of tryptophan corresponding to the indole ring, whereas toluol, which was used for calibration of the setup appears at 92 amu. Figure 2.12 shows the velocity distributions for desorbed tryptophan into a seed gas beams of argon and xenon at room temperature as well as into an argon beam with the valve cooled to 173 K. The velocity distributions are fitted by a Maxwell-Boltzmann distribution given by eq. 1.14. The width of the distribution corresponds to the translational temperature T_{MB} , whereas v_0 gives the flow velocity. Desorption of tryptophan into a room temperature argon beam, as plotted in figure 2.12 (top), results in $v_0=556$ m/s and a corresponding temperature of $T_{MB}=91$ K. The velocity fits the theoretical expected velocity of a supersonic argon beam as plotted in figure 1.2. Using the heavier seed gas xenon (figure 2.12 center) results in a slower and colder tryptophan beam with $v_0=343$ m/s and $T_{MB}=16$ K. Reducing the velocity of the beam by cooling the seed gas prior to the ex-

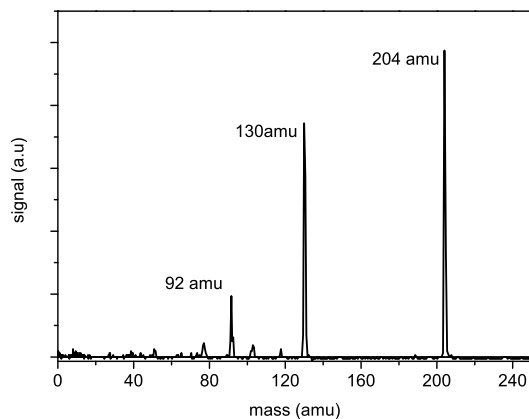


Figure 2.11: Mass spectrum recorded after desorption of tryptophan into a freely expanding argon seed gas beam. The intact tryptophan molecule appears at a mass of 204 amu, whereas at 130 amu a tryptophan fragment appears and the peak at 92 amu stems from toluol which was mixed into the seed gas for calibration of the setup. Desorption: 3.3 mJ (355 nm); Ionization: 2.6 mJ (266 nm); Backing pressure: 2 bar.

pansion was tried in the case of argon. The valve was cooled to 173 K and the desorption of tryptophan led to the velocity distribution shown in figure 2.12 (bottom) with $v_0=397$ m/s and $T_{MB}=66$ K.

In summary, the free desorption in front of the valve resulted in a translationally cold beam of tryptophan molecules. Increasing the seed gas mass or cooling of the valve results in a reduced velocity as well as in a lower translational temperature of the molecular beam. Desorption of the ten times heavier gramicidin did not result in any detectable signal for the polypeptide. The reason is probably that the number of collisions is insufficient to 'kick' the molecules into the forward direction. Since the goal of our work was to develop a source for complex biomolecules the free desorption was not investigated further, but a mixing channel was used instead.

2.2.2 Straight mixing channel

Figure 2.13 (left) shows the mass spectrum of gramicidin desorbed inside the 4 mm diameter straight mixing channel plotted in figure 2.6. The mass spectrum results only in gramicidin and a fragment peak at 130 amu, which is very likely a tryptophan fragment. Independent of the desorption or ionization setup used, the gramicidin mass spectrum never showed any fragments

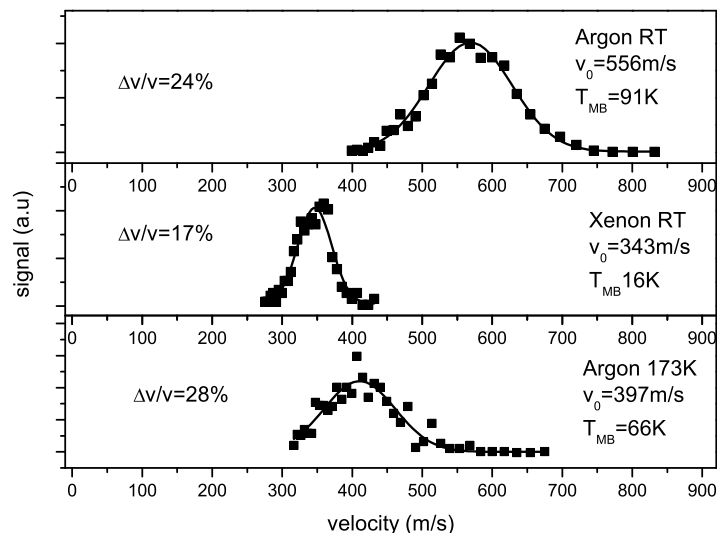


Figure 2.12: Velocity distributions for tryptophan desorbed into three freely expanding seed gas beams: argon and xenon at RT, as well as argon at 173 K. Backing pressure: 2 bar; Desorption: 1.6 mJ (355 nm); Ionization: 3.2 mJ (266 nm).

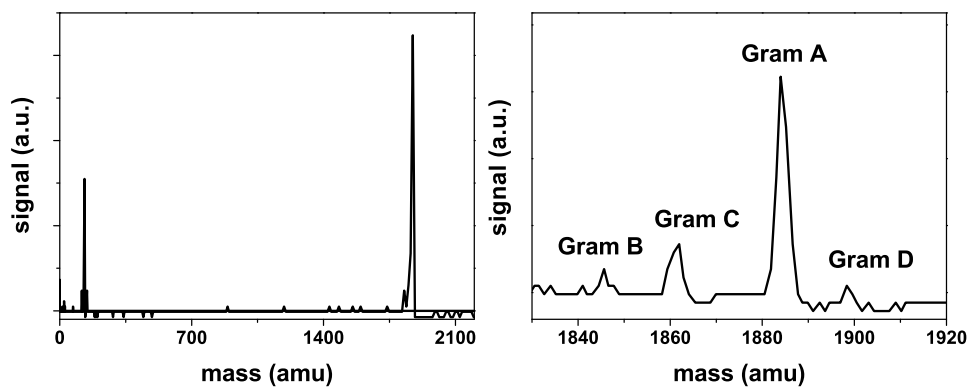


Figure 2.13: Left: Mass spectrum of gramicidin after laser desorption inside the 4 mm open mixing channel. Seed Gas: Argon 2 bar; Desorption: 11 mJ (355 nm); Ionization: 1 mJ (157 nm). Right: Mass spectrum of the four gramicidin molecules in a gramicidin D sample desorbed in the closed mixing channel. Ionization: 3.6 mJ (266 nm); Seed Gas: Argon 2 bar; Desorption: 8 mJ (355 nm).

between 200 amu and the parent ion peak. Figure 2.13 (right) shows a high resolution mass spectrum of gramicidin, where the four gramicidin molecules, which are present in the gramicidin D sample could be resolved (see table 2.1). If not mentioned otherwise all references concerning gramicidin in our work regard the gramicidin A molecule with a mass of 1884 amu.

Figure 2.14 (left) shows a velocity distribution of desorbed tryptophan using the 2 mm straight mixing channel which results for argon in $v_0=479$ m/s and $T_{MB}=129$ K. The velocity of tryptophan is slower than the expected argon velocity, which can be related to several factors. First, the mixing channel may delay the starting point of the molecules, which results in an underestimation of the molecular speed. This effect is observed for the closed mixing channel and is investigated in section 2.3.1 in detail. Another possibility for the reduced tryptophan speed is that the hot molecules do not thermalize completely with the seed gas, if too much seed gas is leaking out at the mixing channel's openings. The velocity of the molecules must be a convolution of the velocity distributions of the seed gas beam and the desorbed molecules. This leads to all kinds of mutual slowing or acceleration depending on the number of collisions and the momentum transfer per kick, which is different for the different seed gases and molecule masses.

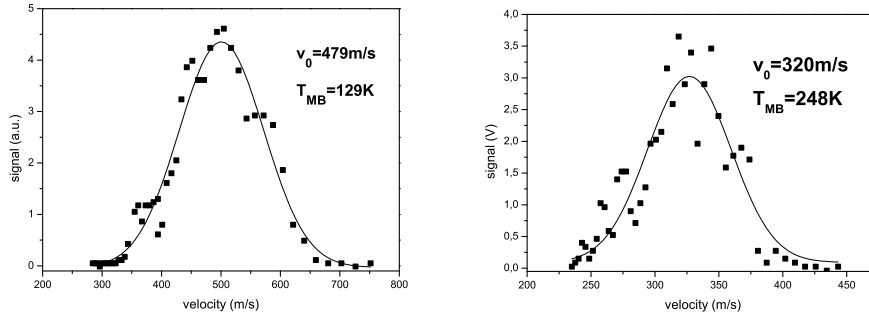


Figure 2.14: Left: Velocity distribution of tryptophan desorbed inside the open 2 mm mixing channel. Ionization: 0.7 mJ (266 nm); Seed Gas: Argon 1 bar; Desorption: 7 mJ (355 nm). Right: Velocity distribution of gramicidin desorbed inside the open 2 mm mixing channel. Ionization: 1 mJ (157 nm); Seed Gas: Argon 1 bar; Desorption: 15 mJ (355 nm).

A velocity distribution for gramicidin recorded with the 2 mm mixing channel and the seed gas argon is shown in figure 2.14 (right), which gives

$v_0=320\text{ m/s}$ and $T_{MB}=248\text{ K}$. As expected, the translational temperature of the heavier molecule is broader in contrast to the lighter tryptophan. Comparing the velocities of tryptophan with those of gramicidin reveals a velocity reduction of 33% for gramicidin when using argon as the seed gas. This leads us to suspect that the reason for the reduced velocity of the organic beam is rather the insufficient number of collisions, since this would result in a mass dependent velocity slip as observed.

Besides the 2 mm diameter mixing channel, the larger 4 mm diameter mixing channel was also tested in the desorption experiments. In figure 2.15 (left) the velocity distribution of tryptophan resulting from the open 4 mm mixing channel is plotted for the seed gas argon. The fitted Maxwell-Boltzmann distribution is defined by $v_0=554\text{ m/s}$ and $T_{MB}=255\text{ K}$.

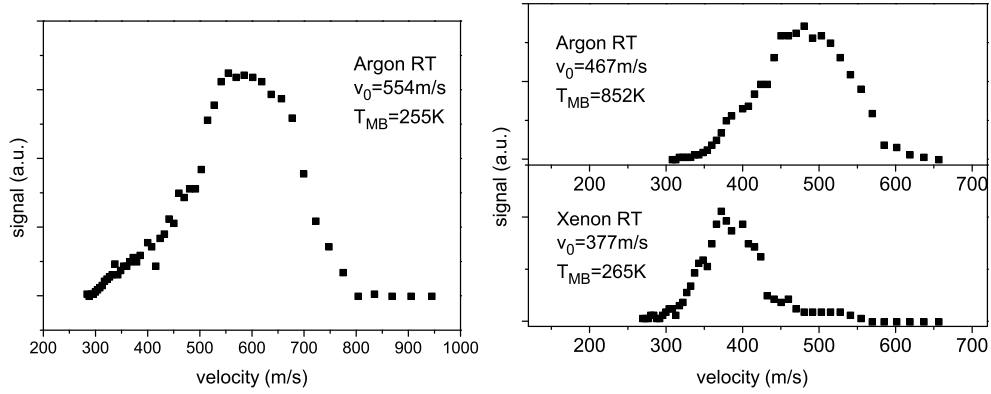


Figure 2.15: Left: Velocity distribution for tryptophan desorbed inside the 4 mm mixing channel for argon at room temperature. Seed gas pressure: 2 bar; Desorption: 7.5 mJ (355 nm); Ionization: 1 mJ. (157 nm) Right: Velocity distribution for gramicidin desorbed inside the 4 mm mixing channel into argon and xenon at room temperature. Seed gas pressure: 2 bar; Desorption: 11 mJ (355 nm); Ionization: 1 mJ (157 nm).

For the desorption of gramicidin inside the 4 mm straight mixing channel the recorded velocity distributions for the seed gases argon and xenon at room temperature are shown in Figure 2.15 (right). The fit for the gramicidin beam results in $v_0=467\text{ m/s}$ and $T_{MB}=852\text{ K}$ for argon and in $v_0=377\text{ m/s}$ and $T_{MB}=265\text{ K}$ in the case of xenon. The translational temperature of gramicidin is about a factor of three larger as in the case of tryptophan. Whereas the velocity of tryptophan is in agreement with the expected argon speed, the heavier gramicidin is about 100 m/s slower. Increasing the seed

gas mass resulted for both channel diameters in a decreased velocity as well as in better cooling of the translational temperature, but also in a decreased signal.

The two mixing channels, as presented so far, have one major drawback. Gas and desorbed material leaks out of the opening for the sample rod on the bottom side of the channel and also at the entrance hole for the desorption laser. To eliminate this problem, of losing gas and molecules, the mixing channel was rebuilt to a closed version (see figure 2.8), where a 1 mm orifice at the exit of the channel is the only opening leading into vacuum.

2.2.3 Closed mixing channel

The velocity distribution of tryptophan desorbed in the closed mixing channel with the different seed gases argon, krypton and xenon is shown in figure 2.16. A Maxwell-Boltzmann fit results for argon in $v_0=373$ m/s and

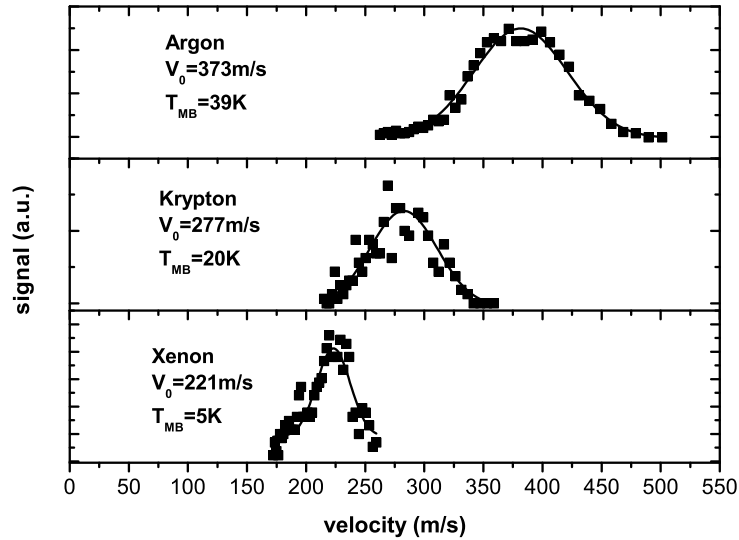


Figure 2.16: Velocity distribution of tryptophan for the three different seed gases argon, krypton and xenon desorbed in the closed mixing channel. Seed gas pressure: 2 bar; Desorption: 4 mJ (355 nm); Ionization: 3.2 mJ (266 nm).

$T_{MB}=39$ K. In the case of krypton the velocity distribution gives $v_0=277$ m/s and $T_{MB}=20$ K, i.e. a slower and colder beam. Using xenon as seed gas results in $v_0=221$ m/s and $T_{MB}=5$ K. The velocity distributions in the case of gramicidin desorption are plotted in figure 2.17 for argon, krypton and

xenon. For argon the Maxwell-Boltzmann fit results in $v_0=307\text{ m/s}$ and $T_{MB}=143\text{ K}$, i.e. significantly broader than for tryptophan. For krypton the fit gives $v_0=247\text{ m/s}$ and $T_{MB}=25\text{ K}$ and for xenon the fit parameters are $v_0=206\text{ m/s}$ and $T_{MB}=20\text{ K}$. The velocities for tryptophan as well as for gramicidin are significantly slower, as theoretically expected, for all used seed gases. One reason for that is a misinterpretation of the velocity due to a delayed starting moment as will be discussed in section 2.3.1.

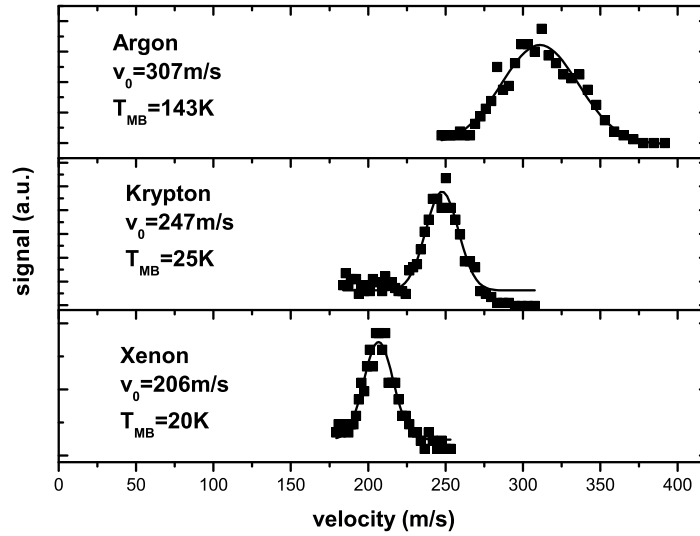


Figure 2.17: Velocity distribution of gramicidin for the three different seed gases argon, krypton and xenon desorbed in the closed mixing channel. Seed gas pressure: 2 bar. Desorption: 7 mJ (355 nm); Ionization: 4 mJ (266 nm).

To summarize this section of the different source designs: Increasing the mass of the seed gas from argon to heavier noble gases results in slower and colder beams for all source designs, but it is also accompanied by a decrease of the total signal. The signal loss is about a factor of 50 to 100 when replacing argon by xenon. This effect is generally attributed to the recoil in collisions with more massive particles. In the case of the free desorption the source was tested successfully for tryptophan, whereas the desorption of larger biomolecules only succeeded inside a mixing channel.

2.3 Further improvements of the laser desorption source

All experiments shown so far were performed in a setup with a flight distance from the source exit to the repeller of about 0.5 m as shown in figure 2.1. Figure 2.18 shows a drawing of the complete setup with the closed mixing channel, chopper, interferometer chamber and TOF-MS. The total flight dis-

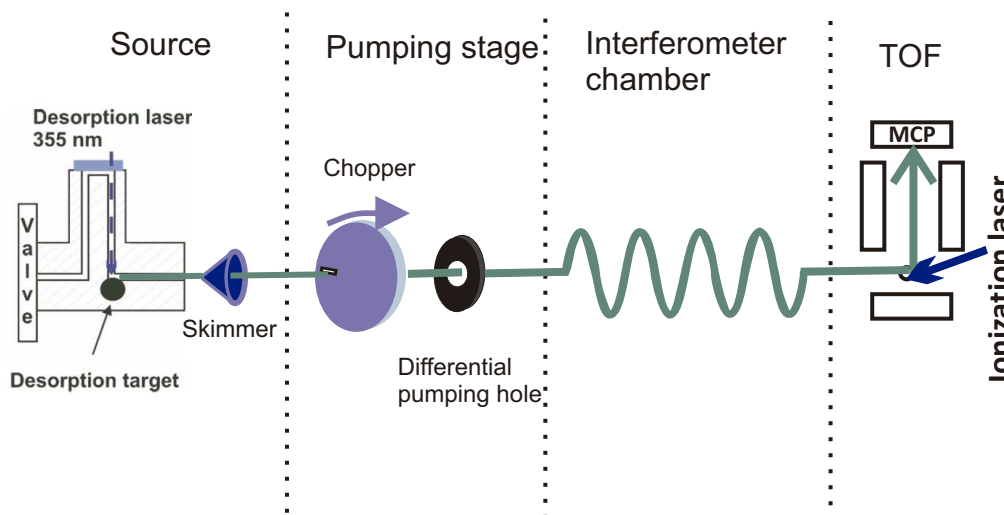


Figure 2.18: Interferometer setup from front to end: Source, differential pumping stage with chopper for velocity measurements, interferometer chamber and TOF-MS. The distance from the source to the TOF was 2.5 m and was reduced later to 1.7 m by shortening the interferometer chamber.

tance from source to the mass spectrometer thus increased to 2.5 m. Besides the geometric signal loss also the three interferometer gratings decreased the signal by about 30% each. Due to these losses no molecular signal could be detected in that setup with argon as the seed gas. Only after argon was replaced by the lightest noble gas, i.e. helium, the signal could be sufficiently gained. The signal increased by about a factor of 200 when using helium instead of argon. Therefore for the further source characterization helium is used as the seed gas. If future interference experiments want to make use of beams produced with the heavier seed gases, because slower velocities result in longer deBroglie wavelengths, they need to be suitable for less intense beams. This can be achieved for example by using shorter interferometers

and phase gratings made of standing light waves, which do not decrease the beam intensity [13, 14, 32].

2.3.1 Velocity measurements

The desorption of various molecules showed almost no difference in velocity for the different masses under the same experimental conditions. The simultaneous desorption of the two different molecules tryptophan and β -carotene showed no velocity slip. A second example will be discussed in section 4.1, where large clusters of tryptophan, which formed during laser desorption, could be observed. These only showed a velocity slip of 5% in the range from 400 to 2,200 amu.

In principle the velocity of the molecular beam can be known with high precision for laser desorption/ionization techniques. The nanosecond pulses define the start and arrival times very well. For a 500 m/s molecule and a flight distance of 0.5 m the velocity uncertainty Δv due to the pulse durations is $\Delta v = 5 \cdot 10^{-3}$ m/s. In case of desorption inside the mixing volume it may, however, happen that the molecules are delayed due to diffusion inside the mixing channel. Their exit from the source is then retarded with respect to the desorption. Neglecting this effect means overestimating the actual flight time, which results in underestimating the molecular velocity. To overcome this uncertainty and in order to have an independent trigger signal for the free beam a chopper was installed in the differential pumping stage of the interferometer (see figure 2.18).

The chopper was a 10 cm diameter steel plate with a 1 mm broad and 5 mm long rectangular slit as depicted in figure 2.19. The total distance from the source exit to the repeller was 1.7 m in the chopper experiments. The chopper rotated at 20 Hz, which resulted in an opening time of $83 \mu\text{s}$ for the slit. Figure 2.20 shows the velocity distribution of tryptophan in helium without a chopper (black line) resulting in $v_0 = 442$ m/s and $T_{MB} = 9$ K. The green line represents the curve measured with the chopper inserted and taking the chopper opening as the starting point for the molecules. The Maxwell-Boltzmann fits results in $v_0 = 816$ m/s and $T_{MB} = 56$ K for the measurement with the chopper as external reference. The channel-related time-lag, i.e. the residence time of the molecules inside the mixing channel, can then be calculated. The distance from the chopper to the ionization point is 138.5 cm, whereas there are 33 cm between the mixing channel and the chopper. Since

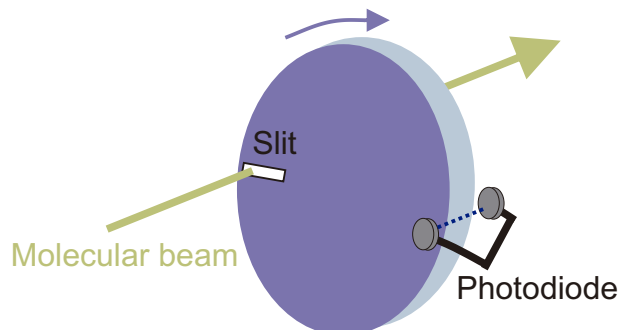


Figure 2.19: Sketch of the chopper with the 1 mm broad slit. A photodiode is used to calibrate the chopper opening with respect to the molecular beam.

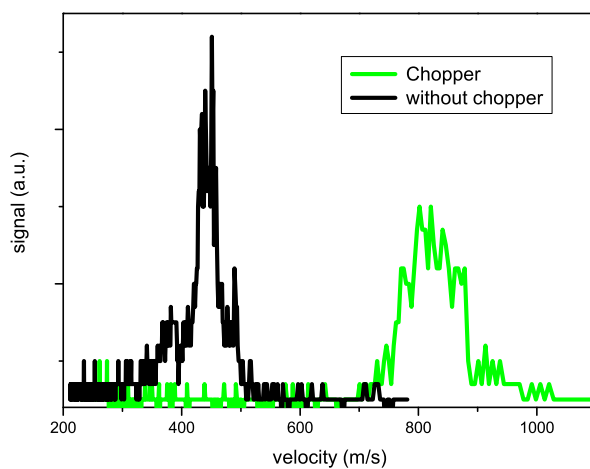


Figure 2.20: Velocity distributions for tryptophan desorbed in the closed mixing channel. Black curve: Velocity (resulting from the time-of-flight curve) measured without the help of a chopper. The velocity is calculated by taking the desorption/ionization time as starting/arrival time. Green: A chopper is inserted in the beam line and used as the external starting point, which reveals the true molecular velocity. Seed gas: Helium 2 bar. Data not averaged.

the measurement with the chopper reveals a real velocity of 816 m/s the molecules take 2.1 ms from the source exit to the mass spectrometer. The total measured time between the desorption and the ionization pulse is 3.6 ms, which results in a drift time inside the mixing channel of 1.5 ms.

The helium beam is still more than a factor of two slower than expected for a fully supersonic helium beam. Two main reason for that could be the following: First, a velocity slip exists between the helium seed gas and the embedded molecules. Or second, the supersonic expansion from the valve into the mixing channel is slowed down due to the meandering channel. The increased volume in the mixing channel may not allow for the required pressure difference to reach the full supersonic speed during the expansion out of the channel.

The extended nozzle residence may also explain why the measured velocities for argon, krypton and xenon in the previous section were slower than expected.

2.3.2 Signal stabilization

The combination of laser desorption with matter wave interferometry demands that the molecular beam is stable and reproducible.

The signal fluctuations in laser desorption have several reasons. Both the stability of the desorption and the stability of the ionization laser are crucial for the number of desorbed/ionized particles. The 157 nm excimer lasers have a shot to shot fluctuation of less than 1%. Slightly higher fluctuations has the flashlight pumped frequency quadrupled Nd:YAG desorption laser, which reaches a typical shot to shot stability around 5%. The biggest source of signal fluctuations is the sample. The desorption laser shoots grooves into the sample (see figure 2.7). This results in an uneven surface, which influences the process of laser desorption. Also crumbling of the sample cannot be avoided and leads to an uneven sample surface.

A solution to these problems would be to use only monolayers of analyte molecules, where the number of desorbed molecules per pulse is relatively fixed. The decision to rather use a larger amount of pressed molecular powder instead of thin layers has the advantage that the experimental usage time of the sample is increased.

The detected signal sometimes varies up to 50%. In order to be able to use the source for interferometry at least 10% signal stability should be

obtained. Under the assumption that each desorption shot produces a similar Maxwell-Boltzmann distribution, the ratio between two different velocity classes within a single distribution is a constant for all distributions even if the total number of desorbed molecules varies. We used two different lasers for probing the velocity distribution. One laser was the 157 nm excimer laser and the other one was the Nd:YAG with its forth harmonic at 266 nm. The method is tested in the setup shown in figure 2.1, where the two lasers were shining from opposite sides into the repeller of the time-of-flight mass spectrometer, as depicted in figure 2.21. Figure 2.22 shows the tryptophan signal

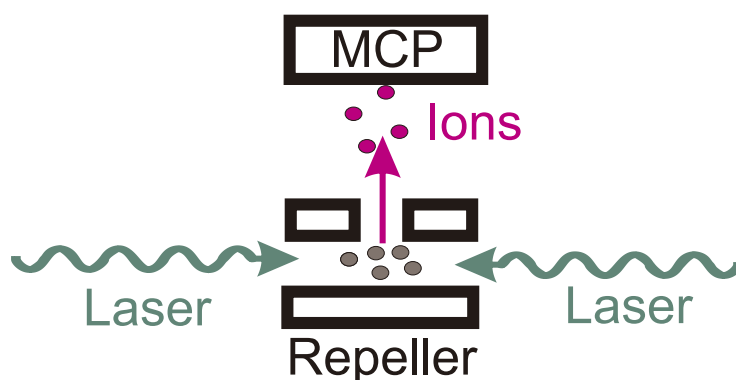


Figure 2.21: Two independent lasers were used to probe the ratio of two different velocity classes. The molecular beam enters the TOF-MS perpendicular to the page and both lasers ionize the molecules with a time difference of $12\mu\text{s}$.

recorded with the VUV and the UV laser separately as well as the ratio of the two signals (blue line). The individual signals vary up to 25%, whereas the ratio UV/VUV is stable within 6%. The experiments confirm that normalization enhances the signal stability as long as the time lag between the two laser shots is not too large. We used a pulse separation of $12\mu\text{s}$ corresponding to a molecular velocity difference of 15 m/s. The details of signal stabilization in combination with interferometry is explained in appendix C.

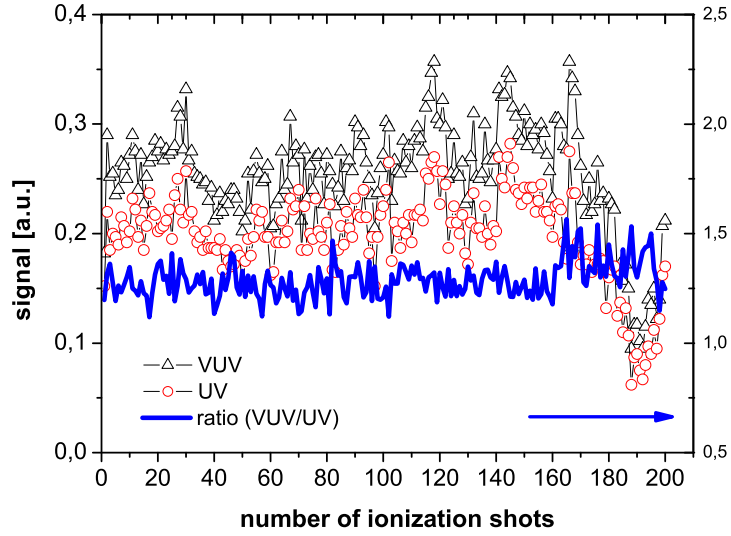


Figure 2.22: Signal of ionized tryptophan for 200 ionization shots [123]. The ratio of the UV (circles) and VUV (triangles) ion signal allows to suppress source dependent fluctuations. Data points were not averaged.

2.4 Comparison of 157 nm versus 266 nm ionization

To maximize the signal yield we examined the ion yield for different ionization wavelengths. The two molecules tryptophan and gramicidin are examined for their different VUV (157 nm) and UV (266 nm) ionization behavior. For this comparison the setup is used, as shown in figure 2.1. The two lasers shine through the repeller of the time-of-flight mass spectrometer from opposite directions as shown in figure 2.21. Both beams are shaped to circular profiles with $5\text{ mm} \pm 1\text{ mm}$ diameters and are overlapped in the middle of the repeller. The error of the laser intensity and the ion yield signal is estimated to be about 20%.

In the case of tryptophan the ionization with UV light at 4.66 eV requires at least a two photon absorption. In figure 2.23 the ionization yield for tryptophan as a function of different laser intensities at 266 nm is plotted. The ion yield increases until above an intensity of about 4 MW/cm^2 a saturation plateau is reached. The data is fitted well by a saturation curve for a resonant

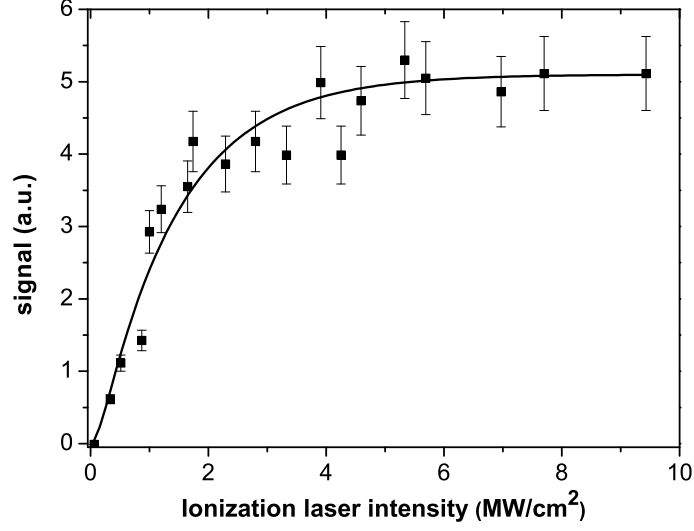


Figure 2.23: The ionization yield of tryptophan for different UV (266 nm) laser intensities [123]. The solid line is a fit using eq. 2.1.

two-photon ionization process [142]:

$$S(I) \propto 1 + \frac{e^{-(s_1+s_2)I\tau/(2h\nu)}(s_1 - s_2)}{2s_2} - \frac{e^{-(s_1-s_2)I\tau/(2h\nu)}(s_1 + s_2)}{2s_2}, \quad (2.1)$$

with $s_1 = 2\sigma_1 + \sigma_2$ and $s_2 = \sqrt{4\sigma_1^2 + \sigma_2^2}$. The laser intensity is denoted with I , h is Planck's constant, ν is the laser frequency and τ represents the laser pulse duration. While σ_1 denotes the one-photon cross section for the first transition from the ground state to the intermediate state, σ_2 is the coefficient to lift the electron from the intermediate state into the continuum.

The fit to the data in figure 2.23 with eq. 2.1 results in the cross sections $\sigma_1 = 1.0(4) \times 10^{-16} \text{ cm}^2$ and $\sigma_2 = 6(4) \times 10^{-16} \text{ cm}^2$ for the two-photon absorption in tryptophan at 266 nm.

For single-photon ionization at 157 nm the increase of the laser intensity should result in a linear dependence of the ion yield. Figure 2.24 shows the ion yield for tryptophan for different VUV laser intensities, which shows the expected linear dependency. In the available energy range of the excimer laser no saturation of the signal yield is observed. The total ion yields of tryptophan are comparable for both UV and VUV light at the same laser intensities.

In the case of gramicidin the comparison of the two ionization wavelengths is plotted in figure 2.25. Interestingly, the VUV ionization outperforms the

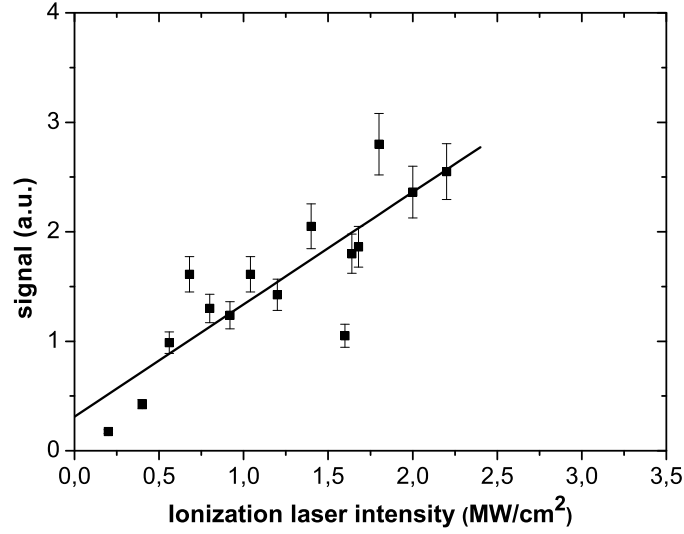


Figure 2.24: The ionization yield of tryptophan for different VUV (157 nm) laser intensities [123]. The solid line is a guide for the eye.

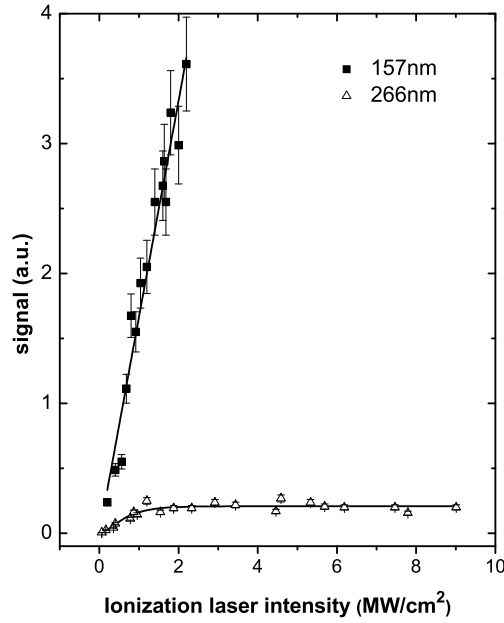


Figure 2.25: Ion yield of gramicidin A as a function of the laser intensity at 266 nm and 157 nm. The UV signal follows a saturated two-photon absorption curve (eq. 2.1), whereas the VUV signal is represented by a linear increase up to the maximal available VUV intensity of 2.2 MW/cm² [123].

signal for the UV wavelength by a factor of fifteen(!) at the maximal available VUV intensity of 2.2 MW/cm^2 . The VUV curve shows a linear increase with intensity, whereas the UV ionization yield saturates, like in the case of tryptophan. The fit of the saturated UV curve with eq. 2.1 results in $\sigma_1 = 6(2) \times 10^{-16} \text{ cm}^2$ and $\sigma_2 = 3(1) \times 10^{-16} \text{ cm}^2$. It should be noted that it is not clear if the saturated two-photon curve is still valid in the case of gramicidin, since the ionization process is not known. The observation that the UV absorption spectra of tryptophan and gramicidin in solution are rather similar [143] suggests that it is actually the tryptophan inside the gramicidin molecules which ionizes. Assuming that, the fit with eq. 2.1 would be correct.

In summary, ionization with 157 nm instead of 266 nm light results in a fifteen times higher signal in the case of gramicidin, whereas for tryptophan the signals are comparable for similar laser intensities, but high intensities can be reached with UV lasers resulting also in a higher ion yield.

Part III

Applications of the laser desorption source

Chapter 3

Towards biomolecule interferometry

3.1 Laser desorption as a source for biomolecule interference

The Talbot-Lau interferometer consists of three identical gratings as shown in figure 3.1. The first grating is used to prepare the coherence of the molecules, which are emitted by the incoherent laser desorption source. The expanding molecular waves pass the second grating and reproduce its periodicity at the Talbot length. In order to resolve this interference pattern an additional third grating is put at the Talbot distance L_T . As shown in figure 3.1 the third grating can be moved stepwise perpendicular to the beam axis as a scanning mask for the expected interference pattern. Scanning the third grating across the interference pattern and counting the molecules passing will result in a sinusoidal signal variation, which is the finger print of successful molecular interference.

Our laser desorption source was tested as a new source for Talbot-Lau interferometry. The interferometer, which was used for the first laser desorption experiments is described in detail in [30, 38]. The three gratings had an identical grating period of 991.2 ± 0.25 nm, etched in a 500 nm thick gold foil by Heidenhain (Germany) with an opening fraction of 0.48. The distances between the gratings was 38.5 cm.

Before the laser desorption source was attached to the interferometer the

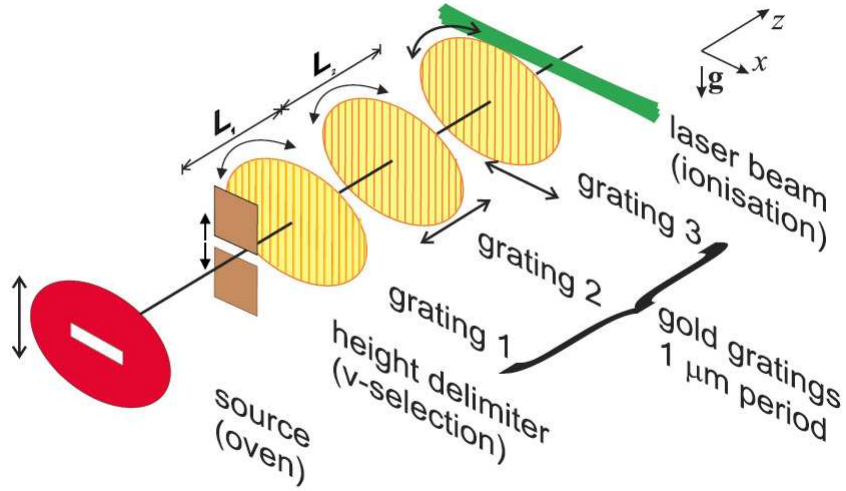


Figure 3.1: Setup of the Talbot-Lau interferometer with the 991 nm gold gratings and a grating distance of 38.5 cm [from [54]].

gratings were aligned with C_{70} emitted from a thermal source. The interference properties for fullerenes are well known [30] and the setup was aligned to maximize the fringe contrast. An oven was heated to 650°C and had a $200\ \mu\text{m}$ slit orifice. The ionization of the fullerenes was done with a 10 W laser at 532 nm (Coherent Verdi), which was focused by a 50 mm lens. The ionized fullerenes are accelerated with electric fields onto a channeltron detector. The velocity selection was done by gravitationally selecting different flight parabola. Any parabola is defined by three points, here by the oven slit, a $200\ \mu\text{m}$ slit in front of the first grating and the ionization laser with $10\ \mu\text{m}$ beam waist. Figure 3.2 shows the interference pattern after optimizing the grating alignment. The interference pattern has a visibility of 32%, which is only slightly smaller than the expected theoretical value of about 35% for the chosen setup.

After the alignment with the fullerenes the laser desorption source was attached and the channeltron was replaced by the TOF-MS with the VUV laser as the ionization source as shown in figure 2.18. The first search for interference with laser desorbed molecules was dedicated to tryptophan. It turned out that bigger junk molecules produced by the laser desorption source spoil the gratings. In order to protect the gratings from molecular debris a micromechanical filter (Gilder grid, HS2000) with $7.4\ \mu\text{m}$ sized openings was inserted into the molecular beam.

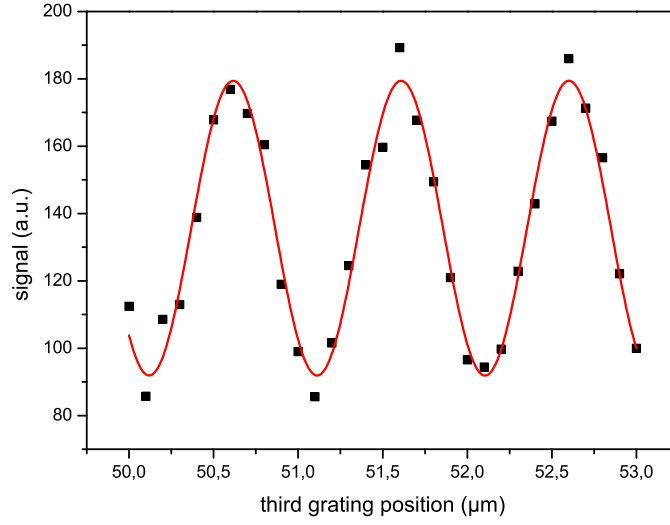


Figure 3.2: Interference pattern of C_{70} recorded in a Talbot-Lau setup. The graph shows the number of molecules as a function of the third grating position. The solid line is a fit to the data and results in a visibility of 32%.

By reducing the grating distance to about 18 cm the total length of the interferometer could be shortened from 2.5 m to 1.7 m. The Talbot length can be reduced if the grating period is adapted according to eq. 3. Instead of the previous gratings ($g=990$ nm) smaller gratings produced by Tim Savas at the Massachusetts Institute of Technology [144] were used. The grating constant was measured by the company Ibson Photonics to be 254.53 ± 0.02 nm with an opening fraction of about 40% for the first and third grating and about 60% for the second grating.

The grating distance was chosen after simulation of the expected visibility [145, 146]. In figure 3.3 the expected visibility is shown as a function of the velocity for tryptophan and the smoothed velocity distribution of tryptophan (taken from figure 2.20) is plotted in red. Within the velocity range of tryptophan the interference peak at 800 m/s is predicted to appear with a maximal visibility of 45%. In figure 3.4 the simulated visibility curves for β -carotene and gramicidin are also shown. The fringes broaden with increasing mass, but they should still allow to observe interference within the range of the available velocity distributions.

The drawback of the smaller grating period is that the pre-alignment of the gratings can no longer be performed with visible light, since the wavelength is smaller than the mask opening. Visible light may still shine through

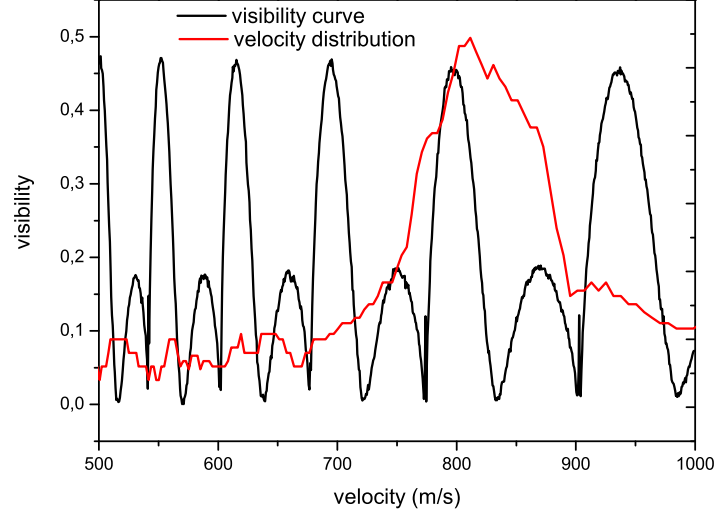


Figure 3.3: The visibility as a function of the tryptophan velocity (black) and the smoothed velocity distribution from figure 2.20 for tryptophan measured with the chopper and the closed mixing channel (red).

the 160 nm thick grating membrane, which allows aligning of the pitch, yaw and gear angle. A green laser diode beam was first aligned to gravity and then directed onto the gratings as shown in figure 3.5 top. Each grating was pitched, geared and yawed so that the backreflection of each individual grating returned along the 10 m long light path into a pinhole. This procedure assured that all three gratings were aligned with respect to gravity. The Littrow reflection was used to align the slits of all gratings parallel to each other. If light hits a grating with a period d under a specific angle Θ_L (Littrow angle) the first diffraction order is reflected back into the incoming beam (see figure 3.6). The Littrow angle is given by:

$$\sin \Theta_L = \frac{d}{2\lambda} \quad (3.1)$$

For the Littrow alignment a 405 nm laser diode again with a beam path of 10 m was used. The rolling of each grating and the incident angle on the grating were aligned in such a way that the Littrow reflex travels back the whole beam path into a pinhole as shown in figure 3.5 (bottom). This procedure assured that all three gratings are aligned parallel to each other. Due to the long beam paths an alignment precision of about $200 \mu\text{rad}$ was achieved, which is sufficient for the chosen interferometer geometry. A possible rolling mismatch of the gratings with respect to each other would result in two

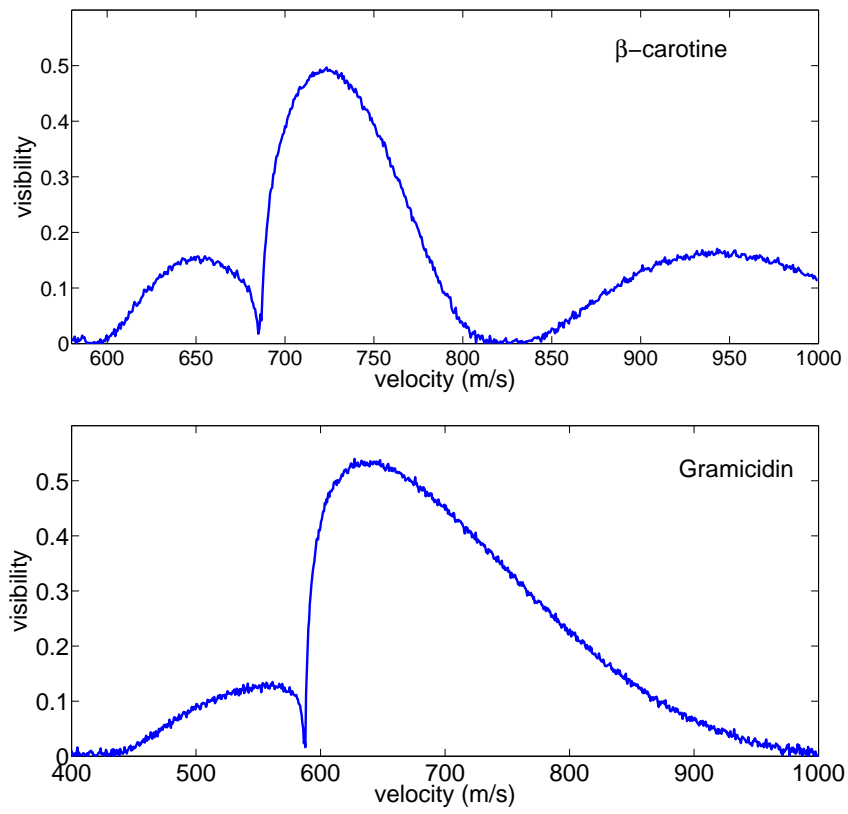
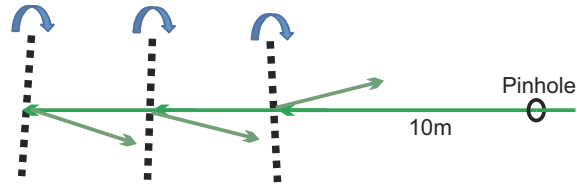


Figure 3.4: Visibility simulations for β -carotene and gramicidin in dependence of their velocity.

Pitch, gear and yaw alignment



Littrow alignment

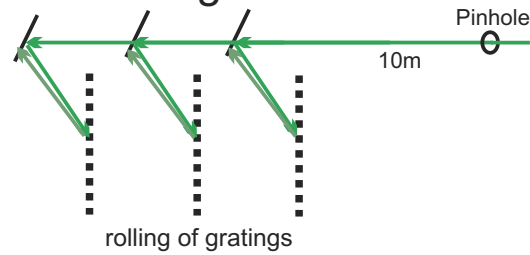


Figure 3.5: Schematic drawing of the grating alignment. Top: For pitch, gear and yaw the gratings are tilted until the backreflex travels back the incident light path. Bottom: A light beam hits the gratings under the Littrow angle. Each grating is rolled until the backreflex travels back to the beam source.

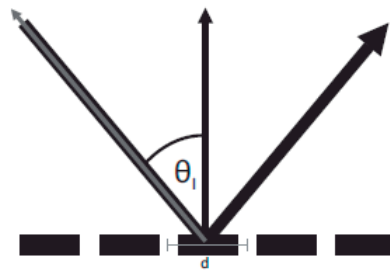


Figure 3.6: The first order diffraction is reflected back into the incident beam, if the grating is illuminated under the Littrow angle Θ_L . Picture taken from [147].

main effects [148]. First the effective grating period is changed and second molecules passing the grating at different heights experience different phase shifts.

For the distance between the three gratings a laser displacement sensor (Keyence) was used. Its longitudinal measurement accuracy is estimated to be about $50\text{ }\mu\text{m}$, which is still within the required precision ΔL for the grating distances L [148]:

$$\frac{\Delta L}{L} < \frac{1}{N} \quad (3.2)$$

where N is the number of illuminated grating slits, which is about 4,000 in our case.

After the alignment procedure was completed and the gratings were mounted in the vacuum chamber the setup was tested again with fullerenes. A change of the delimitation slits made it necessary to open the chamber and the inspection of the gratings showed that the second and third gratings had large holes. Since the first grating had no damage at all the notion that the molecular beam destroyed the gratings can be excluded. The cause of this damage was probably that the alignment laser (532nm, 50 mW), which was shining from the back of the chamber to the source in order to align the setup, burnt the holes into the gratings. The same laser was also used for the pitch, gear and yaw alignment of the three gratings, but since in vacuum there is no heat conduction by the surrounding air, the grating may have melted due to absorption and overheating.

3.1.1 Outlook and application for interferometry

After the throwback due to the damage of the gratings it is necessary to build a new interferometer for biomolecule interference. During this thesis a new possibility came up to build an all optical interferometer, where all three gratings will be replaced by standing light waves. Using three VUV lasers will allow the construction of a pulsed all optical interferometer with 80 nm grating period. Due to this small grating constant the length of the interferometer can be further reduced thereby allowing for less intense beams. The light gratings also have the advantage that the gratings can not be damaged and that the deposition of molecules on the gratings is avoided. These were the two main reasons, why interference of laser desorbed molecules could not yet be presented in this work. The first and the third light grating need to be absorptive gratings, which can be realized by ionizing gratings, which

'burn' holes in the molecular beam. The molecules passing the antinodes of the standing light wave are ionized and deflected by electric fields, such that only the neutral molecules passing through the nodes are available for further analysis. For the diffraction at the second grating a phase grating can be used as in the case of a Kapitza-Dirac-Talbot-Lau interferometer [32, 39, 42], which would also be an alternative interferometer type for biomolecule interference since the visibility reduction due to van-der-Waals interaction is avoided.

An additional advantage of an all-optical interferometer is its ability to measure the scalar optical polarizability of the molecules at the laser wavelength. The interaction of the molecules with the standing light wave depends on the dipole force and is therefore related to the polarizability [39, 42].

The scalar polarizability α of molecules can be measured by the introduction of an electric field gradient next to the second grating. The force on the molecules will lead to a phase shift Δs_x of the interference pattern, which is proportional to the force field $\mathbf{F} = \alpha(\mathbf{E}\nabla)\mathbf{E}$ [38, 40]:

$$\Delta s_x \propto \alpha \frac{(\mathbf{E}\nabla)\mathbf{E}}{mv^2} \quad (3.3)$$

where m is the mass and v the velocity of the molecules. Measuring the phase shift Δs_x for an applied electric field allows the calculation of the polarizability α . In principle this interferometric method can also be used to spatially separate molecules with different polarizabilities as proposed in [149].

Metrology experiments will be the next step as soon as the interference with biomolecules is demonstrated. For this application a laser desorption source has two advantages compared to thermal sources. First, the cold beams contain less conformers, which affect the metrology measurements due to their different polarizabilities. And second the precision of the polarizability is crucially dependent on the selected velocity width, since the velocity enters in eq. 3.3. The width of the selected velocity is in the range of one-tenth of a percent in the case of pulsed laser-desorption and photo-ionization and therefore the accuracy of α can be increased in contrast to thermal beams, where the velocity selection is only in the order of typically more than ten percent.

Chapter 4

Gas-phase formation of large organic clusters and organo-metallic complexes

The formation of large biomolecular complexes with the described laser desorption source was found due to some lucky coincidences, which are definitely an important ingredient for scientific progress. Since the desorption of tryptophan and gramicidin worked, we tried to desorb powder from a commercially available protein shake, hoping to get a cheap source for protein samples. Looking at the mass spectra of this shake was disappointing, since no clear mass peak above 200 amu was visible. We mixed tryptophan into the sample in order to check if the whole setup was working as expected. Desorption of the mixture led to a broad cluster distribution up to masses of a few thousand mass units. The distance between two clusters was the mass of tryptophan, but every peak was shifted by 40 amu towards higher mass. A look at the periodic table of the elements solved the riddle. The element calcium has a mass of 40 amu and was also an ingredient of the protein shake. The explanation for the cluster was found by recognizing that each tryptophan cluster had one calcium atom attached. In this case the protein shake did not enlarge our muscle mass, but our mass spectra!

Several studies had already been done before on the cluster formation of amino acids during laser desorption. For neutral biomolecules the production of tryptophan clusters up to a tetramer as well as the formation of gramicidin clusters was observed [120]. The largest gramicidin cluster was an octomer, which corresponds to a mass of 15.040 amu. And additionally

the attachment of methanol and water molecules to the tryptophan monomer and dimer was shown. Clustering of neutral tryptophan up to a hexamer as well as the attachment of benzene and water molecules to a single tryptophan molecule could be demonstrated [150]. Also the formation of dimers with all possible combinations of the amino acids tryptophan, tyrosine and glycine and clustering of each of the amino acids with retinol was observed.

Many studies on gas-phase clusters so far have been performed on charged complexes using *electro spray ionization* (ESI) [151,152]. In ESI the dissolved molecules are sprayed from a capillary with an electric field at its tip. They leave the ESI source already as ions and further post-ionization is not needed. A detailed examination of the clustering ability of all amino acids was performed in [153] using an ESI source. The formation of mixed complexes between biomolecules and metal atoms was studied for tryptophan-silver clusters [154]. Up to three silver atoms were attached to a single tryptophan molecule, which resulted in a significantly higher absorption compared with pure tryptophan. This showed that the molecular environment strongly influences the electronic properties. Electro spray ionization was also used to study the clustering and appearance of magic numbers of nucleobase-alkali clusters [155] as well as to examine the formation and stabilization of nucleotide quartets by alkali atoms [156], which may give some insight into the complex field of DNA research. Nanometer scaled compact clusters of serine with masses of up to 3,000 amu consisting of 600 serine blocks [157] were studied by the use of ESI. This studies showed a strong chiral preference in the cluster formation and led also to the production of serine-sodium clusters and the incorporation of amino acids into the serine complexes [158]. Infrared spectroscopy on silver, lithium, sodium and potassium attached to a single tryptophan after ESI was used to confirm density functional theory (DFT) calculations of the binding in those species [159].

The motivation for the study of cluster formation is manifold, since many interesting effects can be studied:

- The properties of the cluster may change compared to the single building blocks.
- The formation of magic⁵ clusters can give insight into the formation process.

⁵A cluster peak is called *magic*, if it shows a high stability/abundance relative to its neighboring peaks.

- Cluster formation is used to study preferences in the chirality of various species.
- The study of organic-complex formation is especially interesting, since for example self-organization is important in living organisms.

4.1 Formation of amino acid clusters

4.1.1 Alkaline earth metal inclusion into tryptophan clusters

Our laser desorption source is not only able to bring thermally labile molecules into the gas-phase, but it even allows us to produce big clusters and organic complexes up to 7,000 amu [122,123]. The setup for our cluster experiments is shown in figure 2.1. If not mentioned otherwise we used the closed mixing channel shown in figure 2.8.

The first clusters studied in our experiments were tryptophan-calcium cluster [122]. In order to create these organo-metallic complexes the tryptophan samples were mixed with calcium-carbonate CaCO_3 and cellulose in a weight ratio of 1:5:5 (CaCO_3 :tryptophan:cellulose). All tryptophan-calcium

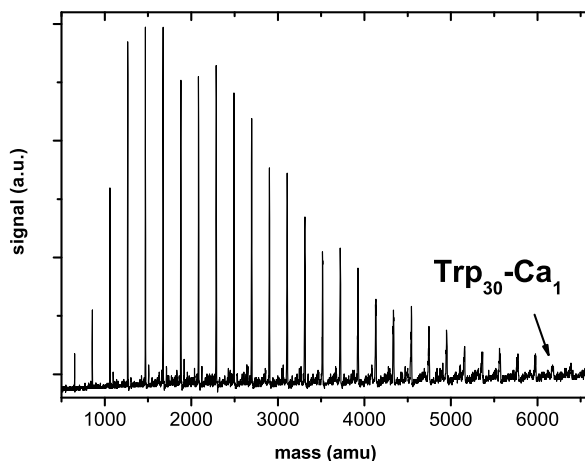


Figure 4.1: Mass spectrum of tryptophan-calcium clusters. All clusters contain a single calcium atom and the largest clusters contain more than 30 tryptophan molecules. Seed gas: Argon 2 bar; Desorption: 12 mJ (355 nm); Ionization: 3 mJ (157 nm) [122].

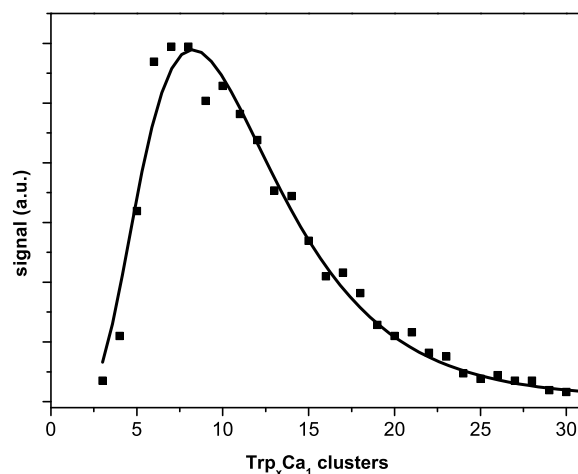


Figure 4.2: The experimental data from figure 4.1 plotted as a cluster distribution of Trp_xCa_1 . The data points are well fitted by a log-normal distribution (solid line) [123].

clusters shown in figure 4.1 are found to be of the form Trp_nCa_1 . The largest observed organo-metallic cluster had a mass of 6,779 amu and contained 33 tryptophan molecules ($n=33$). If the intensities of the cluster peaks are printed as a function of the number of tryptophan molecules as in figure 4.2 one can see that the most intense clusters have about ten tryptophan molecules included. The cluster distribution is well fitted by a log-normal distribution [160]. This indicates that the cluster formation is a product of a series of independent random processes. All clusters are neutral and can only be seen after the post-ionization. We assume that the doubly positive calcium ion is neutralized by negative charges located on two neighboring tryptophan molecules. This results in a neutral TRP-TRP-Ca core, where additional neutral tryptophan molecules can attach.

After our first discovery of large tryptophan-metal clusters further experiments showed that also pure tryptophan clusters can be produced under favorable circumstances. Figure 4.3 shows a mass spectrum of pure tryptophan desorbed from a sample containing a mixture of CaCO_3 :trp:cellulose (0.2:1:1.2).

Preferentially only the clusters with one embedded calcium atom were visible in the mass spectrum. But occasionally also the pure tryptophan were observed and very rarely both species were present at the same time. The desorption of pure tryptophan powder without the calciumcarbonate

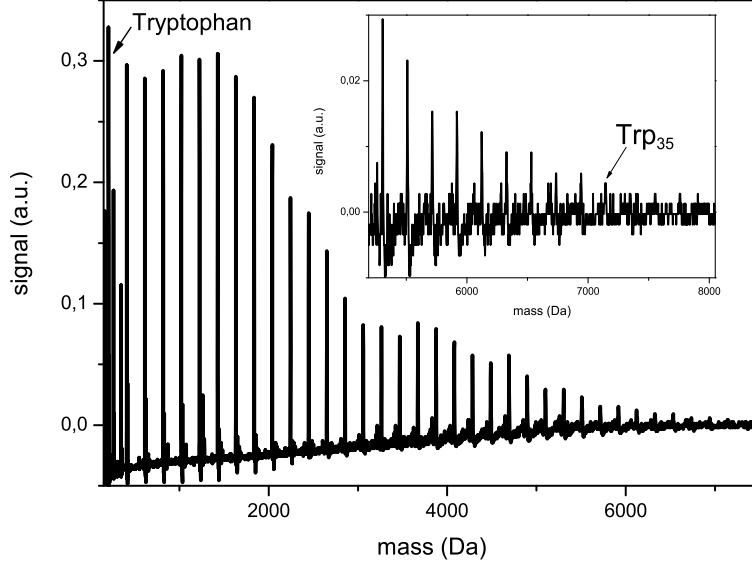


Figure 4.3: Mass spectrum of pure tryptophan clusters. The inset shows the enlarged tail of the cluster distribution where a Trp_{35} cluster with a mass of 7140 amu is still visible. Seed gas: Helium 2 bar; Desorption: 10 mJ (355 nm); Ionization: 1 mJ (157 nm).

in the sample never resulted in cluster bigger than a trimer. We therefore conclude that calcium plays an important role in the formation even of the pure clusters. The reason for that is not yet understood, since neither the channel temperature nor the desorption energy nor the ionization energy significantly influenced the ratio of calcium loaded and pure tryptophan clusters. We propose two different hypotheses to explain the observation of the pure tryptophan clusters: First, since the incorporation of silver atoms into tryptophan showed an enhancement of the absorption cross section [154], a similar effect may also be expected for calcium. In analogy to that one might speculate that the photon absorption during post-ionization may preferentially occur at the site of the TRP-TRP-Ca complex. Thus, the detachment of the TRP-TRP-Ca complex or the single calcium atom may occur during the photo-ionization process. Since these fragments are not present in the mass spectra, they would have to be separated from the cluster as neutral or negatively charged species. A second explanation for the pure clusters may be that the metal-tryptophan clusters fragment soon after their formation. This can be the case, whenever their internal energy exceeds a certain threshold, i.e. if the carrier gas is not able to cool the cluster below a certain

value. If during such a fragmentation process the TRP-TRP-Ca complex ionizes, it will not reach the mass spectrometer and only the neutral pure tryptophan cluster will be post-ionized.

For a better understanding of the cluster formation computational simulations were performed by Prof. Dr. Christoph Dellago and Dr. Harald Oberhofer (Computational Physics, Faculty of Physics, University of Vienna) for various sizes of both pure Trp_n and Trp_nCa_1 clusters in an equilibrium molecular dynamics simulation [122]. For the simulations the NAMD [161] package with the CHARMM 2.7 [162, 163] force field was used. The thermalizing effect of the seed gas was taken into account by assuming that a noisy environment of a given temperature is coupled to the system and acts as a thermostat. The clusters are modeled as consisting of a single Ca^{2+} ion, two tryptophan ions and a varying number of neutral tryptophan molecules.

The first step in the simulation starts with a thermalization of both the pure and the calcium containing clusters for 1 ns at 300 K. The time evolution of the clusters is then followed for 9 ns. The calculations were carried out for individual clusters and do neither describe their formation nor their growth, which will probably happen on much larger time scales. In figure 4.4 snapshots of the simulations are shown for the pure and the metal containing clusters. The last step of the simulations was to calculate the equilibrium average radii of gyration and the binding energies, which are shown in figure 4.5 for different cluster sizes. The radii of gyration for the clusters with and without calcium are roughly the same for all cluster sizes confirming the visual impression that the shapes and sizes of pure and metal containing clusters do not differ significantly. The binding energy is defined as the energy necessary to detach a single tryptophan molecule and move it towards infinity. In order to determine the binding energies the average potential energy for all cluster sizes n was computed and in the case of the metal containing cluster $n - 2$ times the average energy of a single uncharged tryptophan and twice the average energy of a charged tryptophan was subtracted. For the pure clusters simply n times the potential energy of an uncharged tryptophan was subtracted.

The simulations show a higher stability for the calcium containing clusters compared to the pure ones. Most of the increased binding energy is due to the two charged tryptophan molecules binding to the calcium ion, which lowers the binding energy by about 100 kcal/mol. Adding more tryptophan molecules beyond the first two leads to nearly the same energy loss of about

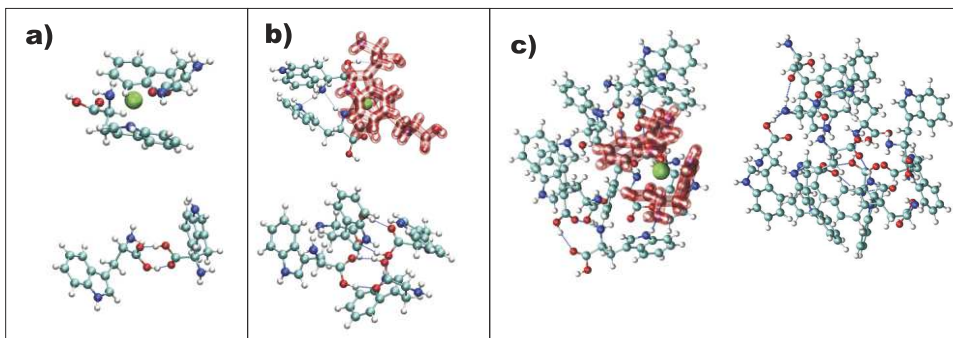


Figure 4.4: Snapshots from molecular dynamics simulations of tryptophan_n clusters with and without calcium for $n = 2$ (a), $n = 4$ (b) and $n = 10$ (c). The calcium atom is depicted as a green large sphere and the two charged tryptophan molecules are highlighted in red. Note that the charged tryptophans are bound rather tightly to the metal by electrostatic forces, while the rest of the cluster is mainly stabilized by hydrogen bonds (dashed blue lines) and van der Waals interactions [122].

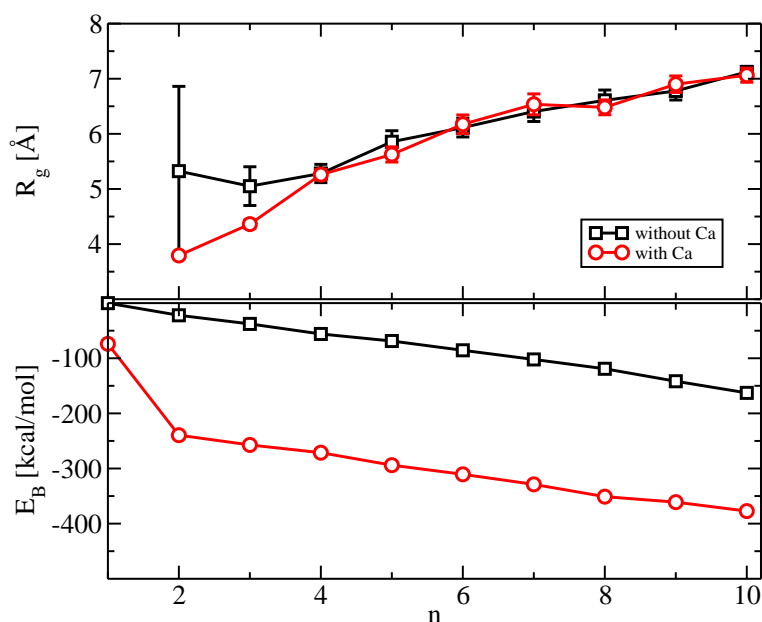


Figure 4.5: Radii of gyration (top) and binding energies (bottom) for Trp_nCa₁ complexes as a function of the number of tryptophan molecules [122].

10 kcal/mol for both cluster types, i.e. with and without a metal atom. This can be seen from the identical slopes in figure 4.5.

The experimental data from figure 4.1 shows that the incorporation of more than one calcium atom is negligible, which means that the tryptophan molecules must agglomerate one by one around the Trp_2Ca_1 nucleation core and no agglomeration of preformed Trp_2Ca_1 cores occurs. A speculative explanation is based on the prevalence of polarization effects around the neutral Trp_2Ca_1 core, which actually possesses a strong charge asymmetry. This could tend to orient the surrounding amino acid's dipoles and lead to further agglomeration. Our simulations are, however, based on the assumption of a system in equilibrium, which is probably not reached in the rapid transition through the nozzle channel.

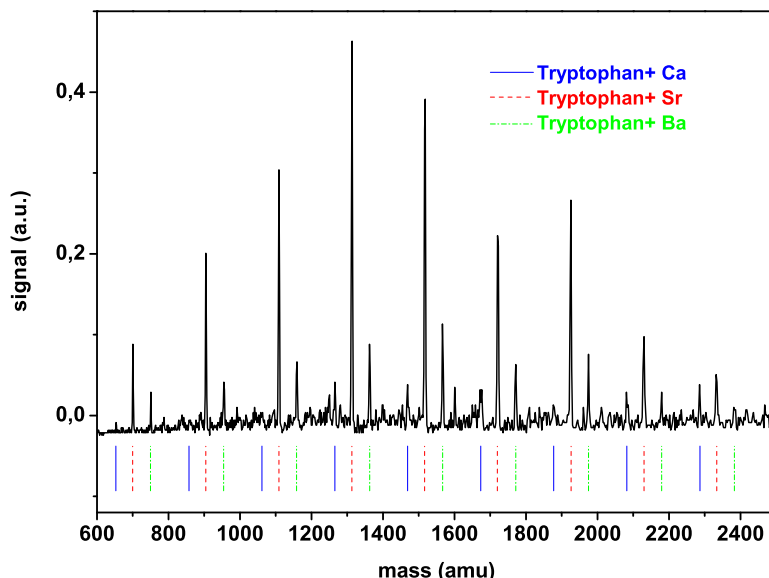


Figure 4.6: Comparison of the tryptophan metal clusters after the desorption of tryptophan and three different alkaline earth metal salts (CaCO_3 , SrCO_3 , BaCO_3) in equal number concentrations. The colored lines mark the three different tryptophan clusters, which contain one of the three metals. The clusters with embedded strontium result in the highest yield. Seed gas: Argon 2 bar; Desorption: 12 mJ (355 nm); Ionization: 1 mJ (157 nm) [122].

In order to understand the particular role of the embedded metal atom other alkaline earth metals were also co-desorbed with tryptophan as they should have a similar configuration of the outer electronic shell. Experiments

performed with strontium and barium showed that these metals also form clusters with tryptophan. By desorbing a sample containing all three metals in a weight ratio of 1:1.5:2 (CaCO_3 : SrCO_3 : BaCO_3) it was investigated if tryptophan preferentially binds to one of the three metals. At this weight ratio the sample contained the same number of atoms for all three metals. In figure 4.6 the mass spectrum of the desorbed metal-mixture, tryptophan and cellulose (weight ratio 2.8:8:5) is shown. The most intense peaks in figure 4.6 are the strontium-tryptophan clusters followed by the ones with barium and calcium. This might be related to the carbonate dissociation efficiency, which could lead to a higher number of, for example, free strontium atoms compared to calcium or barium.

The formation of these large bioclusters allowed to check a possible velocity slip over a large mass range. Analyzing the velocities from small clusters like Trp_2Ca_1 (448 amu) to $\text{Trp}_{11}\text{Ca}_1$ (2284 amu) resulted in a velocity reduction of about 5% for both helium and argon as seed gas. For larger clusters the fluctuating shape of the velocity distribution does not allow to fit the fluctuating velocity distribution anymore.

4.1.2 Formation of sodium and copper tryptophan clusters

In the following section we discuss metal-organic cluster formation in the presence of sodium and copper.

A mass spectrum of a sample containing Na_2CO_3 , tryptophan and cellulose (mixture: 0.3:1:1.6) is shown in figure 4.7. In contrast to calcium, where only one calcium atom was included per tryptophan, co-desorption of sodium allows the incorporation of several metal atoms per tryptophan. The cluster distribution can be described by the form $\text{Trp}_n\text{Na}_1 \dots \text{Trp}_n\text{Na}_{n+1}$ at least up to Trp_5Na_6 in figure 4.7. This rule is underlined by the experimental fact that in the given mass range no limitation is given due to a limited resolution of the setup. For the low mass clusters an additional sodium atom would not be lost in the noise, but its absence is a clear sign that the cluster is unable to include an additional atom. The conclusion drawn from these observations is that the maximally number of embedded sodium atoms is limited. This may be due to the nature of the molecular bonds of the clusters. Further numerical modeling would be needed for a better understanding of this behavior. Additional experimental information such as dipole moments and polarizabi-

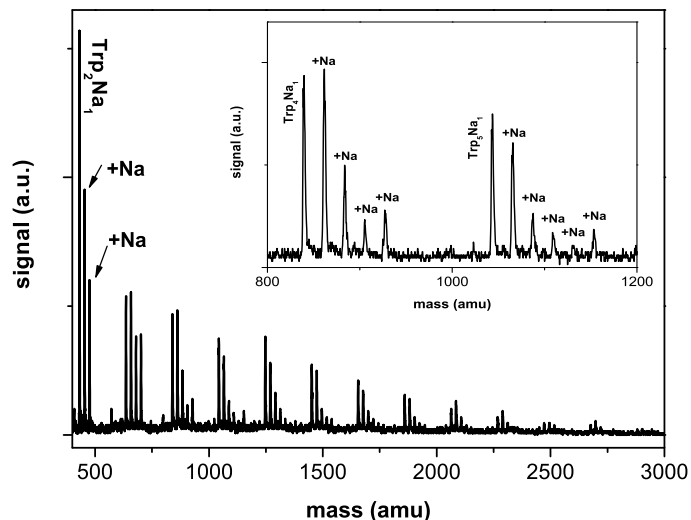


Figure 4.7: Mass spectrum of sodium tryptophan clusters. In contrast to calcium, several sodium atoms can be included into the tryptophan clusters. The inset shows a blown up picture of the Trp_4Na_k and Trp_5Na_k cluster, where the later has six sodium atoms included. Seed gas: Neon 2bar; Desorption: 10 mJ (355 nm); Ionization: 2.5 mJ (157 nm) [123].

lities can be obtained in future metrology experiments in combination with interferometry.

Even the desorption of copper together with tryptophan resulted in the formation of clusters. Desorption of a mixture of CuCO_3 , tryptophan and cellulose led to tryptophan-copper clusters as shown in figure 4.8. The cluster formation starts with Trp_4Cu_1 and every Trp_xCu_n cluster can contain one or two copper atoms ($n=1$ or 2). Except for the first cluster Trp_4Cu_1 the signal for Trp_xCu_1 is always stronger than the yield for Trp_xCu_2 .

4.1.3 Formation of phenylalanine calcium clusters

After the first observation of tryptophan-metal clusters it was of interest how the clustering process would change when tryptophan is replaced by another amino acid. For this comparison phenylalanine (165 amu) was chosen as a substitute for tryptophan. In figure 4.9 the mass spectrum of desorbed phenylalanine mixed with calcium carbonate and cellulose (ratio: 1:1:1) is shown. The phenylalanine complexes contain preferentially one and, less frequently, two calcium atoms. The maximal mass of the phenylalanine clusters is about

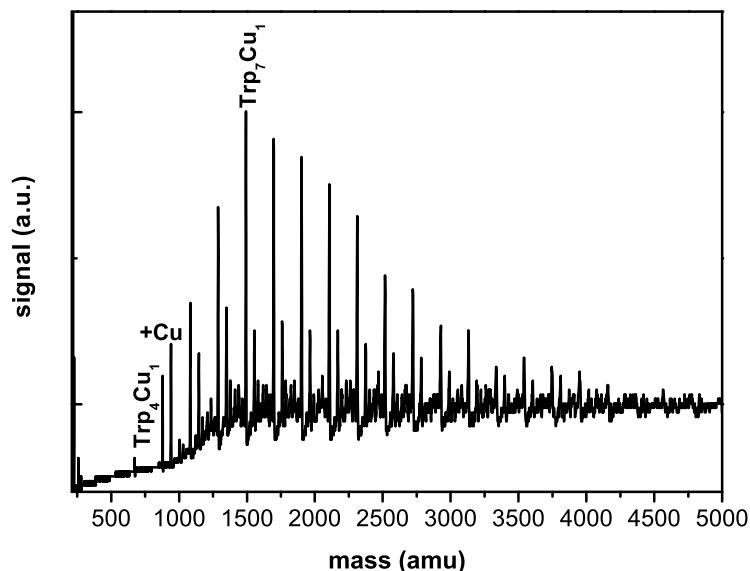


Figure 4.8: Desorption of copper carbonate together with tryptophan leads to the formation of Trp_xCu_n clusters with $n=1,2$. Seed gas: Argon 2 bar; Desorption: 9 mJ (355 nm); Ionization 2.6 mJ (157 nm) [123].

1500 amu. The Phe_5Ca_1 cluster always shows a relative high ion yield compared to its neighboring peaks, which could be the indication for a magic cluster.

4.2 Pure clusters of biomolecules

In our quest for massive neutral organic clusters that can still be photoionized, we also explored a number of additional biomolecules [123]. We observed for example the cluster formation of the tripeptide H-D-Tyr-Trp-Gly-OH (425 amu, Bachem Inc.). It was desorbed from a highly diluted mixture together with calcium carbonate and cellulose (1:40:10-Tripeptide: CaCO_3 :cellulose). The resulting mass distribution after post-ionization is shown in figure 4.10. The tripeptide forms pure clusters up to $(\text{H-D-Tyr-Trp-Gly-OH})_{13}$ with a mass of 5,525 amu and interestingly the tripeptide remained pure, i.e. no calcium is embedded into the clusters despite the enormous relative abundance of calcium in the sample.

All cluster experiments described so far used amino acids. But massive clusters were also observed with nucleotides like guanine (151 amu). Fi-

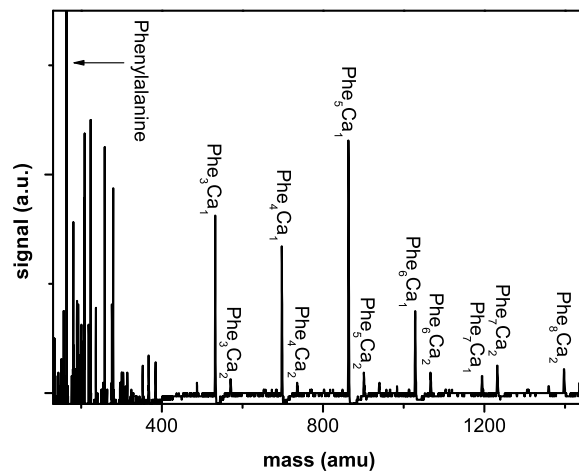


Figure 4.9: Mass spectrum of phenylalanine calcium cluster. Up to two calcium atoms are incorporated in the clusters. Seed gas: Argon 2 bar; Desorption: 10 mJ (355 nm); Ionization: 10 mJ (266 nm) [123].

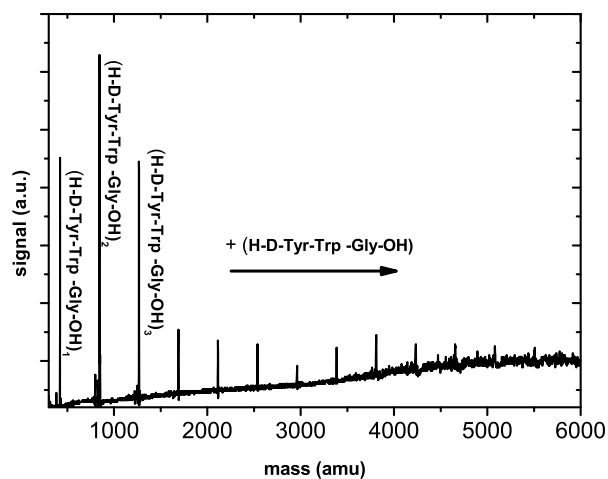


Figure 4.10: Mass distribution of the desorbed tripeptide H-D-Tyr-Trp-Gly-OH with up to thirteen molecules bound together reaching a mass of 5525 amu. No inclusion of calcium atoms was observed for this species. Seed Gas: Argon 2 bar; Desorption: 7 mJ (355 nm); Ionization: 2.8 mJ (157 nm) [123].

Figure 4.11 shows the mass spectrum after desorption of a sample of guanine, calcium carbonate and cellulose (mixture: 1:1:0.7). As depicted in Figure 4.11, guanine forms clusters without embedding even a single calcium atom. The total intensity of all guanine clusters varies from shot to shot, but the guanine pentamer always stands out as a particularly abundant 'magic' cluster. It is still an open question if this phenomenon is related to the particular stability of guanine₅.

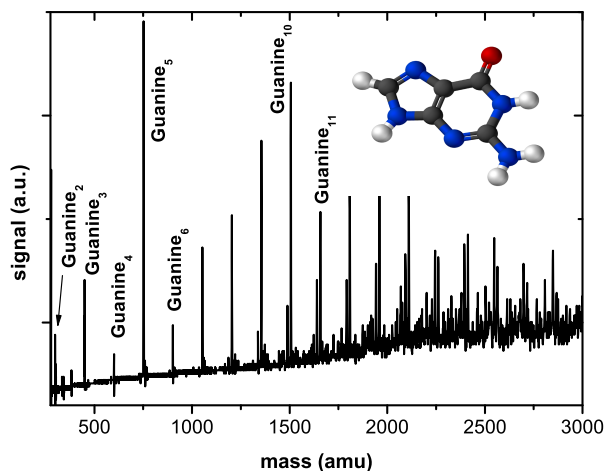


Figure 4.11: Mass spectrum of guanine clusters. The figure also shows that guanine₅ stands out as a 'magic' cluster and that calcium atoms though present in the sample are not embedded into the clusters. The inset shows the structure of the guanine molecule. Seed gas: Argon 2 bar; Desorption: 12 mJ (355 nm); Ionization: 0.5 mJ (157 nm) [123].

As shown so far our source can produce large neutral clusters of biomolecules with a mass of several kDa containing more than thirty molecules. But the heaviest cluster ever seen in the presented source contains only four molecules, i.e. a tetramer. This tetramer formed with gramicidin molecules, but since the mass of the gramicidin A is already 1,884 amu the observed tetramer sums to 7,536 amu. Figure 4.12 shows the mass spectrum of the gramicidin A monomer, dimer, trimer and tetramer, desorbed from a gramicidin D and cellulose sample mixed 1:1 in the open 4 mm mixing channel.

Another interesting feature, which was observed, is the clustering between different molecular species. The experiments were performed with the closed mixing channel, where gramicidin D, tryptophan, insulin and cellulose in a mixture of 0.8:1:1.2:1.6 were co-desorbed from the sample. Clustering could

be observed, but in a completely new form. Insulin was not visible neither pure nor in clusters. Interestingly, however, tryptophan clustered with gramicidin. Figure 4.13 shows a mass spectrum, where up to nine tryptophan molecules are attached to a single gramicidin A molecule.

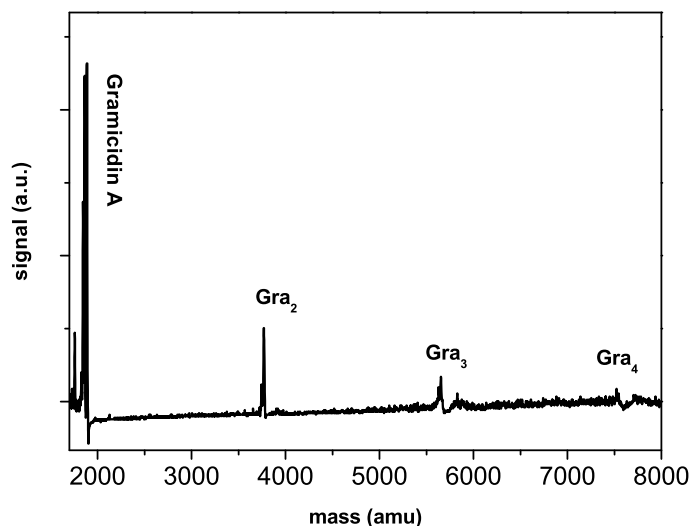


Figure 4.12: Gramicidin A forms clusters after desorption, where the largest one is a tetramer with 7536 amu. This spectrum was recorded with the 4 mm open mixing channel. Seed gas: Argon 2 bar; Desorption: 6 mJ (355 nm); Ionization: 1 mJ (157 nm) [123].

Outlook for bioclusters

Details about the internal properties of the presented clusters are not yet available since this requires additional methods to mass spectrometry. Therefore the clusters are interesting candidates for molecular interference experiments. The high mass will allow future interference experiments to extend the mass limit of biomolecules to several thousand atomic mass units by retaining photo-ionization as detection method, which generally fails in that regime. The combination of near field matter wave interference with metrology will allow the measurements of cluster polarizabilities, dipole moments or to spatially separate species with different values. Results obtained in these experiments hopefully stimulate computational simulations to better understand the binding and structure of the different clusters. Interesting open questions are the predominance of some magic clusters, the varying

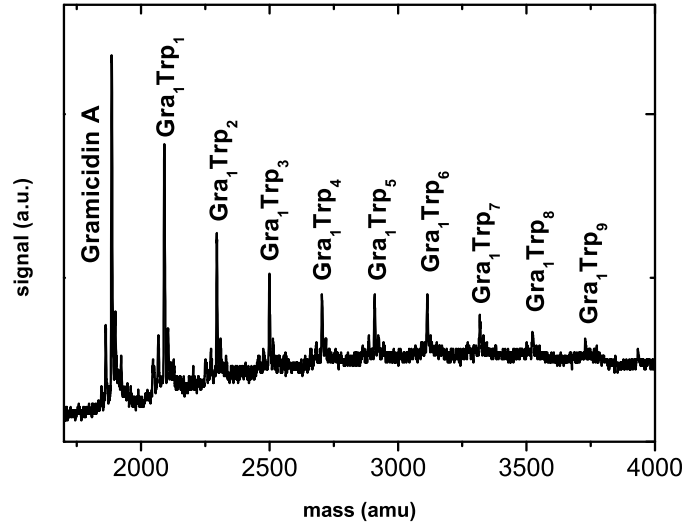


Figure 4.13: Desorption of a tryptophan and gramicidin mixture results in mixed clusters. Up to nine tryptophan amino acids are bonded to a single gramicidin A polypeptide. Seed gas: Helium 2bar; Desorption: 11.5 mJ (355 nm); Ionization: 2.5 mJ (157 nm) [123].

number of the embedded metal atoms for different metal species and the influence of the used metal atoms on the metal-tryptophan cluster yield.

Chapter 5

A superconducting detector for neutral molecules

The experiments presented in this chapter were done in collaboration with Prof. Dr. Gregory Gol'tsman's group from the Moscow State Pedagogical University. Special thanks go to Alexander Divochiy and Dr. Alexander Korneev, who came to Vienna to perform the experiment with us. The results of this chapter are published in [164].

5.1 Introduction to superconducting detectors

Detectors that are sensitive to the incident energy are important tools for the detection of radiation and particles. A very simple detector is for example a *bolometer*, which transforms the incident energy of radiation or particles into a temperature change of the device. The sensitivity of such a bolometer is limited by the ability to detect small changes of ΔT , which can be measured for example by a change in the resistivity. Bolometers, which convert energy to an electric signal were first used for the detection of infrared radiation [165], but were soon also used as particle detectors [166–168]. A germanium bolometer was used to detect beams of neutral helium and argon beams exceeding the threshold of 10^7 molecules/sec for a detector size of 1 mm^2 [167].

Highly sensitive bolometers were developed using superconducting materials, where small temperature changes result in large resistivity changes. This is due to the fact that the resistance of a superconductor drops to zero

at a certain critical temperature called T_c . In principle a superconducting bolometer can be realized by cooling the device slightly below T_c and exposing it to radiation or particles. If the accumulated energy is high enough to heat the superconductor locally above T_c this results in a measurable voltage peak. The first superconducting bolometers were developed as detectors for infrared radiation [169–171], but later also used as particle detectors (for reviews see [168, 172–174]).

Other types of superconducting particle detectors are *superconducting tunneling junctions* (STJ) and superconduction *transition edge detectors* (TES). Superconducting tunneling junctions are used to detect single charged ions of massive molecules in combination with time-of-flight mass spectrometry [175, 176]. In a STJ an incident particle breaks copper pairs, which leads to the tunneling of quasiparticles through an insulating barrier and consequently to a voltage peak. Superconducting tunneling junctions were implemented instead of multi channel plates, which have the drawback of a sensitivity drop with increasing mass due to the decreasing velocity [177, 178]. In [175, 176] STJs are used instead of MCPs to detect high mass ions up to 66,000 amu (bovinum albumine) and the STJ is found to have a mass independent detection efficiency of 100% [176]. Also for *transition edge detectors* the successful detection of large biomolecular ions was demonstrated [179]. A transition edge detector is a superconducting detector working exactly at the phase transition T_c , where small temperature changes result in large resistivity changes.

While both the STJ and TES detectors are only used for high energetic charged single particles, the mentioned germanium bolometer [167] for neutral particles needs a high particle flux. Here we present for the first time the successful application of a *superconducting single photon detector* (SSPD) and first evidence for its sensitivity to *neutral* and *single* particles.

5.2 Experimental setup

We tested two different types of superconducting detectors made of niobium nitride (NbN) wires for their sensitivity to neutral molecules. The first one was a *superconducting single photon detector* (SSPD) and the second one a *superconducting bolometer*.

The SSPD chips were fabricated by depositing a NbN film of 3.5–4 nm thickness on a sapphire substrate. The chips used for the experiment had

a sensitive area of either $10 \times 10 \mu\text{m}^2$ or $20 \times 20 \mu\text{m}^2$. The 100-120 nm wide NbN wire meanders on that area with a filling factor of 60%. The critical temperature of NbN is $T_c = 10\text{-}11 \text{ K}$ and the critical current density amounts to $j_c = 3.5 \times 10^6 \text{ A/cm}^2$.

The NbN film was deposited on sapphire substrates by DC reactive magnetron sputtering in an Ar and N_2 mixture. The film was patterned by direct electron beam lithography and reactive ion etching. Gold contacts were added using photolithography and wet etching. A detailed description of the fabrication process can be found in [180]. Figure 5.1 shows a SEM image of the chip, where the meandering wire is visible. For the operation of the SSPD a DC bias current slightly smaller than the critical current was applied to the nanowire by using the gold contacts.

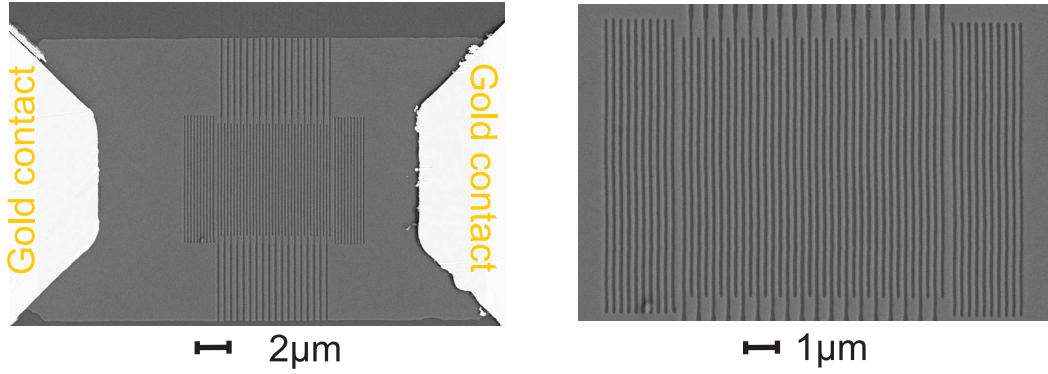


Figure 5.1: SEM images of the SSPD chip. The NbN film is shown in light gray, whereas the dark lines were etched into the film. Left: The wire is sitting between two gold pads used for contacting. Right: Detailed view of the meandering wire.

The SSPD mechanism can be understood as follows: high energy acoustic phonons are created by the impact of a molecule on the chip surface. These phonons break the cooper pairs, which are responsible for superconductivity. Thus electrons are generated, which break more and more copper pairs, i.e. an avalanche multiplication cascade is triggered. At the end of the cascade, a hot spot is formed and the superconducting current is forced to flow around the newly formed normal-conducting area as depicted in figure 5.2. Due to this fact, the current density in the areas next to the hotspot increases. If the hot spot reaches a certain size, the critical current density is exceeded. This, in turn results in a breakdown of superconductivity across the entire

width of the nanowire, followed by a voltage peak. The process of the hot spot formation and the breakdown of superconductivity was studied with photons in [181–185].

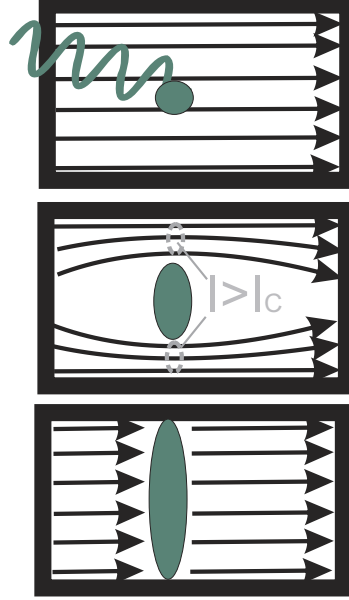


Figure 5.2: Drawing of the hot spot formation mechanism. The nanowire is biased with a current I slightly below the critical current I_c . 1) A particle hits the chip and destroys superconductivity on a small area called the hot spot. 2) The superconducting current is forced to flow in the superconducting areas around the hot spot. 3) The increasing area of the hot spot results in a break down of superconductivity over the hole chip width, as soon as the critical current density is reached. Only after the hot spot is cooled down again the chip will switch back into the superconducting state.

The second superconducting detector that we tested was a bolometer. The chips were made from the same NbN wire using photolithography and wet etching. The bolometer chips had $2\,\mu\text{m}$ broad and a few nanometer thick wires with gaps of $2\,\mu\text{m}$ meandering on an area of about $800 \times 800\,\mu\text{m}$. The bolometer, however, operates at the critical temperature T_c and it is capable of measuring small temperature changes. Therefore a resistor was installed in thermal contact with the chip to heat the superconducting wire to T_c . If a molecule impacting on the chip is able to heat the superconducting wire above T_c , it will cause a voltage peak. This mechanism presupposes that the energy of the particle is high enough to provide a temperature change above

T_c , which is very difficult to achieve with a dilute particle beam. We tested the bolometer chip as a detector in combination with the laser desorption source, but we did not find any detectable signal. Due to the insensitivity of the bolometer chips to the desorbed molecules these chips will not be discussed any further in this thesis, but instead the results of the SSPD chips will be presented in the following.

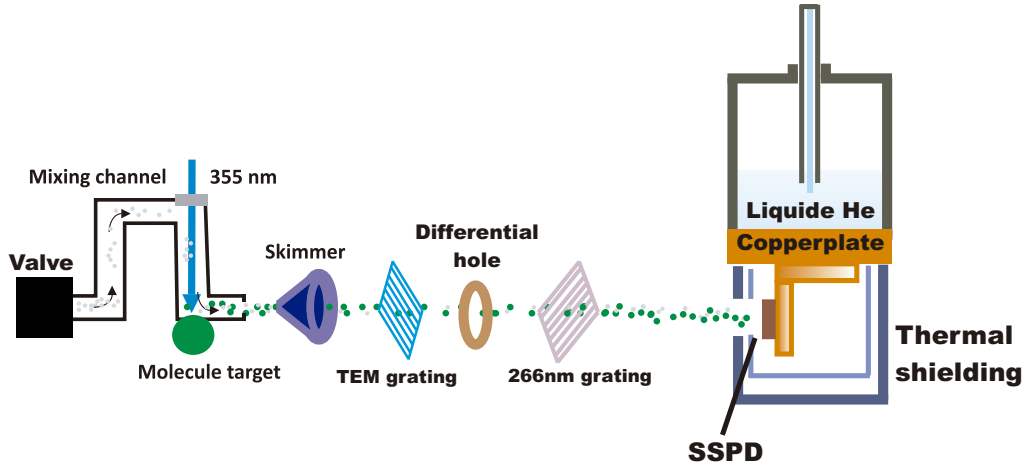


Figure 5.3: Drawing of of the SSPD setup. From left to right: Laser desorption source, skimmers, filters and cryostat with the superconducting chip.

In order to generate molecular beams, which impinge on the chip's surface the closed mixing channel as described in section 2.2 was used. The overall distance from the source exit to the superconducting chip was 76 cm. A schematic drawing of the entire setup is depicted in figure 5.3. Two centimeters after the exit of the mixing channel the molecules pass a 1 mm skimmer and enter a differential pumping stage. They traverse a copper grating with $7.5\ \mu\text{m}$ openings (Gilder grids, HS2000) to filter out possible bigger junk particles released by the source. The molecules leave the pumping stage through a 1 cm diameter hole and enter the detection chamber, where the cryostat is mounted, which houses the chip. Three thermal shields with a 1 cm diameter opening hole in the beam direction are used to decouple the chip from the environment. On the entrance of the outermost shield a silicon nitride (SiN) grating with a 266 nm period and opening slits of about 100 nm was glued in order to further limit the influence of molecular clusters and also to dilute the beam density. But even with the two filter gratings in the beamline the lifetime of the chip was limited to about 20,000 desorption shots, after which

the chip normally became insensitive to further particles. It is believed, that after this amount of shots monolayers of molecules have covered the chip resulting in the observed insensitivity to impacting particles. The detector chip was clamped onto a copper cold finger, which was in thermal contact with the copper bottom plate of the cryostat. Filling liquid helium into the bath cryostat cooled the copper parts and the chip to 4.2 K, i.e. well below T_c of the NbN wire.

5.3 First detection of neutral biomolecules with a superconducting single photon detector

Our first experiments with the SSPD detector tested its sensitivity to neutral molecules. The $20 \times 20 \mu\text{m}^2$ chip was put in the molecular beamline without any filter gratings. An oscilloscope was triggered with the Q-switch of the desorption laser and the SSPD signal was recorded for several milliseconds after the desorption pulse. The SSPD signal voltage was amplified by 20 db. The desorbed sample contained 0.2 g myoglobin (17 kDa), 0.3 g β -carotene (537 amu), 0.3 g insulin (5.7 kDa), 0.25 g bovine serum albumin (66 kDa) and 0.5 g cellulose. Figure 5.4 (left) shows a time-of-flight distribution of the molecules for a bias current of $19.5 \mu\text{A}$ applied to the chip. A high resolution picture of a typical single detection event with a width of 10 ns (FWHM) is shown in figure 5.4 (right).

Further experiments were performed to find evidence for true single molecule sensitivity. All desorption experiments in the previous chapters relied on post-ionization and ions coming directly from the source were never observed. This excludes that ions trigger the SSPD, but instead only the neutral particles are detected. The seed gas or the co-desorbed cellulose could also be excluded as causes for the detected signals. The influence of the co-expanding seed gas can be examined by leaving the valve working without desorption in order to produce a supersonic gas beam without embedded molecules. The helium seed gas beam did not result in any detectable signal. This observation indicates that the SSPD chip is not capable of detecting single helium atoms, which excludes any influence of the seed gas beam to the above shown SSPD signal. Also beams of the more massive noble gases, i.e. neon, argon, krypton and xenon did not result in signal. The absence of any detectable signal for the gas beam is in favor of the *single* molecule

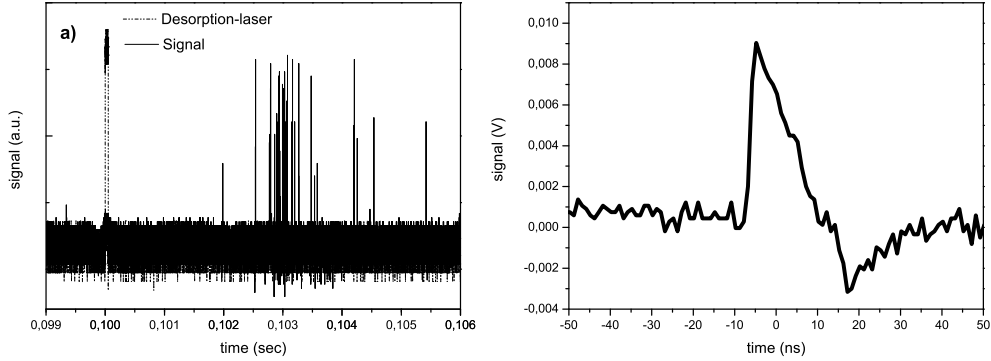


Figure 5.4: Left: Time resolved picture of the SSPD signal. The dashed line shows the Q-switch of the desorption laser, i.e. the starting point of the molecules. About 3 ms later most of the molecules arrive at the SSPD chip. Right: Single signal peak which is attributed to the impact of a neutral molecule on a $20 \times 20 \mu\text{m}^2$ SSPD chip, which was biased with $19.5 \mu\text{A}$. The amplification of the signal was 20 db [164].

sensitivity of the SSPD chip. The energy of a single gas atom is below the detection threshold and therefore the density of the helium atoms is too low for a collective triggering of the chip by simultaneous impacting atoms. Since the number of implanted molecules into the gas beam can be expected to be even more dilute than the gas beam itself, a collective effect from several molecules arriving at the same time is even less likely.

Another source for possible background signals is the cellulose, which is always admixed to the samples. To study its influence a pure cellulose sample was desorbed. Under the same experimental conditions as for samples with biomolecules the SSPD chip did not show any signal with the pure cellulose sample alone. These two observations, that neither the seed gas nor the cellulose produced any background signal indicates that the measured signals must be caused by the biomolecules impinging on the chip and are therefore the first evidence of the sensitivity to neutral complex nanoparticles of the SSPD chip.

The experiment was changed to a pulse counting mode to record time-of-flight curves of the molecules. The amplified output of the SSPD chip was fed into a discriminator, which produces a TTL pulse for every signal peak above a certain threshold. The TTL pulses are counted with a timer card for several milliseconds, which was triggered by the Q-switch of the desorption laser, i.e. the starting point for the molecules. In the following experiments the

samples contained only biomolecules of one species mixed 1:1 with cellulose. In figure 5.5 (left) the arrival time distributions for tryptophan (204 amu) and gramicidin D ($\approx 1,900$ amu) are shown. For the heavier molecules insulin ($\approx 5,700$ amu), myoglobin (≈ 17 kDa) and hemoglobin (≈ 66 kDa) the arrival times are shown in figure 5.5 (right). The curves from figure 5.5 were recorded

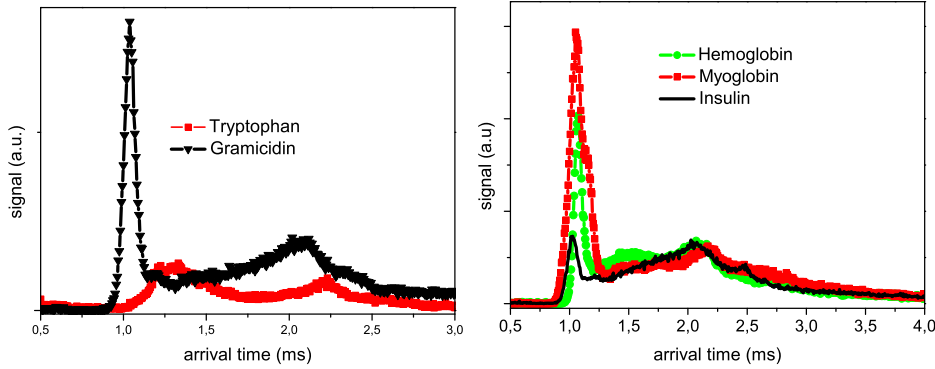


Figure 5.5: *Left: Recorded arrival time distribution of tryptophan and gramicidin. Right: Arrival time distribution of insulin, myoglobin and hemoglobin. For all measurements the same $20 \times 20 \mu\text{m}^2$ chip and a bias current of $20 \pm 1 \mu\text{A}$ was used [164].*

by the same $20 \times 20 \mu\text{m}^2$ SSPD chip and the same bias current of $20 \pm 1 \mu\text{A}$. The two filter gratings, i.e. the $7.5 \mu\text{m}$ copper mesh as well as the 90 nm SiN grating were placed in the beamline to reduce the particle flux and to filter out big aggregates. The opening time of the desorption valve at the source was set to $700 \mu\text{s}$ for all recorded curves in figure 5.5, except for that of tryptophan as discussed below. The valve settings chosen for the SSPD experiment resulted in a double peaked arrival time distribution, since the valve opened shortly for a second time. The amplitudes of the arrival time distributions in figure 5.5 do not allow to draw any conclusions about sensitivity differences for the various molecules. This effect is negligible compared to other experimental factors like the reduction of the SSPD chip sensitivity due to its coverage with molecules.

The question if the high mass particles survived the desorption process intact or leave the source as smaller fragments cannot be answered in a definitive way. Independent detectors would be needed, which also work in that same mass regime. Detectors for neutral particles beyond $2,000$ amu are not easily available, since ionization detectors start to fail above $2,000$ amu,

as discussed in section 1.3.3. Due to this fact checks could only be done for beams of tryptophan and gramicidin, which can be ionized by photo-ionization [105,131]. The 157 nm excimer laser was used in combination with a time-of-flight mass spectrometer to record the arrival time distribution of molecules leaving the source under the same conditions as in combination with the SSPD chip. Figure 5.6 shows a velocity distribution of tryptophan recorded by laser ionization and TOF mass spectrometry using the setup in figure 2.1. The same experimental source settings were used as in the case of the the SSPD experiments. The arrival time distribution recorded

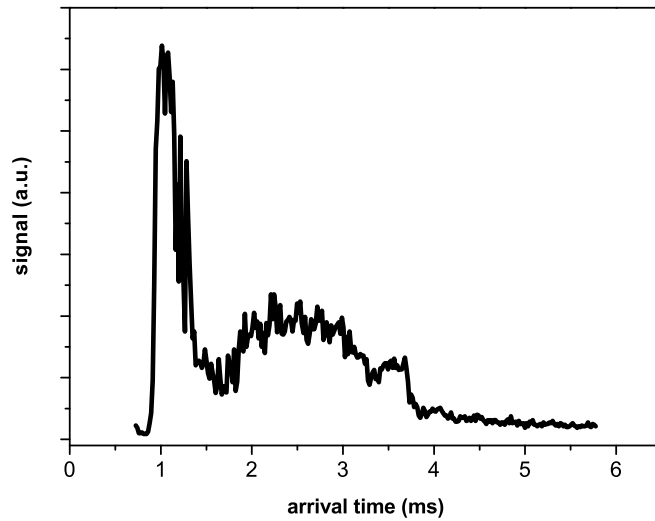


Figure 5.6: *Arrival time distribution of tryptophan recorded by laser post-ionization and time-of-flight mass spectrometry with the same source settings as in the SSPD case. The distribution reproduces the shape recorded by the SSPD chip as shown in figure 5.5 [164].*

via photo-ionization and TOF measurement in figure 5.6 shows the same shape as the one recorded with the SSPD chip from figure 5.5. The curves show a double structure where following the main peak another group of slower molecules arrive. Except for the curve of tryptophan all curves in figure 5.5 have the same time structure, which is reproduced with the TOF-MS as reference method for tryptophan. Only the arrival time distribution for tryptophan in the SSPD case is shifted to retarded times, but keeping the double structure. An explanation for the tryptophan velocity deviation in the SSPD experiment is that the opening time of the valve during the SSPD experiment was accidentally reduced. This is supported by measurements

using the SSPD chip to record arrival times as a function of different valve opening times. Figure 5.7 shows the arrival time distribution for gramicidin for the three different valve opening times: $360\text{ }\mu\text{s}$, $600\text{ }\mu\text{s}$ and $700\text{ }\mu\text{s}$. An opening time of $700\text{ }\mu\text{s}$ shows the main peak centered at around 1 ms followed by a second smaller and broader peak as shown above. The retarded tail of the distribution disappears for an reduced opening time of $600\text{ }\mu\text{s}$. Reducing the opening time further to $360\text{ }\mu\text{s}$ results in a retarded main peak, but with a revival of the second long tail. From the comparison of the arrival time

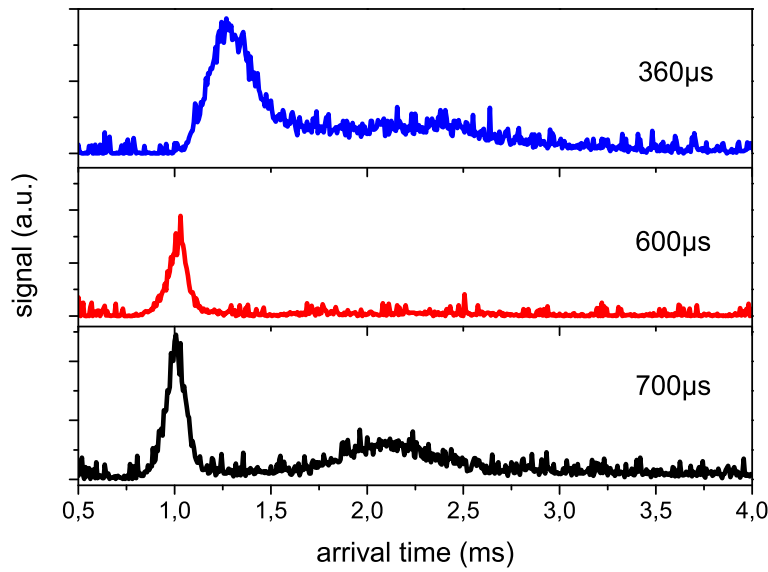


Figure 5.7: Arrival time distribution of gramicidin recorded by a $10\times 10\text{ }\mu\text{m}$ SSPD chip as a function of three different valve opening times. Reducing the valve opening time leads to shift in the arrival time distribution [164].

distributions in figure 5.5 with the arrival time distribution for different valve opening times in figure 5.7, we conclude a reduced valve opening time in the tryptophan measurement leading to the observed velocity shift.

We conclude that the arrival time distributions of the molecules can be reproduced by the SSPD chip and are similar to the ones recorded with the ionization TOF-MS detector for those molecules which can be photo-ionized. Furthermore, the absence of any signal with the carrier gases and the cellulose leads to the conclusion that an energy threshold exists for the SSPD, which can only be reached with sufficient massive and energetic molecules. Dividing the flight distance by the flight time gives the velocity of the beams although possible delays in the mixing channel would lead to an underesti-

mation of the real velocity as shown in section 2.3.1. Therefore the numbers for the kinetic energies can only be considered as lower borders, since the actual velocity might be higher. In the shown experiments the least energetic molecule was tryptophan in a velocity range of 300 to 500 m/s, leading to kinetic energies of 100-300 meV. The helium atoms in the carrier beam would have even at their theoretical supersonic velocity of 1766 m/s a kinetic energy of 65 meV only, whereas the xenon beam with a supersonic speed of about 300 m/s would add up to 60 meV, which are both still below the value for tryptophan. From this consideration an energy threshold must lie somewhere between 60 and 100 meV since tryptophan could be observed, whereas xenon was not detected. The velocity measurements with a chopper presented in section 2.3.1 revealed an actual tryptophan velocity of about 700 m/s for the slowest particles in the case of helium as seed gas (see figure 2.20). Considering this, the upper limit of the threshold would shift to about 500 meV. Not taken into account, however, is the internal energy of the molecules. Nothing is known about how far the internal energy plays a role in the interaction of a molecule and the SSPD surface, i.e. if the heat transfer is fast enough to influence the hot spot formation.

In summary the presented SSPD experiments show the sensitivity of the superconducting chip to single neutral molecules with an energy threshold between 60 to 500 meV.

5.4 Outlook and future SSPD experiments

While this thesis is being written new SSPD experiments are already being set up in Vienna. The main focus of these experiments will be to investigate if the SSPD can distinguish between the internal and external energy of molecules as well as between different energetic molecules. The first experiment will use a thermal fullerene source with optional supersonic expansion, where the flux and velocity are known and the internal energy can be varied by heating of the source exit [186]. An alternative method for the heating of the fullerenes would be thermal heating by a laser beam. By the absorption of photons energy can be stored in the fullerenes in discrete steps depending on the number of absorbed photons. If the SSPD is able to resolve the internal energy of molecules it could be used instead of spectroscopy setups and the ability to distinguish between different energies would allow to obtain also the masses of the molecules if the velocities are measured as well. This would

make them interesting for mass spectroscopy, especially since no ionization is needed anymore.

Also new cleaning procedures will be examined for covered 'dirty' chips. This will include laser desorption, heating, ion sputtering and chemical methods.

In the meantime new SSPD designs are available, which consist of several meandering nanowires coupled in parallel to a whole device [187,188]. This design allows in the case of photons to resolve the number of the incident light quanta. Future developments towards even a higher number of these coupled SSPDs may allow to spatially resolve photons and probably also a molecular beam similar to a CCD chip.

Chapter 6

Summary

In this work we presented a new source for organic molecules, clusters and organo-metallic complexes and a superconducting detector. Both are particularly beneficial for improving the mass and the complexity of neutral molecules for applications especially for matter wave interference.

Standard effusive sources lack the ability to produce intense beams of biomolecules due to fragmentation in the evaporation process. The laser desorption source with additional supersonic cooling is capable of producing beams of cold biomolecules, where the velocity can be tuned by varying the seed gas. Our laser desorption source produces beams of biomolecules, that are compatible with an Talbot-Lau interferometer. The produced molecular beam has to fulfill the following criteria:

- An intense beam of large neutral biomolecules.
- A tunable velocity to match the Talbot condition.
- A stable signal to resolve the interference pattern.

The first point has been tested intensively during this work and resulted in a source design, which works for small amino acids as well as for massive biomolecules. The velocity can be easily tuned within the given velocity distribution by changing the timing between the desorption and ionization laser. The whole velocity distribution can be shifted by changing to heavier seed gas, which results in lower velocities. The signal stability can be kept within 6% of the signal amplitude by normalizing the signal with two separated ionization lasers.

With short pulse one- and two-photon ionization it was possible to ionize molecules ranging from small amino acids to large polypeptides. The largest post-ionized single molecule was gramicidin with nearly 2000 amu. Applying post-ionization to heavy single molecules did not result in any detectable ion signal, which reproduces the general mass limit for post-ionization of massive molecules.

Beside the production of isolated molecules also the production of huge bio-complexes was studied. The observation of large pure tryptophan clusters, as well as clusters with one or several embedded metal atoms, led to the gas-phase production of clusters with masses up to 7,000 amu. The inclusion of a single or at most a few metal atoms into tryptophan clusters is observed for alkaline, alkaline earth metals and copper atoms. Further studies on the formation of pure biomolecular clusters led to the observation of a gramicidin tetramer with a mass of about 7530 amu and to gramicidin-tryptophan clusters with several tryptophan molecules attached to a single gramicidin molecule.

The formation of these large clusters is interesting for matter wave interferometry for two reasons: First, masses of several thousand atomic mass units can be reached by keeping post-ionization as detection method. Second, since very little is known about the structural, electronic, optical, thermal or magnetic properties of such organic neutral complexes in the gas-phase, quantum interference enhanced metrology experiments are expected to reveal new insight. Measurements of cluster polarizabilities and dipole moments can be helpful in developing models for these clusters. Especially interesting in that context is the observation of magic clusters, where more insight into their properties could help to understand their predominance. Another question of interest is also, what exactly influences the number of included atoms into tryptophan clusters.

In addition to the production of large molecules, we presented a new detection method for neutral molecules. A superconducting single photon detector (SSPD) has been successfully tested for its sensitivity to impacting neutral molecules. The experiments have shown, that the SSPD is able to reproduce the velocity distributions of neutral molecules. Beside tryptophan and gramicidin the SSPD could also resolve the velocity distribution of the heavier molecules like insulin, myoglobin and hemoglobin. It was not yet possible to verify independently, whether the heavy molecules reach the detector intact. This is due to the lack of other detection methods for this

mass range. The lightest molecule seen by the SSPD was tryptophan. The even lighter xenon atom did not trigger the detector at all. From that fact one can estimate an energy threshold of the SSPD in the range between 60 and 500 meV. It is still an open question how the internal energy of molecules contributes to the detection event. Experiments to clarify that questions are currently in preparation. If the internal energy also adds to the detection threshold there is reason to hope that even large molecules at moderate velocities, as required for matter wave interference, would lead to a detectable signal. The SSPD will maybe close the need for a new kind of detection method for the next generations of molecular interferometers.

Biomolecule interference will be continued in the near future, since metrology of the various presented molecules and complexes may provide a great deal of new insight and perhaps stimulate further cooperation between experimentalists, theoreticians and computational scientists.

Appendix

A) TOF settings

Typical voltage values used for the TOF can be found in table 6.1.

TOF element	Voltage
Repeller	1.52 kV
Liner I	-7.4 kV
Liner II	-16.3 kV
Lens	-8.1 kV
MCP	2 kV

Table 6.1: Typical voltage settings of the TOF mass spectrometer components.

The formula for the mass calibration is given by

$$m = \sqrt{A * t + B}, \quad (6.1)$$

where m is the mass of the ion, t is the flight time from the repeller to the MCP and A and B are two fit parameters, which can be obtained by calibration with at least two known masses. The calibration from 3/Dec/2007 (see figure 6.1) for tryptopan (204 amu), β -carotene (536 amu) and gramicidin A (1,884 amu) resulted in $A=2.678E6 \pm 1.1E3$ and $B=-0.603 \pm 0.012$ for TOF settings as shown in table 6.1.

B) Valve characterization

The following table lists the comparison of the real opening time of the valve in contrast to the set opening time for a typical valve setting. Changing the

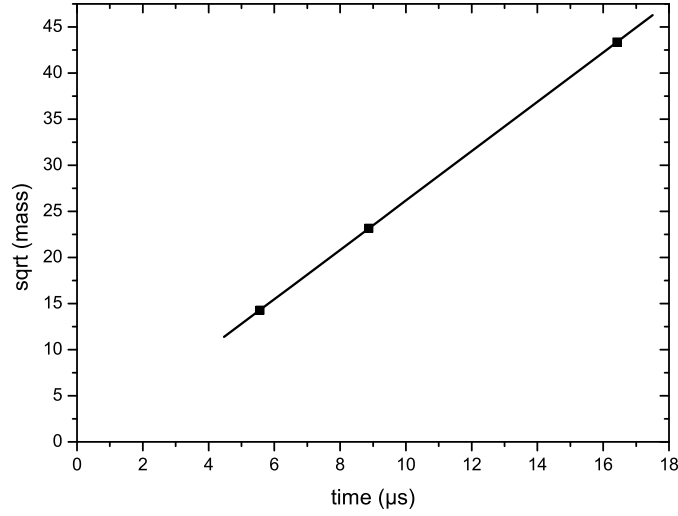


Figure 6.1: The measured flight times inside of the TOF-MS are shown for tryptophan, β -carotene and gramicidin. A linear fit with eq. 6.1 gives the parameters A and B : $A=2.678E6\pm1.1E3$ and $B=-0.603\pm0.012$.

force on the poppit can lead to a change of the opening times.

C) Signal stabilization

The signal stabilization of the laser desorption source as described in section 2.3.2 has to be modified slightly, if it is used in combination with an interferometer. After the molecular beam traveled through the Talbot-Lau interferometer described in chapter 3, it has a sinus variation added to its intrinsic beam fluctuations. If the sinus variation is on both probed velocity classes the ratio will still be a constant and the sinus would not be visible. In order to filter the fluctuations while keeping the sinus pattern, one has to select two different velocity classes. One velocity showing interference structures and the second velocity resulting in zero visibility. In that case the ratio between the two signals shows the interference structure, since the source fluctuations are on both signals in the same way, but the superposed sinus variation is only present in one of the two velocity classes. Figure 6.2 (top) shows the signals of the VUV signal and the UV signal, where the later has mathematically added a sinus with 10% visibility and a period of 30 points to simulate an interference pattern for that signal. The added sinus shape completely vanishes inside the signal fluctuations, but by calculating the ratio

set time (μs)	real time (μs)	set time (μs)	real time (μs)
200	210	600	604
250	245	650	566
300	308	700	599
350	367	750	691
400	481	800	778
450	560	850	820
500	566	900	903
550	570		

Table 6.2: Comparison of the set valve opening time and the actual opening time (FWHM) measured with a fast ion gauge 1.5 cm away from the valve orifice with helium.

of the two signals the periodicity of the sinus again becomes visible, whereas the fluctuations are suppressed (see figure 6.2 (bottom)). The described method relies on the fact that two signals are available, where the interference pattern is superposed only on one of the two. If no velocity class is available without visibility a special setup can handle that case. As discussed in section 3 a rolling of the gratings with respect to each other results in a reduced visibility or in worst case also in no visibility at all. This effect is dependent on the height of the detected molecular beam. If the gratings are rolled with respect to each other each beam height will experience a different phase shift as depicted in figure 6.3. By leaving one ionization laser large in height and rolling one of the gratings the visibility will vanish, whereas for a small ionization laser height the interference pattern is still present. Therefore the combination of the two laser spots with different dimensions in height guaranties that the interference pattern will vanish for the larger one, whereas the small laser spot preserves the sinus pattern.

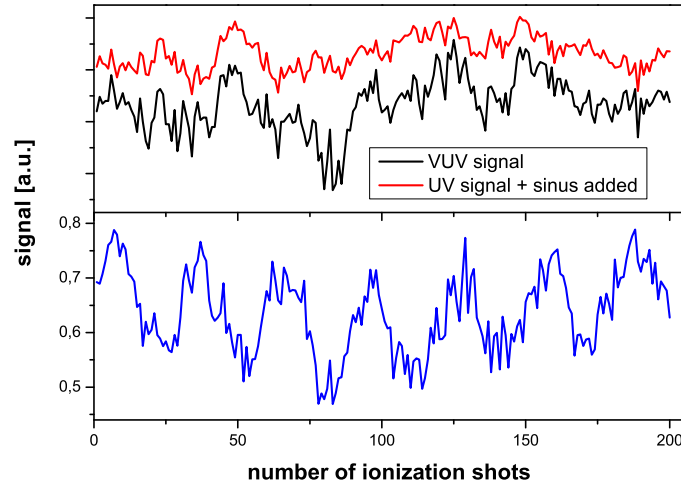


Figure 6.2: Top: UV laser signal plus a theoretically added sinus with 10% visibility and a period of 30 points and the pure VUV signal. Bottom: Ratio of the signals, which is free of fluctuations but reveals the artificial sinus structure of the UV signal.

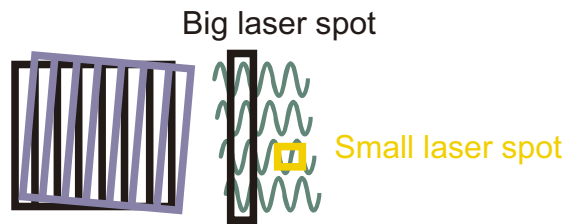


Figure 6.3: A rolling of the gratings leads to a height dependent phase shift of the molecules. Detecting the molecules over a large height will smear out the interference pattern, whereas for a small detection height the phase shift can be neglected.

List of publications

- M. Marksteiner, G. Kiesewetter, L. Hackermüller, H. Ulbricht and M. Arndt: *Cold Beams of Biomolecules for Quantum Optics*, Acta Phys. Hung. B, **26**, 87-94, 2006
- M. Marksteiner, P. Haslinger, H. Ulbricht, M. Sclafani, H. Oberhofer, C. Dellago and M. Arndt: *Gas-Phase Formation of Large Neutral Alkaline-Earth Metal Tryptophan Complexes*, J. Am. Soc. Mass Spectrom., **19**, 1021-1026, 2008
- M. Marksteiner, P. Haslinger, M. Sclafani, H. Ulbricht and M. Arndt: *UV and VUV Ionization of Organic Molecules, Clusters and Complexes*, J. Phys. Chem. A, **113**, 9952-9957, 2009
- M. Marksteiner, A. Divochiy, M. Sclafani, P. Haslinger, H. Ulbricht, A. Korneev, A. Semenov, G. Gol'tsman and M. Arndt: *A superconducting NbN detector for neutral nanoparticles*, Nanotechnology, **20**, 455501, 2009
- M. Arndt, M. Berninger, S. Deachapunya, S. Gerlich, L. Hackermüller, A. G. Major, M. Marksteiner, A. Stefanov and H. Ulbricht: *On the prospects of interferometry and deflectometry for characterizing large molecules*, Eur. Phys. J. Special Topics, **159**, 1–9, 2008

Bibliography

- [1] E. W. SCHLAG, J. GROTEMEYER, and R. D. LEVINE, *Chem. Pyhs. Lett.* **190**, 521 (1992).
- [2] E. W. SCHLAG and R. D. LEVINE, *Phys. Chem.* **96**, 10608 (1992).
- [3] C. H. BECKER and K. J. WU, *Am. Soc. Mass Spectrom.* **6**, 883 (1995).
- [4] M. PLANCK, *Verhandl. Dtsch. phys. Ges.* **2**, 1 (1900).
- [5] A. EINSTEIN, *Ann. Physik* **17**, 132 (1905).
- [6] L. DE BROGLIE, *Nature* **112**, 540 (1923).
- [7] C. DAVISSON and L. H. GERMER, *Nature* **119**, 558 (1927).
- [8] G. P. THOMSON, *Nature* **120**, 802 (1927).
- [9] I. ESTERMANN and O. STERN, *Z. Phys.* **61**, 95 (1930).
- [10] H. V. HALBAN JNR. and P. PREISWERK, *C.R. Acad. Sci. Paris* **203**, 73 (1936).
- [11] H. RAUCH and A. WERNER, *Neutron Interferometry: Lessons in Experimental Quantum Mechanics*, Oxford Univ. Press, 2000.
- [12] V. F. SEARS, *Oxford University Press* (1989).
- [13] P. L. GOULD, G. A. RUFF, and D. E. PRITCHARD, *Phys. Rev. Lett.* **56**, 827 (1986).
- [14] P. J. MARTIN, B. G. OLDAKER, A. H. MIKLICH, and D. E. PRITCHARD, *Phys. Rev. Lett.* **60**, 515 (1988).

- [15] D. W. KEITH, M. L. SCHATTENBURG, H. I. SMITH, and D. E. PRITCHARD, *Phys. Rev. Lett.* **61**, 1580 (1988).
- [16] D. W. KEITH, C. R. EKSTROM, Q. A. TURCHETTE, and D. E. PRITCHARD, *Phys. Rev. Lett.* **66**, 2693 (1991).
- [17] C. BORDÉ, N. COURTIER, F. D. BURCK, A. GONCHAROV, and M. GORLICKI, *Phys. Lett. A* **188**, 187 (1994).
- [18] M. CHAPMAN, C. R. EKSTROM, T. D. HAMMOND, J. SCHMIED-MAYER, B. E. TANNIAN, S. WEHINGER, and D. E. PRITCHARD, *Phys. Rev. A* **51**, R14 (1995).
- [19] C. LISDAT, M. FRANK, H. KNÖCKEL, M. L. ALMAZOR, and E. TIE-MANN, *Eur. Phys. J. D* **12**, 235 (2000).
- [20] W. SCHÖLLKOPF and J. TOENNIES, *J. Chem. Phys.* **104**, 1155 (1996).
- [21] R. BRÜHL, R. GUARDIOLA, A. KALININ, O. KORNILOV, J. NAVARRO, T. SAVAS, and J. P. TOENNIES, *Phys. Rev. Lett.* **92**, 185301 (2004).
- [22] T. REISINGER, A. A. PATEL, H. REINGRUBER, K. FLADISCHER, W. E. ERNST, G. BRACCO, H. I. SMITH, and B. HOLST, *Phys. Rev. A* **79**, 053823 (2009).
- [23] R. PENROSE, *Gen. Rel. Grav.* **28**, 581 (1996).
- [24] A. J. LEGGETT, *J. Phys.: Condens. Matter* **14**, R415 (2002).
- [25] C. H.-T. WANG, R. BINGHAM, and J. T. MENDONCA, *Class. Quant. Grav.* **23**, L59 (2006).
- [26] S. CARLIP, *Class. Quant. Grav.* **25**, 154010 (2008).
- [27] M. ARNDT, O. NAIRZ, J. VOSS-ANDREAE, C. KELLER, and G. V. DER ZOUWANDA. ZEILINGER, *Nature* **401**, 680 (1999).
- [28] M. ARNDT, O. NAIRZ, J. PETSCHINKA, and A. ZEILINGER, *C.R. Acad. Sci. Paris t. 2, Série IV*, 1 (2001).
- [29] O. NAIRZ, B. BREZGER, M. ARNDT, and A. ZEILINGER, *Phys. Rev. Lett.* **87**, 160401 (2001).

- [30] B. BREZGER, L. HACKERMÜLLER, S. UTTENTHALER, J. PET-SCHINKA, M. ARNDT, and A. ZEILINGER, *Phys. Rev. Lett.* **88**, 100404 (2002).
- [31] L. HACKERMÜLLER, S. UTTENTHALER, K. HORNBERGER, E. REIGER, B. BREZGER, A. ZEILINGER, and M. ARNDT, *Phys. Rev. Lett.* **91**, 90408 (2003).
- [32] S. GERLICH, L. HACKERMÜLLER, K. HORNBERGER, A. STIBOR, H. ULBRICHT, M. GRING, F. GOLDFARB, T. SAVAS, M. MURI, M. MAYOR, and M. ARNDT, *Nat Phys* **3**, 711 (2007).
- [33] T. JUFFMANN, S. TRUPPE, P. GEYER, A. G. MAJOR, S. DEACHAPUNYA, H. ULBRICHT, and M. ARNDT, *Phys. Rev. Lett.* **103**, 263601 (2009).
- [34] C. EKSTROM, J. SCHMIEDMAYER, M. CHAPMAN, T. HAMMOND, and D.E.PRITCHARD, *Phys. Rev. A* **51**, 3883 (1995).
- [35] M. B. G. T. A. MIFFRE, M. JACQUEY and J. VIGUE, *Phys. Rev. A* **73**, 011603(R) (2006).
- [36] D. WEISS, B. YOUNG, and S. CHU, *Phys. Rev. Lett.* **70**, 2706 (1993).
- [37] J. SCHMIEDMAYER, M. CHAPMAN, C. EKSTROM, T. HAMMOND, S.WEHINGER, and D. PRITCHARD, *Phys. Rev. Lett.* **74**, 1043 (1995).
- [38] M. BERNINGER, A. STEFANOV, S. DEACHAPUNYA, and M. ARNDT, *Phys. Rev. A* **76**, 013607 (2007).
- [39] L. HACKERMÜLLER, K. HORNBERGER, S. GERLICH, M. GRING, H. ULBRICHT, and M. ARNDT, *Appl. Phys.B* **89**, 469 (2007).
- [40] S. DEACHAPUNYA, A. STEFANOV, M. BERNINGER, H. ULBRICHT, E. REIGER, N. L. DOLTSINIS, and M. ARNDT, *The Journal of Chemical Physics* **126**, 164304 (2007).
- [41] S.GERLICH, M. GRING, H. ULBRICHT, K. H. J. TÜXEN, M. MAYOR, and M. ARNDT, *Angew. Chem. Int. Ed. Engl.* **47**, 6195 (2008).

- [42] M. GRING, S. GERLICH, S. EIBENBERGER, S. NIMMRICHTER, T. BARRIDA, M. ARNDT, H. ULBRICHT, K. HORNBERGER, M. MÜRI, M. MAYOR, M. BÖCKMANN, and N. L. DOLTSINIS, *Phys. Rev. A* **81**, 031604 (2010).
- [43] J. TÜXEN, S. GERLICH, S. EIBENBERGER, M. ARNDT, and M. MAYOR, *Chem. Commun.* **46**, 4145 (2010).
- [44] S. NIMMRICHTER, K. HORNBERGER, and M. ARNDT, *Phys. Rev. A* **78**, 063607 (2008).
- [45] S. MIRZA and C. SHAKHER, *Optical Engineering* **44**, 013601 (2005).
- [46] M. THAKUR, C. QUAN, and C. J. TAY, *Optics and Laser Technology* **39**, 453 (2007).
- [47] W. B. CASE, M. TOMANDL, S. DEACHAPUNYA, and M. ARNDT, *Optics Express* **17**, 20966 (2009).
- [48] B. J. MCMORRAN and A. D. CRONIN, *New Journal of Physics* **11**, 033021 (2009).
- [49] J. F. CLAUSER and S. LI, *Phys. Rev. A* **49**, R2213 (1994).
- [50] J. F. CLAUSER and S. LI, *Phys. Rev. A* **50**, 2430 (1994).
- [51] S. NOWAK, C. KURTSIEFER, T. PFAU, and C. DAVID, *Opt. Lett.* **22**, 1430 (1997).
- [52] S. B. CAHN, A. KUMARAKRISHNAN, U. SHIM, T. SLEATOR, and P. R. B. DUBETSKY, *Phys. Rev. Lett.* **79**, 784 (1997).
- [53] H. F. TALBOT, *Philos. Mag.* **9**, 401 (1836).
- [54] M. ARNDT, *Matter Waves*, University of Vienna, 2002.
- [55] E. LAU, *Ann. Phys.* **6**, 417 (1948).
- [56] K. PATORSKI, Self-Imaging and its Applications, in *Progress in Optics XXVII*, edited by E. WOLF, pp. 2–108, Elsevier Science Publishers B. V., Amsterdam, 1989.
- [57] K. . PATORSKI, *Optica Acta* **30**, 745 (1983).

- [58] K. BANASZEK, K. WODKIEWICZ, and W. P. SCHLEICH, *Optics Express* **2**, 169 (1998).
- [59] C. JÖNSSON, D. BRANDT, and S. HIRSCHI, *Am. J. Phys.* **42**, 4 (1973).
- [60] F. HASSELBACH and U. MAIER, *Quantum Coherence and Decoherence, Proc. ISQM-Tokyo'98, Amsterdam, Elsevier*, 299 (1999).
- [61] G. MEIJER, M. S. DE VRIES, H. E. HUNZIKER, and H. R. WENDT, *Appl. Phys. B* **51**, 395 (1990).
- [62] A. KANTROWITZ and J. GREY, *Rev. Sci. Instrum.* **22**, 328 (1951).
- [63] G. B. KISTIAKOWSKY and W. P. SLICHTER, *Rev. Sci. Instrum.* **22**, 333 (1951).
- [64] G. SCOLES, editor, *Atomic and Molecular Beam Methods*, Oxford University Press, 1988.
- [65] H. HABERLAND, editor, *Clusters of Atoms and Molecules*, Springer, 1994.
- [66] H. PAULY, *Atom, Molecule, and Cluster Beams I*, Springer, 2000.
- [67] J. B. ANDERSON and J. B. FENN, *The Physics of Fluids* **8**, 780 (1965).
- [68] R. E. SMALLEY, L. WHARTON, and D. H. LEVY, *Acc. Chem. Res.* **10**, 139 (1977).
- [69] J. P. TOENNIES and K. WINKELMANN, *J. Chem. Phys.* **66**, 3965 (1977).
- [70] A. AMIRAV, U. EVEN, and J. JORTNER, *Chemical Physics* **51**, 31 (1980).
- [71] G. M. MCCLELLAND, K. L. SAENGER, J. J. VALENTINI, and D. R. HERSCHBACH, *Physical Chemistry* **83**, 947 (1979).
- [72] J. P. TOENNIES and A. F. VILESOV, *Angew. Chem.* **43**, 2622 (2004).
- [73] M. HILLENKAMP, S. KEINA, and U. EVEN, *J. Chem. Phys.* **118**, 8699 (2003).

- [74] U. EVEN, J. JORTNER, D. NOY, N. LAVIE, and C. COSSART-MAGOS, *J. Chem. Phys.* **112**, 8068 (2000).
- [75] J. WANG, V. A. SHAMAMIAN, B. R. THOMAS, J. M. WILKINSON, J. RILEY, C. F. GIESE, and W. R. GENTRY, *Phys. Rev Lett.* **60**, 696 (1988).
- [76] F. LUO, G. C. MCBANE, G. KIM, C. F. GIESE, and W. R. GENTRY, *J. Chem. Phys.* **98**, 3564 (1993).
- [77] M. DEY, F. MORITZ, G. H. ATKINSON, J. GROTEMEYER, and E. SCHLAG, *J. Chem. Phys.* **95**, 4584 (1991).
- [78] K. TANAKA, H. WAKI, Y. IDO, S. AKITA, Y. YOSHIDA, and T. YOSHIDA, *Rapid Communications in mass spectrometry* **2**, 151 (1988).
- [79] M. KARAS, D. BACHMANN, and F. HILLENKAMP, *Anal. Chem.* **57**, 2935 (1985).
- [80] F. HILLENKAMP, M. KARAS, R. C. BEAVIS, and B. T. CHAIT, *Am. Chem. Soc.* **63**, 1193 (1991).
- [81] F. HILLENKAMP and M. KARAS, *Int. J. Mass Spectro.* **200**, 71 (2000).
- [82] R. L. LEVIS, *Laser desorption and ejection of biomolecules from the condensed phase into the gas phase* **45**, 483 (1994).
- [83] F. J. VASTOLA, R. O. MUMMA, and A. J. PIRONE, *Organic Mass Spectrometry* **3**, 101 (1969).
- [84] R. O. MUMMA and F. J. VASTOLA, *Organic Mass Spectrometry* **6**, 1373 (1972).
- [85] M. A. POSTHUMUS, P. G. KISTEMAKER, H. L. C. MEUZELAAR, and M. C. T. N. DE BRAUW, *Anal. Chem.* **50**, 985 (1978).
- [86] M. KARAS and F. HILLENKAMP, *Anal. Chem.* **60**, 2299 (1988).
- [87] M. KARAS, U. BAHR, A. INGENDOH, and F. HILLENKAMP, *Angew. Chem. Int.* **28**, 760 (1989).
- [88] Y. CAI, W.-P. PENG, S.-J. KUO, S. SABU, C.-C. HAN, and H.-C. CHANG, *Anal. Chem.* **74**, 4434 (2002).

- [89] J. GROTEMEYER, U. BOSEL, K. WALTER, and E. W. SCHLAG, *J. Am. Chem. Soc.* **108**, 4233 (1986).
- [90] R. N. ZARE, J. H. HAHN, and R. ZENOBI, *Bull. Chem. Soc. Jpn.* **61**, 87 (1988).
- [91] L. LI and D. LUBMAN, *Appl. Spectr.* **42**, 381 (1988).
- [92] G. R. KINSEL, J. LINDNER, J. GROTEMEYER, and E. W. SCHLAG, *J. Phys. Chem.* **95**, 7824 (1991).
- [93] B. SPENGLER, M. KARAS, U. BAHR, and F. HILLENKAMP, *J. Phys. Chem.* **91**, 6502 (1987).
- [94] Y. LI, R. T. MCLVER, and J. C. HEMMINGER, *J. Chem. Phys.* **93**, 4719 (1990).
- [95] K. DREISEWERD, M. SCHÜRENBERG, M. KARAS, and F. HILLENKAMP, *Int. J. Mass Spectro. Ion. Proc.* **154**, 171 (1996).
- [96] P. DEMIREV, A. WESTMANN, C. T. REIMANN, P. HAKANSSON, D. BAROFSKY, B. U. R. S. ANDY. D. CHENG, W. SEIBT, and K. SIEGBAHN, *Rapid Communications in mass spectrometry* **6**, 187 (1992).
- [97] S. V. CHEKALIN, V. V. GOLOVLEV, A. A. KOZLOV, Y. A. MATVEYETS, A. P. YARTSEV, and V. S. LETOKHOV, *J. Phys. Chem.* **92**, 6855 (1988).
- [98] K. DREISEWERD, *Chem. Rev.* **103**, 395 (2003).
- [99] D. DING, J. HUANG, R. N. COMPTON, C. E. KLOTS, and R. E. HAUFLER, *Phys. Rev. Lett.* **73**, 1084 (1994).
- [100] J. DE VRIES, H. STEGER, B. KAMKE, C. MENZEL, B. WEISSER, W. KAMKE, and I. V. HERTEL, *Chem. Phys. Lett.* **188**, 159 (1992).
- [101] E. E. B. CAMPBELL, G. ULMER, and I. V. HERTEL, *Phys. Rev. Lett.* **67**, 1986 (1991).
- [102] G. V. HELDEN, I. HOLLEMAN, A. A. V. ROJI, G. M. H. KNIPPELSAND, A. F. G. V. DER MEER, and G. MEIJER, *Phys. Rev. Lett.* **81**, 1825 (1998).

- [103] K. R. WILSON, M. JIMENEZ-CRUZ, C. NICOLAS, L. BELAU, S. R. LEONE, and M. AHMED, *The Journal of Physical Chemistry A* **110**, 2106 (2006).
- [104] U. SCHÜHLE, J. B. PALLIX, and C. H. BECKER, *J. Am. Chem. Soc.* **110**, 2323 (1988).
- [105] J. ARPS, C. CHEN, M. MCCANN, and I. DATSKOU, *Applied Spectroscopy* **43**, 1211 (1989).
- [106] D. J. BUTCHER, *Microchemical Journal* **62**, 354 (1999).
- [107] Y. J. SHI and R. H. LIPSON, *Can. J. Chem.* **83**, 1891 (2005).
- [108] K. R. WILSON, L. BELAU, C. NICOLAS, M. JIMENEZ-CRUZ, S. R. LEONE, and M. AHMED, *Int. J. Mass Spectrom.* **249–250**, 155 (2006).
- [109] L. HANLEY, O. KORNIENKO, E. T. ADA, E. FUOCO, and J. L. TREVOR, *J. Mass Spectrom.* **34**, 705 (1999).
- [110] L. HANLEY and R. ZIMMERMANN, *Anal. Chem.* **81**, 4174 (2009).
- [111] L. HANLEY, P. EDIRISINGHE, W. CALAWAY, I. VERYOVKIN, M. PELLIN, and J. MOORE, *Applied Surface Science* **252**, 6723 (2006).
- [112] P. EDIRISINGHE, J. MOORE, W. CALAWAY, I. VERYOVKIN, V. IGOR, M. PELLIN, and L. HANLEY, *Anal. Chem.* **78**, 5876 (2006).
- [113] S. N. DIXIT and V. MCKOY, *Chem. Phys.* **82**, 3546 (1985).
- [114] R. WEINKAUF, P. AICHER, G. WESLEY, J. GROTEMEYER, and E. W. SCHLAG, *Phys. Chem.* **98**, 8381 (1994).
- [115] C. H. BECKER and J. S. HOVIS, *J. Vac. Sci. Technol. A* **12**, 2352 (1994).
- [116] C. R. AYRE, L. MORO, and C. H. BECKER, *Anal. Chem.* **66**, 1610 (1994).
- [117] K. P. AICHER, U. WILHELM, and J. GROTEMEYER, *Am. Soc. Mass Spectrom.* **6**, 1059 (1995).

- [118] K. W. D. LEDINGHAM and R. P. SINGHAL, *Int. J. Mass Spectrom. Ion Process.* **163**, 149 (1997).
- [119] N. P. LOCKYER and J. C. VICKERMAN, *Int. Mass Spectrom.* **176**, 77 (1998).
- [120] C. KÖSTER, J. GROTEMEYER, and E. W. SCHLAG, *Z. Naturforsch.* **45a**, 1285 (1990).
- [121] D. S. ANEX, M. S. DE VRIES, A. KNEBELKAMP, J. BARGON, H. R. WENDT, and H. E. HUNZIKER, *Int. J. Mass Spectrom. Ion Process.* **131**, 319 (1994).
- [122] M. MARKSTEINER, P. HASLINGER, H. ULBRICHT, M. SCLAFANI, H. OBERHOFER, C. DELLAGO, and M. ARNDT, *J. Am. Soc. Mass Spectrom.* **19**, 1021 (2008).
- [123] M. MARKSTEINER, P. HASLINGER, M. SCLAFANI, H. ULBRICHT, and M. ARNDT, *J. Phys. Chem. A* **113**, 9952 (2009).
- [124] M. S. DE VRIES and H. E. HUNZIKER, *J. Photochem. Photobiol.* **106**, 31 (1997).
- [125] M. S. DE VRIES and H. E. HUNZIKER, *Appl. Surf. Sci.* **106**, 466 (1996).
- [126] A. AMIRAV, *Organic Mass Spectrometry* **26**, 1 (1991).
- [127] C. WEICKHARDT, L. DRAAK, and J. GROTEMEYER, *Eur. J. Mass Spectrom.* **6**, 319 (2000).
- [128] C. WEICKHARDT, L. DRAACK, and A. AMIRAV, *Anal. Chem.* **75**, 5602 (2003).
- [129] W. C. WILEY and I. H. MCLAREN, *Rev. Sci. Instrum.* **26**, 1150 (1955).
- [130] T. R. RIZZO, Y. D. PARK, L. A. PETEANU, and D. H. LEVY, *J. Chem. Phys.* **84**, 2534 (1986).
- [131] C. KÖSTER and J. GROTEMEYER, *Organic Mass Spectrometry* **27**, 463 (1992).

- [132] R. C. BEAVIS and B. T. CHAIT, *Rapid Commun Mass Spectrom* **3**, 439 (1989).
- [133] D. DEHARENG and G. DIVE, *Int. J. Mol. Sci.* **5**, 301 (2004).
- [134] T. R. RIZZO, Y. D. PARK, and D. H. LEVY, *J. Chem. Phys.* **85**, 6945 (1986).
- [135] A. LINDINGER, J. P. TOENNIES, and A. F. VILESOV, *J. Chem. Phys.* **110**, 1429 (1999).
- [136] L. C. SNOEK, R. T. KROEMER, M. R. HOCKRIDGE, and J. P. SIMONS, *Phys. Chem. Chem. Phys.* **3**, 1819 (2001).
- [137] T. R. RIZZO, Y. D. PARK, L. A. PETEANU, and D. H. LEVY, *J. Chem. Phys.* **84**, 2534 (1995).
- [138] W. A. DE HEER, *Rev. Mod. Phys.* **65**, 611 (1993).
- [139] J. R. CABLE, M. J. TUBERGEN, and D. LEVY, *J. Am. Chem. Soc.* **111**, 9032 (1989).
- [140] G. KIESEWETTER, *Laser Desorption as a Source for Matter Wave Interferometry*, 2006.
- [141] M. MARKSTEINER, G. KIESEWETTER, L. HACKERMÜLLER, H. ULBRICHT, and M. ARNDT, *Acta Phys. Hung. B* **26**, 87 (2006).
- [142] B. WITZEL, C. J. G. UITERWAAL, H. SCHRÖDER, D. CHARALAMBIDIS, and K.-L. KOMPA, *Phys. Rev. A* **58**, 3836 (1998).
- [143] N. GOTSCHKE, H. ULBRICHT, and M. ARNDT, *Laser Phys.* **17**, 583 (2007).
- [144] T. A. SAVAS, S. N. SHAH, M. L. SCHATTENBURG, J. M. CARTER, and H. I. SMITH, *J. Vac. Sci. Technol.* **B 13**, 2732 (1995).
- [145] S. NIMMRICHTER and K. HORNBERGER, *Phys. Rev. A* **78**, 023612 (2008).
- [146] S. NIMMRICHTER, *Matter wave Talbot Lau interferometry beyond the eikonal approximation*, 2007.

- [147] S. TRUPPE, *Molecular Lithography - A Quantum Optical Approach*, University of Vienna, 2009.
- [148] K. HORNBERGER, S. GERLICH, H. ULBRICHT, L. HACKERMÜLLER, S. NIMMRICHTER, I. V. GOLDT, O. BOLTALINA, and M. ARNDT, *New Journal of Physics* **11**, 043032 (2009).
- [149] H. ULBRICHT, M. BERNINGER, S. DEACHAPUNYA, A. STEFANOV, and M. ARNDT, *Nanotechnology* **19**, 045502 (2008).
- [150] M. DEY and J. GROTEMEYER, *Eur. J. Mass Spectrom.* **1**, 95 (1995).
- [151] J. B. FENN, M. MANN, C. K. MENG, S. F. WONG, and C. M. WHITEHOUSE, *Science* **246**, 64 (1989).
- [152] R. B. COLE, *Electrospray Ionization Mass Spectrometry*, Wiley, New York, 1997.
- [153] P. NEMES, G. SCHLOSSER, and K. VEKEY, *Mass Spectrom.* **40**, 43 (2005).
- [154] I. COMPAGNON, T. TABARIN, R. ANTOINE, M. BROYER, P. DUGOUR, R. MITRIC, J. PETERSEN, and V. BONACIC-KOUTECKY, *Chem. Phys.* **125**, 164326 (2006).
- [155] K. J. KOCH, T. AGGERHOLM, S. C. NANITA, and R. G. COOKS, *Mass Spectrom.* **37**, 676 (2002).
- [156] T. AGGERHOLM, S. C. NANITA, K. J. KOCH, and R. G. COOKS, *Mass Spectrom.* **38**, 87 (2003).
- [157] S. MYUNG, R. R. JULIAN, S. C. NANITA, R. G. COOKS, and D. E. CLEMMER, *Phys. Chem. B* **108**, 6105 (2004).
- [158] Z. TAKATS, S. C. NANITA, R. G. COOKS, G. SCHLOSSER, and K. VEKEY, *Anal. Chem.* **75**, 1514 (2003).
- [159] N. C. POLFER, J. OOMENS, and R. C. DUNBAR, *Phys. Chem. Chem. Phys.* **8**, 2744 (2006).
- [160] I. POCSIK, *Z. Phys. D* **20**, 395 (1991).

- [161] L. KALE, R. SKEEL, M. BHANDARKAR, R. BRUNNER, A. GURSOY, N. KRAWET, J. PHILLIPS, A. SHINOZAKI, K. VARADARAJAN, and K. SCHULTEN, *Journal of Computational Physics* **151**, 283 (1999).
- [162] A. D. MACKERELL, M. FEIG, and C. L. B. III, *J. Comput. Chem.* **25**, 1400 (2004).
- [163] A. D. MACKERELL, D. BASHFORD, BELLOTT, R. L. DUNBRACK, J. D. EVANSECK, M. J. FIELD, S. FISCHER, J. GAO, H. GUO, S. HA, D. JOSEPH-MCCARTHY, L. KUCHNIR, K. KUCZERA, F. T. K. LAU, C. MATTOS, S. MICHNICK, T. NGO, D. T. NGUYEN, B. PRODHOM, W. E. REIHER, B. ROUX, M. SCHLENKRICH, J. C. SMITH, R. STOTE, J. STRAUB, M. WATANABE, J. WIORKIEWICZ-KUCZERA, D. YIN, and M. KARPLUS, *The Journal of Physical Chemistry B* **102**, 3586 (1998).
- [164] M. MARKSTEINER, A. DIVOCHIY, M. SCLAFANI, P. HASLINGER, H. ULBRICHT, A. KORNEEV, A. SEMENOV, G. GOL'TSMAN, and M. ARNDT, *Nanotechnology* **20**, 455501 (2009).
- [165] F. LOW, *Journal of the optical society of America* **51**, 1300 (1961).
- [166] M. CAVALLINI, G. GALLINARO, and G. SCOLES, *Zeitschrift Naturforschung Teil A* **22**, 413 (1967).
- [167] M. CAVALLINI, L. MENEGHETTI, G. SCOLES, and M. YEALLAND, *Rev. Sci. Instrum.* **42**, 1759 (1971).
- [168] M. FRANK, S. E. LABOV, G. WESTMACOTT, and W. H. BENNER, *Mass Spectrometry Reviews* **18**, 155 (1999).
- [169] D. H. ANDREWS, R. M. MILTON, and W. DESORBO, *Journal of the optical society America* **36**, 518 (1946).
- [170] D. H. ANDREWS, W. F. BRUCKSCH, W. T. ZIEGLER, and E. R. BLANCHARD, *Rev. Sci. Instrum.* **13**, 281 (1942).
- [171] A. GOETZ, *Phys. Rev.* **55**, 1270 (1939).
- [172] N. E. BOOTH and D. J. GOLDIE, *Supercond. Sci. Technol.* **9**, 493 (1996).

- [173] H. KRAUS, *Supercond. Sci. Technol.* **9**, 827 (1996).
- [174] D. TWERENBOLD, *Rep. Prog. Phys.* **59**, 349 (1996).
- [175] D. TWERENBOLD, J.-L. VUILLEUMIER, D. GERBER, A. TADSEN, B. VAN DEN BRANDT, and P. M. GILLEVET, *Appl. Phys. Lett.* **68**, 3503 (1996).
- [176] D. TWERENBOLD, D. GERBER, D. GRITTI, Y. GONIN, A. NETUSCHILL, F. ROSSEL, D. SCHENKER, and J.-L. VUILLEUMIER, *Proteomics* **1**, 66 (2001).
- [177] W. ENS, G. WESTMACOTT, and K. G. STANDING, *Nuclear Instruments and Methods in Physics Research Section B* **108**, 282 (1996).
- [178] G. FRASER, *International Journal of Mass Spectrometry* **215**, 13 (2001).
- [179] G. C. HILTON, J. M. M. AND D. A. WOLLMAN, K. IRWIN, L. L. DULCIE, D. GERBER, P. M. GILLEVET, and D. TWERENBOLD, *Nature* **391**, 672 (1998).
- [180] G. GOL'TSMAN, K. SMIRNOV, P. KOUMINOV, B. VORONOV, N. KAUROVA, V. DRAKINSKY, J. ZHANG, A. VEREVKIN, and R. SOBOLEWSKI, *IEEE Transactions On Applied Superconductivity* **13**, 192 (2003).
- [181] G. N. GOLTSMAN, O. OKUNEV, G. CHULKOVA, A. LIPATOV, A. SEMENOV, K. SMIRNOV, B. VORONOV, A. DZARDANOV, C. WILLIAMS, and R. SOBOLEWSKI, *Applied Physics Letters* **79**, 705 (2001).
- [182] A. D. SEMENOV, G. N. GOLTSMAN, and A. A. KORNEEV, *Physica C* **351**, 349 (2001).
- [183] A. VEREVKIN, J. ZHANG, R. SOBOLEWSKI, A. LIPATOV, O. OKUNEV, G. CHULKOVA, A. KORNEEV, K. SMIRNOV, , G. N. GOLTSMAN, and A. SEMENOV, *Applied Physics Letters* **80**, 4687 (2002).
- [184] A. KORNEEV, V. MATVIENKO, O. MINAEVA, I. MILOSTNAYA, I. RUBTSOVA, G. CHULKOVA, K. SMIRNOV, V. VORONOV,

- G. GOLTSMAN, W. SLYSZ, A. PEARLMAN, A. VEREVKIN, and R. SOBOLEWSKI, *IEEE Transactions on Applied Superconductivity* **15**, 571 (2005).
- [185] A. M. KADIN and M. W. JOHNSON, *Appl. Phys. Lett.* **69**, 3938 (1996).
- [186] A. BUDREVICH, B. TSIPINYUK, and E. KOLODNEY, *J. Phys. B* **29**, 4965 (1996).
- [187] A. DIVOCHIY, F. MARSILI, D. BITAULD, A. GAGGERO, R. LONI, F. MATTIOLI, A. KORNEEV, V. SLZNEV, N. KAUROVA, O. MINAEVA, G. GOL'TSMAN, K. G. LAGOUDAKIS, M. BENKHAOUL, F. LEVY, and A. FIORE, *Nature Photonics* **2**, 302 (2008).
- [188] G. GOLTSMAN, A. KORNEEV, A. DIVOCHIY, O. MINAEVA, M. TARKHOV, N. KAUROVA, V. SELEZNEV, B. VORONOV, O. OKUNEV, A. ANTIPOV, K. SMIRNOV, Y. VACHTOMIN, I. MILOSTNAYA, and G. CHULKOVA, *Journal of modern optics* **56**, 1670 (2009).

Acknowledgments

The presented work could not have been done without the help and support of other persons, whom shall be thanked at this place:

First of all I would like to thank Markus Arndt, who gave me the opportunity to write this PhD thesis in his group. But beside his supervision, moreover I would like to thank him for his constant motivation and support, which both were very important in some stages of the experiments. And I would like to thank him for everything he taught me, which is much more than pure physics, but also a variety of important soft skills needed for working as a scientist.

Since experimental physics is teamwork I would like to thank those persons, who spend a lot of time working with me in the lab (in chronological order): Hendrik Ulbricht, Philipp Haslinger, Michele Sclafani and Philipp Schmid. Special thanks also go to the rest of the Quantum group in Vienna for the nice atmosphere during the whole time.

I would also like to thank the group of Gregory Golt'sman for the collaboration on the SSPD project, which is continued also in the future. Special thanks go to Alexander Divochiy and Alexander Korneev, who visited us in Vienna to work together on the experiments.

Christoph Dellago and Harald Oberhofer shall be thanked for performing computational simulations and for interesting discussions.

For proof-reading the manuscript my special thanks go to Bill Case, Peter Lötscher, Philipp Schmid and Fraser McLennan Keir.

Finally I thank Philipp Haslinger and Michele Sclafani again, not only as a colleague, but also for their friendship and spending some great time during the one or other vacation.

Fundings were received from the Austrian Science Fund (FWF) within the projects START Y177 and Wittgenstein Z149-N16.

Curriculum vitae

Personal Information

- Name: Markus Marksteiner
- Date and place of birth: January 7, 1981, Linz, Austria
- Citizenship: Austria

Professional History

- Since 03/2006: Employment as Assistant in the group of Prof. Dr. Markus Arndt at the Faculty of Physics, University of Vienna

Education

- since 03/2006 Doctoral studies of Physics at the University of Vienna
- 10/2000-02/2006 Study of physics at the University of Vienna
- 10/1999-09/2000 Civilian service at the Lebenshilfe OÖ
- 09/1991-06/1999: Grammar school (Gymnasium Aloisianum in Linz)